

**Universidad Autónoma de Madrid  
Facultad de Ciencias  
Departamento de Química Orgánica**

**Technische Universität Berlin  
Faculty III Process Sciences  
Department of Applied Biochemistry**

**PHTHALOCYANINE-FULLERENE DYADS AND  
DNA INTERSTRAND CROSS-LINKING  
ON SURFACE**

**CINTHYA YAMILA VÉLIZ MONTES  
Doctoral Thesis**

Madrid 2017



“You never fail until you stop trying.”

Albert Einstein



This work was developed in the Department of Organic Chemistry of The Autonomia University of Madrid, under the supervision of Prof. Dr. Tomás Torres Cebada, Dr. Olga Trukhina and in the Fachbereich 1.8 of Bundesanstalt für Materialforschung und -prüfung (BAM) tutored by Dr. habil. Rudolf J. Schneider under the supervision of Prof. Dr. Jens Kurreck whom I express all my thankfulness.



Parts of this work was presented in the following articles:

- “Photo-induced cross-linking of short furan-modified DNA on surfaces”. C. Véliz Montes, H. Memczak, E. Gysels, T. Torres, A. Madder and R. J. Schneider. *Langmuir*, **2017**, *in press*; DOI: 10.1021/acs.langmuir.6b03855.
- “Unsubstituted, Covalently-linked Phthalocyanine-C60 Fullerene Dyads”. C. Véliz Montes, O. Trukhina, G. Bottari and T. Torres, **2017**. *Manuscript in preparation*.

This work has been developed in large parts within the EU Marie Curie Initial Training Network FP7-PEOPLE-2012-ITN “SO2S”, grant no. 316975.

- The first part of my doctoral research was performed in the group directed by Dr. Rudolf J. Schneider at Bundesanstalt für Materialforschung und -prüfung (BAM), Berlin, Germany, from June 2013 until August 2015, in close collaboration with Fraunhofer Institute for Cell Therapy and Immunology (IZI-BB), Branch Bioanalytics and Bioprocesses, Potsdam, Germany.
  - Experience in the chemistry of nucleic acids and DNA interstrand cross-linking methodologies was gained during a research stay in the group of Prof. Annemieke Madder, Organic and Biomimetic Chemistry Research Group, Ghent University, Belgium, from August to September 2013, with the help of her experienced PhD students Ellen Gysels and Nathalie De Laet.
  - The last step was done at Universidad Autónoma de Madrid in the group of Prof. Tomás Torres in the Department of Organic Chemistry from August 2015 to August 2016, under the kind guidance of Dr. Olga Trukhina and Dr. Giovanni Bottari.
- I would like to thank all of them warmly.





## Acknowledgements

First of all, I would like to express my gratitude to “The Singlet Oxygen Strategy” Marie Curie Initial Training Network (ITN) under the European Union Seventh Framework programme FP7-PEOPLE-2012-ITN for the financial support.

I would also like to express my most sincere gratitude to my supervisors Prof. Tomás Torres and Prof. Jens Kurreck for their time and guidance. I am very grateful and indebted to my research tutor Dr. habil. Rudolf Schneider for his continuous encouragement, support, and freedom for developing my work.

I express my profound gratitude to the whole Fachbereich 1.8 of Bundesanstalt für Materialforschung und -prüfung (BAM) for scientific discussion, advice and direct assistance in the lab and help with the German language. I'd like to extend my thanks for scientific discussions and ideas to my friends and PhD colleagues: Holger, Peter, Stephan, Martin, Mafalda, Lucía, Ana, Lidia and Robert. Special thanks to Kristin Hoffman and Sabine Flemig for their honest friendship and assistance. Thanks to Christin Heinrich for the big help with the management.

I would also like to thank Prof. Dr. Dirk M. Guldi and staff of the Department of Chemistry and Pharmacy at Friedrich-Alexander-Universität Erlangen/Nürnberg for the spectral characterization of my compounds, as well as the Surface Science Laboratory of Madrid Autonoma University, in particular PhD student Luigi Terracciano for his attempts of UHV STM deposition of prepared dyads onto surfaces.

Thanks to Dr. Olga Trukhina for her friendship, patience and excellent guidance in teaching me organic chemistry. I extend my sincere thanks to all the other members at the Nanoscience and Molecular Materials Research Group of the Department of Organic Chemistry of Madrid Autonoma University, for their help and suggestions. I dedicate a special acknowledgement to the senior scientists: Gianni, Andres, Salome, Gema, David and Marivi for being good examples of expertise and commitment to science. Special thanks to Giovanni Bottari for his scientific contributions and guidance. Thanks Irene for becoming a good friend, keeping the contact.

My sincere thanks to Henry Memczak and Walter Stöcklein from Fraunhofer Institute for Cell Therapy and Immunology, Branch Bioanalytics and Bioprocesses (IZI-BB) for collaboration on the SPR measurements. Thanks also to the members of the group of Biomarker Validation and Assay Development, without their assistance I could not have managed the experimental work.

I also want to thank for the opportunity that Prof. Annemieke Madder gave me to experience the chemistry of nucleic acids during my research stay as well to her group of Organic and Biomimetic Chemistry. Special thanks to Ellen Gyssels and Nathalie De Laet.

I'm very thankful to all my friends that during this period making me laugh and for their constant encouragement. My sincere thanks to my Rock Berliner's friends who directly supported me along this journey. I am deeply grateful to Nahla, Benita, Rafael, Margarida and Ana for hearing me, and sharing my daily frustrations and successes.

Thanks to my parents, who taught me from an early age to always see light on the difficulties and to help without expecting anything back, and to my dear littles Michelle and Kristel, for motivating me being better. I thank my whole family for their support and being by my side. My aunts Nubia and Tanya are specially acknowledged for their love and motivating words.

I cannot express all my respect and gratitude I feel for all of you. Once again, I thank you.

“There is no other God who can rescue like this.”

Daniel 3:29

## Abbreviations

AFM	Atomic force microscope
CHCA	$\alpha$ -cyano-4-hydroxycinnamic acid
CR	Charge recombination time
CRP	C-reactive protein
CS	Charge separation time
cTnI	Cardiac troponin I
CVD	Cardiovascular Disease
D-A	donor-acceptor
DDI	DNA-directed immobilization
EADS	Evolution-associated differential spectra
ELISA	Enzyme-linked immunosorbent assay
hFABP	Heart-type fatty acid binding protein
HRP	Horseradish peroxidase
ICL	Chemical interstrand crosslinking
MALDI-TOF	matrix-assisted laser desorption/ionization time-of-flight
MB	Methylene blue
MS	mass spectroscopy
NA	Neutravidin
OD	Optical density
ODN	DNA oligonucleotide
OPV	Organic Photovoltaics
OSCs	Organic Solar Cells
PA	Photoinduced absorption
Pc	Phthalocyanine
PCE	Power Conversion Efficiencies
Pc-C <sub>60</sub>	Phthalocyanine-C <sub>60</sub> fullerene
PET	photoinduced electron transfer
PMMA	Polymethyl-methacrylate
Por	Porphyrin
PPV	poly(p-phenylenevinylene)
PSI	Photosensitizer
ROS	Reactive oxygen species
RU	Resonance Units
SA	Sinapinic Acid
SAM	Self-assembled monolayer
SE	Stimulated emission
SPR	Surface Plasmon Resonance
STM	Scanning Tunnelling Microscope
TA	Transient absorption spectra
THF	Tetrahydrofuran
TLC	thin-layer chromatography
TMB	3,3',5,5'-tetramethylbenzidine
TPB	1,1,4,4-tetraphenyl-1,3-butadiene
ZnPc	Zinc Phthalocyanine



# Contents

---

Abstract .....	1
Resumen .....	5
Zusammenfassung .....	9
Thesis Outline .....	13
1. Introduction .....	17
1.1 Phthalocyanines .....	19
1.2 Phthalocyanines-fullerene dyads .....	21
1.2.1 Nanotechnology and self-assembly .....	21
1.2.2 Donor-acceptor ensembles .....	23
1.2.3 Covalently-linked Pc-C <sub>60</sub> systems .....	26
1.3 DNA interstrand cross-linking on surface .....	35
1.3.1 Biosensors in cardiovascular diseases detection .....	35
1.3.2 Biosensors and DNA in nanotechnology .....	43
1.3.3 Furan mediated DNA-ICL cross-linking .....	54
2. Objectives .....	59
2.1 Phthalocyanine-fullerene dyads .....	61
2.2 DNA interstrand cross-linking on surface .....	63
3. Materials and Methods .....	65
3.1 Phthalocyanine-fullerene dyads .....	67
3.1.1 Chemicals and instrumentation .....	67
3.1.2 Synthesis of dyad precursors .....	68
3.1.3 Synthesis of Zn(II)Pc-C <sub>60</sub> fullerene dyads .....	75
3.1.4 Experimental techniques .....	79
3.2 DNA interstrand cross-linking on surface .....	85
3.2.1 Chemicals and instrumentation .....	85
3.2.2 Experimental procedures .....	87
3.2.2.1 Surface Plasmon Resonance .....	87

3.2.2.2 ELISA.....	90
3.2.2.3 MALDI-TOF sample preparation procedures .....	90
3.2.2.4 Cross-linking in solution .....	91
3.2.3 Antibody-oligonucleotide conjugation .....	93
3.2.4 Cross-reactivity experiments of the multiplex immunoassay .....	94
3.2.5 Experimental techniques .....	95
4. Results and Discussion .....	101
4.1 Phthalocyanines-fullerene dyads.....	103
4.1.1 Synthesis and characterization.....	103
4.1.2 Photophysical studies of the dyads .....	113
4.1.2.1 Photophysics in THF solution.....	119
4.1.2.2 Photophysics in PMMA films on glass.....	121
4.1.2.3 Photophysics in drop casted films on glass.....	124
4.1.3 Microscopic characterization .....	126
4.2 DNA interstrand cross-linking on surface.....	129
4.2.1 DNA-directed immobilization on SPR biosensor chips .....	130
4.2.2 Light-induced immobilization on microplate surfaces .....	136
4.2.3 Multiplex immunoassay cross-reactivity .....	137
4.2.4 Implementation of ICL in immunoassays.....	138
5. Conclusions.....	139
5.1 Phthalocyanine-C <sub>60</sub> fullerene dyads .....	141
5.2 DNA Interstrand cross-link on surface .....	142

## **Abstract**

---





Nanotechnology deals with structures and components of nanoscale size in order to create new properties or to improve significantly their physical, chemical and biological properties, processes and phenomena. Many efforts of molecular nanotechnology are directed to design artificial nanostructures on surfaces due to their potential applications in nanodevices and biosensors. This thesis includes two areas of application, phthalocyanine-based photovoltaic dyads and using phthalocyanine-based photosensitisation in creating a stable biosensor chip surface.

To date, phthalocyanine (Pc)-C<sub>60</sub> fullerene arrays have shown interesting electrochemical, photophysical and photovoltaic properties. In this case the systems are constituted by an unsubstituted phthalocyanine (donor) and a fullerene (acceptor) unit. As a result of the absence of any substituent at the Pc peripheral positions, these building blocks show a better organization at supramolecular level. This results in important changes in some physical properties of these systems with respect to their individual counterparts. Assembling of Pc-C<sub>60</sub> nanostructures on substrate surfaces and their photo-induced energy/electron transfer properties were also studied.

The fabrication of biosensor chips for clinical diagnosis is becoming an increasingly important topic. A large number of biosensors are aimed to the diagnosis of cardiovascular diseases, which represent 45% of all deaths in Europe. DNA-directed immobilization (DDI) is a technique that allows the preparation of protein immunoarrays by forming a self-assembled monolayer (SAM) of DNA target molecules with DNA probes previously immobilized on a surface. One of the drawbacks of DDI is that it requires long oligonucleotides (ODNs) for recognition and stable duplex formation. Shorter ODNs would be sufficient for antibody addressing but they are not stable enough during storage and handling (e.g. rinsing) steps.

Chemical interstrand crosslinking (ICL) of short ODNs in solution has been studied before by several groups due to its important clinical applications. The furan-based ICL strategy has been widely studied in solution and presents the advantage of selective oxidation of the furan-modified ODN which leads to the fast formation of a covalent bond with the complementary ODN sequence. This very stable DNA duplex showed extraordinary resistance towards enzymatic digestion and higher melting temperatures in comparison with the non-cross-linked DNA duplex. One studied oxidant is singlet oxygen, produced in a photosensitised reaction involving a phthalocyanine.

## Abstract

On this basis this thesis also describes as an application the development of a novel platform based on DDI to detect three cardiac biomarkers in a multiplex immunoarray, requiring only short dodecamer (12mer) ODNs for addressing the antibody, as a consequence of the increased DNA duplex stability after cross-linking. Methylene blue and a phthalocyanine were used as photosensitisers for the ICL formation.

This thesis reports on recent experiments on both Pc-C<sub>60</sub> and immobilized DNA ICL. Open problems and future applications are also discussed.

Key words: Nanotechnology, biosensor, phthalocyanine, fullerene, nanostructures, cardiac biomarker, DNA, DNA-directed immobilization, interstrand cross-linking, furan, singlet oxygen.

## **Resumen**

---



La nanotecnología trata con estructuras y componentes de tamaño nanométrico para crear o mejorar sus propiedades, procesos y fenómenos físicos, químicos o biológicos. En este campo, una gran parte de la investigación está dirigida a diseñar nanoestructuras artificiales en superficies, debido a su potencial aplicación en nanodispositivos y biosensores. Esta tesis abarca dos áreas de aplicación, diadas fotovoltaicas basadas en ftalocianinas y fotosensibilización basada en ftalocianinas para crear un chip con una superficie estable para un biosensor. A lo largo de la misma se describen los resultados obtenidos en ambos temas, diadas Pc-C<sub>60</sub> y ADN inmovilizado, además de discutir los problemas observados y las futuras aplicaciones.

En las últimas décadas, el estudio de diadas ftalocianina (Pc)-fulereno C<sub>60</sub> ha resultado en la demostración de interesantes propiedades electroquímicas, fotofísicas y fotovoltaicas. En esta tesis, se presenta diadas formadas por una ftalocianina sin sustituyentes periféricos (dador) y un fullereno (aceptor). Como resultado de la ausencia de sustituyentes en las posiciones periféricas, nuestras diadas mostraron una mayor capacidad de organización a nivel supramolecular. Esto repercute en algunas de sus propiedades físicas de estos sistemas con respecto a sus homólogos individuales. En este trabajo se presenta un estudio del ordenamiento de las nanoestructuras Pc-C<sub>60</sub> en superficies, y sus propiedades de transferencia de energía o electrones fotoinducidas.

Por otro lado, la fabricación de chips biosensores para aplicaciones diagnósticas se está convirtiendo en un tema de creciente importancia y atractivo científico. El principal objetivo de estos biosensores es el diagnóstico de enfermedades cardiovasculares, las cuales representan el 45% de todas las muertes en Europa. La inmovilización dirigida por ADN (DDI) es una técnica que permite la preparación de matrices mediante la formación una monocapa auto-ensamblada (SAM) de moléculas diana de ADN. Una de las desventajas del DDI es la necesidad de emplear oligonucleótidos de alto peso molecular (ODNs) para el reconocimiento y la formación estable de la doble hélice. ODNs más cortos podrían ser suficientes para interactuar con el anticuerpo pero no son lo suficientemente estables para su conservación y pasos de manipulación (ej. lavado).

La formación de enlaces químicos intercatenarios (ICL) de oligonucleótidos cortos han sido estudiados en disolución por varios grupos debido a sus importantes aplicaciones clínicas. La estrategia de ICL basada en el furano ha sido utilizada ampliamente en disolución y presenta como principal ventaja la oxidación selectiva del ODN modificado

## Resumen

con el furano, la cual produce la formación de un enlace covalente con el ODN de la secuencia complementaria. Esta doble hélice resultó ser extraordinariamente resistente a la digestión enzimática, además de presentar un punto de fusión bastante elevado en comparación con la doble hélice de ADN no enlazada. Para la oxidación de los oligonucleótidos preparados en esta tesis se utilizó el oxígeno singlete, producido en una reacción fotosensible implicando una ftalocianina.

A partir de los resultados obtenidos, esta tesis también describe como una aplicación el desarrollo de una nueva plataforma basada en DDI para detectar tres biomarcadores cardíacos en un dispositivo que incluye sólo ODNs cortos dodecámeros, 12 mer) para direccionar el anticuerpo. Esto ha sido posible gracias al incremento de la estabilidad de la doble hélice de ADN después de enlace intercatenario. Para la formación de dicho enlace, se han utilizado azul de metileno y ftalocianina como fotosensibilizadores.

Esta tesis reporta ambos experimentos, Pc-C<sub>60</sub> e inmovilizado ADN ICL. Problemas observados y futuras aplicaciones también se comentan.

Palabras clave: Nanotecnología, biosensor, ftalocianina, fullereno, nanoestructuras, biomarcadores cardíacos, ADN, inmovilización dirigida por ADN, enlace intercatenario, furano, oxígeno singlete.

## **Zusammenfassung**

---





Nanotechnologie untersucht Bestandteile und Strukturen von Materialien im Nanobereich, um Prozesse und Phänomene besser zu verstehen beziehungsweise neue oder verbesserte physikalische, chemische sowie biologische Eigenschaften zu erzeugen. Viel Forschungsarbeit im Bereich der molekularen Nanotechnologie wurde geleistet, um künstliche Oberflächennanostrukturen zu erzeugen um diese als Biosensoren oder Nanoröhren zu verwenden. Diese Arbeit beinhaltet zwei Anwendungsbereiche, Phthalocyanin-basierte Photovoltaik-Dyaden und Phthalocyanin-basierte Photosensibilisatoren, um eine stabile Chipoberfläche zu generieren und diese als Biosensor zu verwenden.

Phthalocyanin-Fullerene (Pc)-C<sub>60</sub> haben interessante elektrochemische, photophysikalische und photovoltaische Eigenschaften. In diesem Fall besteht das System aus einer unsubstituierten Phthalocyanin- (Donor) und einer Fulleren-Einheit (Akzeptor). Durch Abwesenheit einer peripheren Substitution am Pc, zeigen diese Gebilde eine höhere Ordnung auf supramolekularer Ebene. Daraus resultiert ein entscheidender Wechsel einiger physikalischer Eigenschaften. Der Aufbau der Pc-C<sub>60</sub> Nanostrukturen und ihre photoinduzierten Energie- beziehungsweise Elektronentransfereigenschaften wurden ebenfalls untersucht.

Die Herstellung von Biosensorchips zur Anwendung in der klinischen Diagnostik wird ein immer wichtigeres Thema. Eine Großzahl von Biosensoren werden angewendet zur Diagnostizierung von Herz-Kreislauf-Erkrankungen, welche verantwortlich für 45 % aller Todesfälle in Europa sind. Die DNA-vermittelte Immobilisierung (DDI) ist eine Technik, welche die Herstellung von Protein-Immunoassays durch Bildung einer selbstorganisierten Monoschicht von spezifischer DNA mit zuvor auf einer Oberfläche immobilisierten, komplementären DNA, ermöglicht. Ein Nachteil von DDI ist, dass lange Oligonukleotide (ODNs) für die Bildung von stabilen Duplexformen notwendig sind. Kurze ODNs wären ausreichend stabil zur Immobilisierung der Antikörper, jedoch nicht für die Lagerung und Waschschriffe.

Chemische intra-Strang Kreuzvernetzungen (ICL) von kurzen ODNs in Lösung wurden aufgrund ihrer Wichtigkeit für die klinische Diagnostik bereits häufiger untersucht. Die Furan-basierte ICL-Strategie stellt den Vorteil der selektiven Oxidation von Furan-modifizierten ODNs dar, welche eine schnelle kovalente Verknüpfung mit dem komplementären ODN-Strang ermöglicht. Dieser sehr stabile DNA-Duplex weist außergewöhnliche Robustheit gegenüber enzymatischem Verdau und eine höhere Schmelztemperatur im Vergleich zum nicht verknüpften DNA-Komplex auf. Ein untersuchtes Oxidationsmittel ist Singulett-Sauerstoff, welcher durch eine Photoreaktion vom Phthalocyanin produziert wird.

## Zusammenfassung

Auf dieser Grundlage beschreibt diese Arbeit auch die Anwendung einer neuartigen Plattform, basierend auf DDI, um drei Herzinfarkt-Biomarker in einem Multiplex-Immunoarray zu messen. Dabei sind, aufgrund der hohen Stabilität des DNA-Duplex nach Verknüpfung, nur Dodecamere (12mere) von ODNs zur Immobilisierung der Antikörper notwendig. Methylenblau und ein Phthalocyanin wurden als Photosensibilisatoren für die ICL benutzt.

Diese Arbeit berichtet über neue Experimente sowohl an Pc-C<sub>60</sub> als auch an Oberflächen-DNA-ICL. Offene Fragen und zukünftige Anwendungen werden ebenfalls diskutiert.

Schlüsselbegriffe: Nanotechnologie, Biosensor, Phthalocyanin, Fullerene, Nanostrukturen, Herzinfarkt-Biomarker, DNA-vermittelte Immobilisierung, intra-Strang Kreuzvernetzung, Furan, Singulett-Sauerstoff.

## **Thesis Outline**

---



Each chapter of this thesis has been divided into two sections. The first part is centered around the donor-acceptor Pc-C<sub>60</sub> dyads and the second part discusses the DNA interstrand cross-linking (ICL) on surface. This dissertation is arranged as follows:

## 1. Introduction

This section provides the motivation of the work, background information, and a literature review. The first part introduces the self-assembly systems in nanoscience and molecular nanotechnology, also some basic concepts about phthalocyanines (Pc) and Pc-C<sub>60</sub> based conjugates.

In the second part the role of biosensors in cardiovascular diseases detection, DNA in nanotechnology and biosensors are introduced, as well as basic concepts about DNA and ICL formation in solution.

## 2. Objectives

States the major questions that the research intends to answer. In summary, the aim of the first section is the synthesis of four novel covalently-linked ZnPc-C<sub>60</sub> conjugates and to deposit them on surfaces to study their organization by TEM, STM, AFM, and to study the potential applicability of the novel dyads for energy conversion.

The main aim of the second section is the establishment of a new method for DNA-ICL on the surface via singlet oxygen, using methylene blue or a ZnPc derivative ("TT1") as photosensitizers, and to study the possible applications in a multiplex addressable immunoassay for the detection of three cardiac biomarkers using short ODN for addressing the antibody (C-reactive protein, heart-type fatty acid binding protein and Troponin I).

### **3. Materials and Methods**

The first part of this section gives experimental details about the synthesis of unsubstituted Pc-C<sub>60</sub> dyads and their precursors as the experimental techniques used to perform the surface and photoexcitation dynamics studies.

The second section is about the steps followed during the development of the methodology for ICL of immobilized oligonucleotide. SPR, ELISA and microarray experiments are described.

### **4. Results and Discussion**

The results are presented, analysed and discussed. Synthesis of the dyads' precursors and the Pc-C<sub>60</sub> dyads' conjugates with its photophysical study in solution as well as on the surface and the different microscopic characterizations are provided.

Within the second section, a novel ICL methodology on surface-immobilized short DNA oligonucleotides is detailed and the problems found for the implementation of the new DNA platform in a multiplex addressable immunoassay are also described.

### **5. Conclusion**

Provides a summary of key findings on both topics. Briefly, the results of the first section suggest the necessary use of nanocomposite polymers as a possible template for enhancing the supramolecular ordering and consequent organic photovoltaics performance of the ZnPc-C<sub>60</sub> dyads.

The main conclusion of this section is that ICL formation of immobilized DNA is a very useful method for increasing the stability of short DNA oligonucleotide on a surface. Comparing both photosensitizers, methylene blue was more efficient than the ZnPc. The developed methodology has the drawback that it cannot be implemented in an addressable immunoassay due to the loss of the recognition activity of the capture antibody for the protein of analysis.

Summarizing it can be said that for phthalocyanines another two applications could be developed which show the high versatility of this diverse group of compounds.

## **1. Introduction**

---





## 1.1 Phthalocyanines

Phthalocyanines (PCs) enjoy a privileged position within the large family of porphyrinoid systems. These chromophores, which have a two-dimensional (2-D) and 18- $\pi$ -electron aromatic system, have been commended as thermally stable excellent light-harvesters with major absorption at the maximum of the solar photon flux – at around 700 nm. More importantly, the optical and electronic properties as well as the redox character of these macrocycles can be easily modulated by the careful choice of the metal center and/or the peripheral substituents, making them perfect building blocks for light harvesting, photovoltaic, and molecular photonic applications.<sup>1</sup>

Their 18  $\pi$ -electron system generates absorption spectra with two major intense bands: The Q and the Soret band. The Soret band is centered in the range of 350 nm and, and is usually a broad and has low intensity. The Q band lies in the visible region around 620-720nm. The position and the shape of the Q band determines the color of the Pc, and depends on several factors such the central metal, type of substitution (peripheral, non-peripheral and axial substitution, Figure 1)<sup>2</sup>, the solvent in which the compound is dissolved, its aggregation behavior, and the extent of  $\pi$ -conjugation.

The nature of the central atom of the Pcs has a strong impact in their photophysical properties, influencing their fluorescence electronic absorption, fluorescence and phosphorescence spectra, and the triplet excited state generation.<sup>3</sup> Transition metal ions produce short triplet lifetimes, in the nanosecond range, while closed-shell and diamagnetic metals,

---

<sup>1</sup> a) G. Bottari; G. de la Torre; T. Torres, *Acc. Chem. Res.*, **2015**, *48*, 900–910; b) N. L. Bill., O.Trukhina, J. L. Sessler, T. Torres, *Chem. Commun.*, **2015**, *51*, 7781–7794; c) G. Bottari.; O.Trukhina, M. Ince; T. Torres, *Coord. Chem. Rev.*, **2012**, *256*, 2453–2477; d) F. D'Souza; O. Ito, *Coord. Chem. Rev.*, **2005**, *249*, 1410–1422.e) G. de la Torre, G. Bottari, M. Sekita, A. Hausmann, D.M. Guldi, T. Torres, *Chem. Soc. Rev.*, **2013**, *42*, 8049-8105; f) H. Imahori, T. Umeyama, K. Kurotobi, Y. Takano, *Chem. Commun.*, **2012**, *48*, 4032-4045; g) *Handbook of Porphyrin Science*, Academic Press, San Diego, **2010**, Vols. 1–15.

<sup>2</sup> L. Martin-Gomis, F. Fernandez-Lazaro and A. Sastre-Santos, *J. Mater. Chem. A.*, **2014**, *2*, 15672.

<sup>3</sup> a) A. Morandeira, I. López-Duarte, M. V. Martínez-Díaz, B. O'Regan, C. Shuttle, N. A. Haji-Zainulabidin, T. Torres, E. Palomares, J. R. Durrant, *J. Am. Chem. Soc.*, **2007**, *129*, 9250-9251; b) Y. Rio, M. S. Rodríguez Morgade, T. Torres, *Org. Biomol. Chem.*, **2008**, *6*, 1877-1894; c) A. Listorti, I. López-Duarte, M. V. Martínez-Díaz, T. Torres, T. Dos Santos, P. R. F. Barnes, J. R. Durrant, *Energ. Environ. Sci.*, **2010**, *3*, 1573-1579; d) X. F. Zhang, X. Shao, H. Tian, X. Sun, K. Han, *Dyes Pigm.*, **2013**, *99*, 480-488.

## Introduction

such as zinc, aluminum and gallium, leads to high triplet state quantum yields, short lifetimes and high singlet oxygen quantum yields,  $\Phi_{\Delta} \geq 0.7$ .<sup>4</sup>

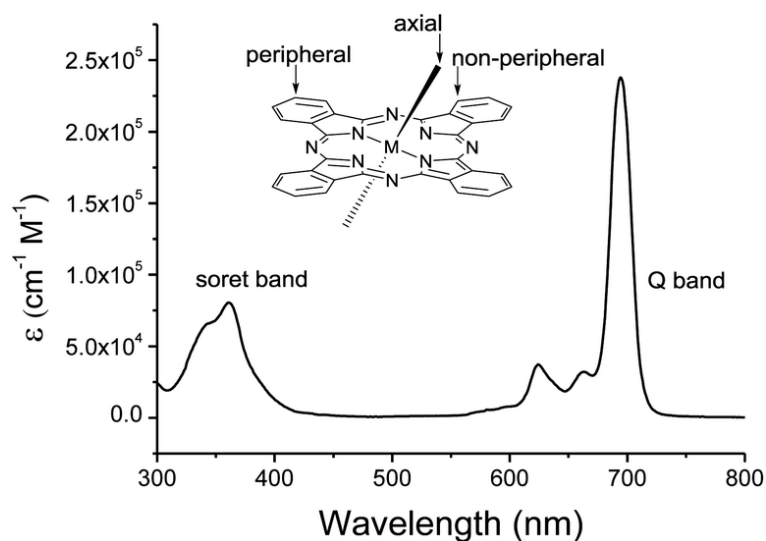


**Figure 1.** Typical structure of a Pc showing the non-peripheral, peripheral and axial positions which can be functionalized, together with a typical UV-vis spectrum of a metallophthalocyanine. Adopted from ref 16 with permission from The Royal Society of Chemistry (RSC).

Zinc phthalocyanines (ZnPc) show high absorption in the red region of solar spectrum (Q-band) and good singlet oxygen generation yield,<sup>5</sup> rendering them promising candidates as photosensitizers for DNA cross-linking. However, the formation of dimeric aggregates, which is promoted in aqueous solutions, reduces its photoactivity<sup>6</sup> and singlet oxygen quantum yields compared to the corresponding monomer.<sup>7</sup> TT1 (Scheme 1) is a well-known ZnPc photosensitizer bearing a carboxylic moiety and three bulky *tert*-butyl groups that help to minimize the formation of molecular aggregates.<sup>8</sup> The photophysical properties in aqueous media of TT1 functionalized with cholesteryl oleate have been studied before, pointing out that this functionalized TT1 derivative can still effectively photosensitize <sup>1</sup>O<sub>2</sub> formation.<sup>9</sup>

<sup>4</sup> G. Jori. In *CRC Handbook of Organic Photochemistry and Photobiology*, F. Lenci, W. Horspool, (Eds.), CRC Press, **2004**. 146–141.

<sup>5</sup> C. M. Allen, W. M. Sharman and J. E. Van Lier, *J. Porphyr. Phthalocya.*, **2001**, 5, 161-169.

<sup>6</sup> J. R. Darwent, P. Douglas, A. Harriman, G. Porter and M. C. Richoux, *Coord. Chem. Rev.*, **1982**, 44, 83-126.

<sup>7</sup> X. F. Zhang and H. J. Xu, *Faraday Trans.*, **1993**, 89, 3347-3351.

<sup>8</sup> J-J. Cid, J.-H. Yum, S.-R. Jang, M. K. Nazeeruddin, E. M. Ferrero, E. Palomares, J. Ko, M. Graetzel and T. Torres, *Angew. Chem. Int. Edit.*, **2007**, 46, 8358-8362.

<sup>9</sup> L. E. S. Contreras, J. Zirzmeier, S. V. Kirner, F. Setaro, F. Martinez, S. Lozada, P. Escobar, U. Hahn, D. M. Guldi and T. Torres, *J Porphyr. Phthalocya.*, **2015**, 19, 320-328.



**Scheme 1.** Synthesis of carboxyphthalocyanine TT1. Reproduced with copyrights permissions from John WILEY-VCH Verlag GmbH & Co.

## 1.2 Phthalocyanines-fullerene dyads

### 1.2.1 Nanotechnology and self-assembly

The first time that nanotechnology was formally recognized as a viable field of research was during the annual meeting of the American Physical Society on December 29<sup>th</sup> 1959. During the lecture delivered by the Nobel Prize Winner Richard P. Feynman entitled “There’s plenty of room at the bottom - an invitation to enter a new field of physics”<sup>10</sup> it was described how the natural laws should not limit the ability to work at the molecular level, atom by atom. He challenged the researchers to develop appropriate techniques and equipment for doing so. The age of nanotechnology started relatively recently, 30 years ago, once scientists had developed the scanning tunneling microscope<sup>11</sup> (STM) and the atomic force microscope<sup>12</sup> (AFM) which possess three-dimensional resolution down to the atomic scale.

The general and complete definition of nanotechnology is this statement: “The essence of nanotechnology is the ability to work at the molecular level, atom by atom, to create large structures with fundamentally new molecular organization. Nanotechnology is concerned with materials and systems whose structures and components exhibit novel and significantly improved physical, chemical, and biological properties, phenomena, and processes due to their nanoscale size. The aim is to exploit these properties by gaining control of structures and devices at atomic, molecular, and supramolecular levels and to learn to

<sup>10</sup> R. Feynman, “*There’s Plenty of Room at the Bottom*” at the American Physical Society meeting at Caltech, **1959**.

<sup>11</sup> G. Binning, H. Rohrer, Ch. Gerber and E. Weibel, *Phys. Rev. Lett.*, **1982**, 49, 57.

<sup>12</sup> G. Binning, C. F. Quate, Ch. Gerber, *Phys. Rev. Lett.*, **1986**, 56, 930.

## Introduction

efficiently manufacture and use these devices".<sup>13</sup> In order to produce nanoscale materials in reproducible and controllable manners, top-down and bottom-up approaches were developed.<sup>14</sup> The top-down approach is the assembly by manipulating components with larger devices to give smaller features, for example by lithographic techniques. However, this technique has limitations when the size of the desired feature is below 100 nm. Thus, the bottom-up approach is an alternative way for the creation of nanostructures because it can easily go far beyond the previous size limitation. The bottom-up approach consists in the self-assembly of machines from basic chemical building blocks, and this is considered to be an ideal through which nanotechnology is implementing itself. Nanoscience and nanotechnology have become promising approaches for many applications including medical, pharmaceutical, microbiology, energy conversion, etc.<sup>15</sup>

---

<sup>13</sup> Interagency Working Group on Nanoscience, Engineering and Technology "*National Nanotechnology Initiative: Leading to the Next Industrial Revolution*" US National Science and Technology Council, **2000**.

<sup>14</sup> G. A. Mansoori and T. A. Fauzi Soelaiman, "*Nanotechnology—An Introduction for the Standards Community*", J. ASTM Int., **2005**, 2, 6.

<sup>15</sup> a) G. A. Mansoori, "Principles of Nanotechnology: Molecular Based Study of Condensed Matter in Small Systems", WCPC, 2005; b) T. Rajagopalan, K. Venumadhav, G. Arkasubhra, C. Nripen, G. Keshab and G. Shubhra, *Rep. Prog. Phys.*, **2013**, 76, 066501; c) E. J. Chung and M. Tirrell, *Adv. Healthc. Mater.*, **2015**, 4, 2408-2422; d) K. Avijit, B. Kaustuv and L. Peter, *Nanotechnology*, **2017**.

## 1.2.2 Donor-acceptor ensembles

The rational design and successful fabrication of functional materials received much attention over the last decade, extensively employing the versatile tools of *supramolecular chemistry*.<sup>16</sup> Thus, with well-defined principles of molecular recognition<sup>17</sup> in hands, multiple supramolecular species have been generated by research society for sensing and catalytic applications, resulting from the intermolecular association of the corresponding molecular building blocks.<sup>18</sup> However, the fabrication of larger entities by spontaneous association of undefined number of species into a specific phase with well-defined macroscopic characteristics remains a challenge. Currently, many research groups keep exploring the basic principles and concepts to assemble building blocks into organized states exhibiting specific functions including optical, electrical, and magnetic properties.<sup>19</sup> Compounds with an extended  $\pi$ -conjugation are considered promising candidates in this respect, step-by-step finding their applications in organic thin-film electronics such as organic light-emitting diodes,<sup>20</sup> organic field-effect transistors,<sup>21</sup> and organic photovoltaics (OPV).<sup>22</sup>

OPV devices have been intensely investigated in the last decades owing to their potential to open up new markets where classical silicon technology cannot compete. Their exceptional properties such as transparency, light weight, flexibility and tunability of colors and others, remain very attractive for integration of OPV devices into consumer products and buildings, yielding environmentally friendly electricity generation at zero additional footprint. However, both power conversion efficiencies (PCE) and operational stability of OPV

<sup>16</sup> a) A. Harada, R. Kobayashi, Y. Takashima, A. Hashidzume, H. Yamaguchi, *Nat. Chem.*, **2011**, 3, 34-37; b) O. Ikkala, G. ten Brinke, *Science*, **2002**, 295, 5564, 2407-2409; c) Q. Zhang, J. He, H. Zhuang, H. Li, N. Li, Q. Xu, D. Chen and J. Lu, *Adv. Funct. Mater.*, **2016**, 26, 146-154.

<sup>17</sup> A. D. Buckingham, A. C. Legon, S. M. Roberts, *Principles of Molecular Recognition*, Springer Netherlands, 1993.

<sup>18</sup> a) D. Sun, et al., *J. Am. Chem. Soc.* **2002**, 124, 6604-6612 b) Y. Liu, T. Pauloehrl, S. Presolski, I. Albertazzi, L. Palmans, *J. Am. Chem. Soc.* **2015**, 137, 13096-105; b) Schreiner, P. R. *Chem. Soc. Rev.* **2003**, 32, 289-96; c) E. Morales-Narváez, L. Baptista-Pires, A. Zamora-Gálvez and A. Merkoçi, *Adv. Mater.*, **2016**, DOI: 10.1002/adma.201604905.

<sup>19</sup> a) Herr, D. J.C., *J. Mater. Res.*, **2011**, 122-139; b) *Bottom-up Nanofabrication*, ed. K. Ariga and H. S. Nalwa, American Scientific Publishers, CA, 2009.

<sup>20</sup> a) Hong, M.; Ravva, M. K.; Winget, P.; Bredas, J.-L. *Chem. Mater.*, **2016**, 28, 5791-5798; b) L.-S. Cui, et al., *Angew. Chem. Int. Ed.*, **2016**, 55, 6864-6868.

<sup>21</sup> a) Ford, M. J.; Wang, M.; Patel, Sh. N.; Phan, H.; Segalman, R. A.; Nguyen, T.-Q.; Bazan, G. C. *Chem. Mater.* **2016**, 28, 1256-1260; b) Jiang, H.; Ye, J.; Hu, P.; Wei, F.; Du, K.; Wang, N.; Ba, T.; Feng, Sh.; Kloc, Ch., *Sci. Rep.* **2014**, 4, 7573.

<sup>22</sup> a) S. Holliday, R. S. Ashraf, A. Wadsworth, D. Baran, S. A. Yousaf, C. B. Nielsen, C.-H. Tan, S. D. Dimitrov, Z. Shang, N. Gasparini, M. Alamoudi, F. Laquai, C. J. Brabec, A. Salleo, J. R. Durrant, I. McCulloch, *Nat. Commun.*, **2016**, 7, 11585; b) R. C. Masters, et al., *Nat. Commun.*, **2015**, 6, 6928; c) Y. Liu, et al., *Nat. Commun.*, **2014**, 5, 5293.

devices are still significantly lower than those of inorganic compounds.<sup>23</sup> In recent years, progress has been made by reducing typical loss processes for charge generation and extraction, by using lower bandgap polymers<sup>24</sup> and by controlling the nanomorphology of the photoactive layers using additives,<sup>25</sup> ternary blends,<sup>26</sup> and controlling the processing conditions. However, the fundamental primary process of OPV, namely *charge generation* and *separation* across the donor-acceptor interface, is still not fully understood.

The presence of ultrafast direct charge generation has been shown to depend on size of the donor and acceptor-rich phases and on the excitation wavelength, however ambiguities remained with respect to the extension of the primary charge transfer state, as well as to the influence of specific donor and acceptor conformations at the interface. For these reasons, donor-acceptor dyads have been introduced as synthetic model systems for the donor-acceptor interface. Owing to their biological relevance and useful properties, porphyrinoids has been extensively incorporated into light-to-energy conversion schemes as both, photosynthetic antenna and reaction center module.<sup>27</sup>

Up to date, phthalocyanines (Pcs) has been commended as thermally stable excellent light-harvesters with major absorption at the maximum of the solar photon flux – at around 700 nm, Pc also possess in fact unique physicochemical properties which render these macrocycles valuable building blocks in nanomaterials science. To this end, *fullerenes* represent another class of widely explored molecular materials that have generated an enormous interest in the field of nanoelectronics. On one hand, their rigid aromatic structure evokes low reorganization energies in electron transfer reactions. On the other hand, their extended  $\pi$ -conjugation affords efficient charge stabilization.<sup>28</sup> Unique architectural flexibility and chemical versatility of fullerenes allow the fine-tuning of their properties. Covalent

---

<sup>23</sup> S. Karuthedath, T. Sauermann, H.-J. Egelhaaf, R. Wannemacher, C. J. Brabe, L. L uer, *J. Mater. Chem. A.*, **2015**, 3, 3399-3408.

<sup>24</sup> C. Wang, et al, *Adv. Energy Mater.*, **2016**, doi: 10.1002/aenm.201600148.

<sup>25</sup> Y.-S. Jung, J.-S.k Yeo, N.-K. Kim, S. Lee, D.-Y. Kim, *ACS Appl. Mater. Interfaces.*, **2016**, 8, 30372-30378.

<sup>26</sup> M. Koppe, H.-J. Egelhaaf, E. Clodic, M. Morana, L. L uer, A. Troeger, V. Sgobba, D. M. Guldi, T. Ameri, C. J. Brabec, *Adv. Energy Mater.*, **2013**, 3, 949-958.

<sup>27</sup> a) A. Satake, Y. Kobuke, *Org. Biomol. Chem.*, **2007**, 5, 1679-1691; b) H. Imahori, *J. Phys. Chem.*, **2004**, 108, 6130-6143; c) D. M. Guldi, *Chem. Soc. Rev.*, **2002**, 31, 22-36.

<sup>28</sup> a) M. Lederer, U. Hahn, J.-M. Strub, S. Cianf erani, A. Van Dorsselaer, J.-F. Nierengarten, T. Torres, D. M. Guldi, *Chem. Eur. J.*, **2016**, 22, 2051-2059; b) S. Kirner, M. Sekita, D. M. Guldi, *Adv. Mat.*, **2014**, 26, 1482-1493; c) A. J. Ferguson, et al., *Mat. Letters* **2013**, 90, 115-125; d) Ch.-Z, et al., *J. Mat. Chem.* **2012**, 22, 4161-4177.

modification of their exterior<sup>29</sup> and incorporation of molecular guest into their interior<sup>30</sup> constitutes extremely efficient strategies in this connection. In light of the aforementioned, a myriad of electron donor-acceptor conjugates/hybrids have been designed featuring porphyrins,<sup>31</sup> phthalocyanines,<sup>32</sup> subphthalocyanines<sup>33</sup> and other chromophors as light-harvesting electron donors and fullerenes as electron acceptors. All mentioned provide a versatile toolbox for tuning the photophysical properties in terms of the type of process (photoinduced energy/electron transfer), the nature of the interactions between the electroactive units (through bond or space), and the kinetics of the formation/decay of the photo-generated species. Noteworthy, the preparation of multicomponent systems with tunable photophysical properties and highly ordered nanoarchitectures may assist in enhancing high charge mobilities. In this context, the use of Pcs and fullerenes may result in the preparation of intriguing one- and two-dimensional materials with improved self-assembling and conducting properties. In this chapter, recent progress in the construction of covalent and supramolecular systems comprising Pcs will be summarized, with a particular emphasis on their photoinduced and aggregation behaviors. It is believed that the high degree of control achieved in the preparation of Pc-C<sub>60</sub> systems, together with the increasing knowledge of the factors governing their photophysics, will allow for the design of next-generation light-fueled electroactive systems. Possible implementation of these structures in high performance devices is envisioned, finally turning into reality much of the expectations generated by these materials.

---

<sup>29</sup> a) E. E. Maroto, M. Izquierdo, S. Reboredo, J. Marco-Martinez, S. Filippone, N. Martin, *Acc. Chem. Res.*, **2014**, *47*, 2660-2670; b) M. Garcia-Borras, et al., *Chem. Soc. Rev.*, **2014**, *43*, 5089-5105; c) J. L. Delgado, et al., *Chem. Commun.*, **2010**, *46*, 4853-4865; d) A. Hirsch in *The Chemistry of the Fullerenes*, John Wiley & Sons, **2008**, pp. 1-215.

<sup>30</sup> a) M. Rudolf, S. V. Kirner, D. M. Guldi, *Chem. Soc. Rev.*, **2016**, *45*, 612-630; b) J. Zhang, S. Stevenson, H. C. Dorn, *Acc. Chem. Res.*, **2013**, *46*, 1548-1557; c) M. Rudolf, et al., *Chem. Eur. J.*, **2012**, *18*, 5136-5148.

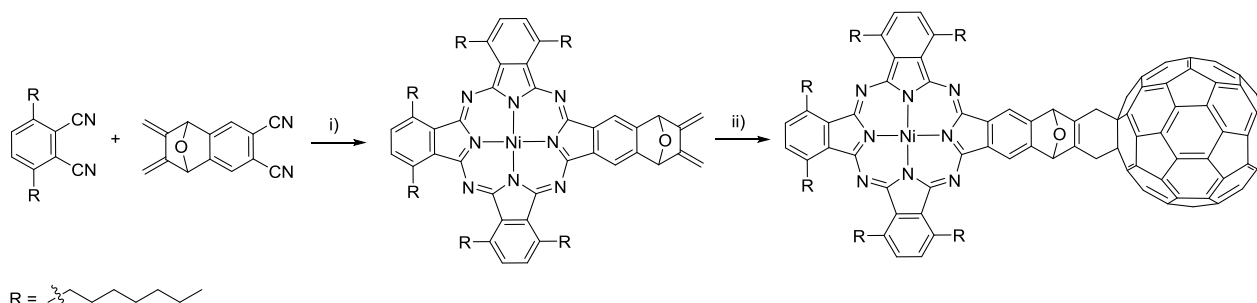
<sup>31</sup> a) T. Hasobe in *Handbook of Carbon Nano Materials* (Eds.: F. D'Souza, K. M. Kadish, **2012**, *4*, 95-130; b) O. Ito, F. D'Souza, *Molecules*, **2012**, *17*, 5816-5835; c) S. Fukuzumi, T. Kojima, *J. Mat. Chem.*, **2008**, *18*, 1427-1439.

<sup>32</sup> a) M. Lederer, U. Hahn, J. Fernandez-Ariza, O. Trukhina, M. S. Rodriguez-Morgade, C. Dammann, T. Drewello, T. Torres, D. M. Guldi, *Chem. Eur. J.*, **2015**, *21*, 5916-5925; b) G. Bottari, M. Urbani, T. Torres in *Organic Nanomaterials: Synthesis, Characterization, and Device Applications* (Eds.: T. Torres, G. Bottari), John Wiley & Sons, Inc., Hoboken, New Jersey, **2013**, pp. 163-187; c) G. Bottari, J. A. Suanzes, O. Trukhina, T. Torres. *J. Phys. Chem. Lett.*, **2011**, *2*, 905-913.

<sup>33</sup> a) H. M. Rhoda, M. P. Kayser, Y. Wang, A. Y. Nazarenko, R. V. Belosludov, P. Kiprof, D. A. Blank, V. N. Nemykin, *Inorg. Chem.*, **2016**, *55*, 9549-9563; b) M. Rudolf, O. Trukhina, J. Perles, L. Feng, T. Akasaka, T. Torres, D. M. Guldi. *Chem. Sci.*, **2015**, *6*, 4141-4147; c) D. Gonzalez-Rodriguez, et al., *J. Am. Chem. Soc.* **2010**, *132*, 16488-16500.

### 1.2.3 Covalently-linked Pc-C<sub>60</sub> systems

Organic chemistry offers a wide range of synthetic strategies for the preparation of covalently-connected Pc-C<sub>60</sub> systems. The first report on covalently connected Pc-C<sub>60</sub> molecular system appeared in 1997 by Hanack, Hirsch and coworkers, who prepared Pc-C<sub>60</sub> dyad through a Diels-Alder reaction between C<sub>60</sub> fullerene (*i.e.*, dienophile) and Ni(II)Pc bearing two terminal double bonds (*i.e.*, diene). This latter compound obtained by cyclotetramerization reaction of the corresponding phthalonitriles (Scheme 2).<sup>34</sup> The [4+2] cycloaddition occurs at a [6,6]-ring junction of the C<sub>60</sub> fullerene cage, giving rise to the formation of Pc-C<sub>60</sub> dyad, named by the authors “green fullerene” due to the intense green color in solution imparted by the Pc chromophore.



**Scheme 2.** Synthesis of the first Pc-C<sub>60</sub> fullerene dyad. Conditions: i) Ni(OAc)<sub>2</sub>, DBU, 1-pentanol, reflux. ii) C<sub>60</sub> fullerene, toluene, reflux.

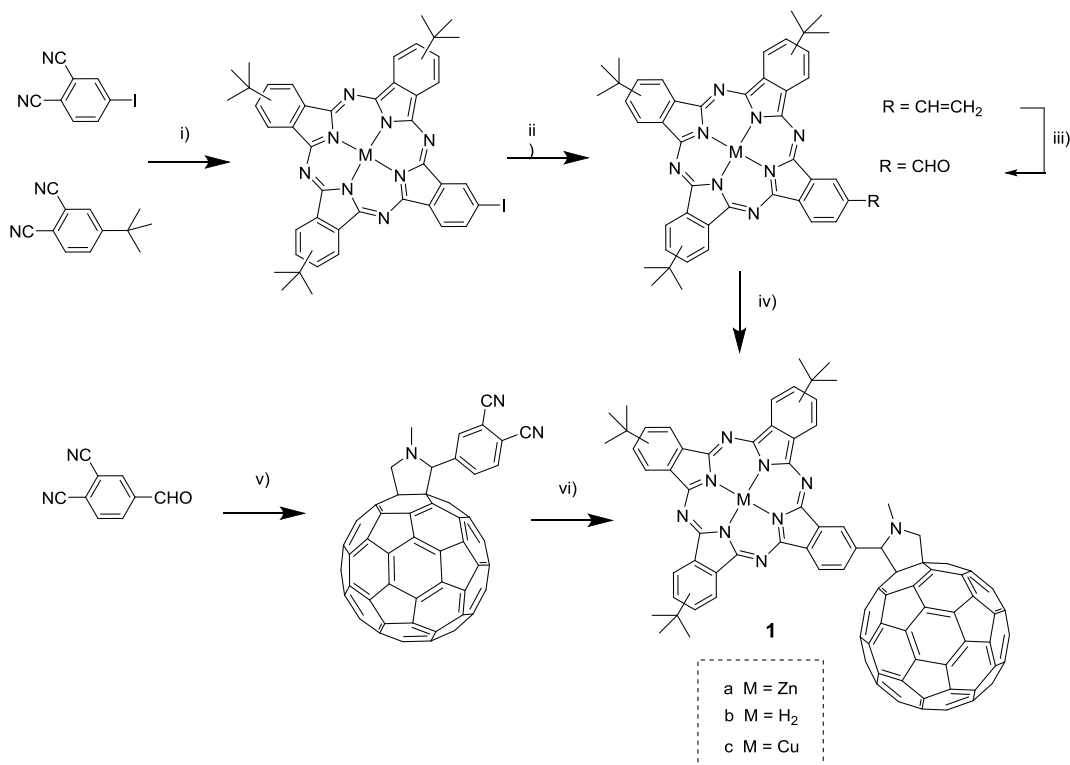
Since that first report, a large number of covalently-linked Pc-C<sub>60</sub> systems have been designed. Compounds **1a-c** became one of the most examined examples of covalently-connected systems constituted by a Pc and C<sub>60</sub> and were prepared by 1,3-dipolar cycloaddition reaction of azomethine ylides, generated *in situ* from formyl-Pcs and *N*-methylglycine, to C<sub>60</sub> fullerene, allowed to obtain Pc-C<sub>60</sub> dyads **1** in reasonable yields (*i.e.*, 40% (**1a**), 43% (**1b**), 41% (**1c**)) (Scheme 3).<sup>35</sup> This reaction (also known as “Prato reaction”) consists in the formation of a pyrrolidine macrocycle attached to a fullerene moiety and represents, nowadays, one of the mostly used synthetic strategies for the functionalization of fullerenes. An alternative synthetic route for the preparation of Pc-C<sub>60</sub> dyad **1a** has also been involved the preparation of 4-vinylphthalonitrile from 4-iodophthalonitrile, followed by the oxidative cleavage of the vinyl functionality to obtain 4-formylphthalonitrile (Scheme 3). The latter compound was then reacted with C<sub>60</sub> fullerene in the presence of *N*-methylglycine to

<sup>34</sup> T. G. Linssen, K. Duerr, M. Hanack, A. Hirsch, *J. Chem. Soc., Chem. Commun.*, **1995**, 103-104.

<sup>35</sup> a) A. Gouloumis, S. G. Liu, A. Sastre, P. Vazquez, L. Echegoyen, T. Torres, *Chem. Eur. J.* **2000**, *6*, 3600-3607; b) D. M. Guldi, I. Zilbermann, A. Gouloumis, P. Vazquez, T. Torres, *J. Phys. Chem. B.*, **2004**, *108*, 18485-18494.



afford the fullerene-containing phthalonitrile, which was subsequently condensed with 4-*tert*-butyl phthalonitrile in the presence of zinc (II) chloride, affording Pc-C<sub>60</sub> dyad **1a** in low yield.



**Scheme 3.** General reaction conditions for the preparation of Pc-C<sub>60</sub> dyads **1a-c**. i) ZnCl<sub>2</sub> or Cu(AcO)<sub>2</sub>, dimethylaminomethanol (DMAE), reflux, argon. For H<sub>2</sub>Pc: lithium, 1-pentanol, amyl alcohol, reflux, argon. ii) tributyl(vinyl)tin, Pd(PPh<sub>3</sub>)<sub>4</sub>, toluene, 100 °C. iii) OsO<sub>4</sub>, NaIO<sub>4</sub>, THF, room temperature. iv) C<sub>60</sub> fullerene, *N*-methylglycine, toluene, reflux. v) C<sub>60</sub> fullerene, *N*-methylglycine, toluene, reflux. vi) only for **1a**: 4-*tert*-butylphthalonitrile, ZnCl<sub>2</sub>, DMAE/*o*-DCB, reflux.

A detailed analysis on the photophysical properties (*i.e.*, steady-state and time-resolved fluorescence measurements and transient absorption measurements) of dyads **1a-c** in solution was carried out, confirming the occurrence of photo-induced electron transfer (PET) events.<sup>36</sup> Experimental evidence of long-lived CS in the solid state with lifetime several orders of magnitude higher than in solution and the first demonstration of working solar cell with dyad **1a** as active layer have been also reported, showing that the spin coating

<sup>36</sup> D. M. Guldi, A. Gouloumis, P. Vazquez, T. Torres, *Chem. Commun.*, **2002**, 2056-2057.

## Introduction

technique is efficient tool for preparation dyad-containing thin films, and that the morphology of the condensed phase is an important parameter to consider for photovoltaic applications.<sup>37</sup>

An amphiphilic Pc-C<sub>60</sub> conjugate **2** have also been prepared with the aim of stimulating the supramolecular organization of this dyad through a combination of  $\pi$ - $\pi$  stacking and hydrophilic/hydrophobic interactions (Figure 2a). The system comprised of a *tert*-butyl substituted Pc covalently linked to a fulleropyrrolidine moiety and beared a polyethylene glycol unit terminated with an ammonium function.<sup>38</sup> Interestingly, such an amphiphilic system is able to form aggregated species when dispersed in water, as demonstrated by UV-vis (Figure 2c) and light-scattering studies. Further insights into the morphology of these aggregates in water were gathered by transmission electron microscopy (TEM) studies in which the formation of uniform, micrometer long 1-D nanorods was be observed (Figure 2b). Interestingly, these nanotubules are reminiscent of those observed for a D-A, porphyrin-C<sub>60</sub> dyad.<sup>39</sup>

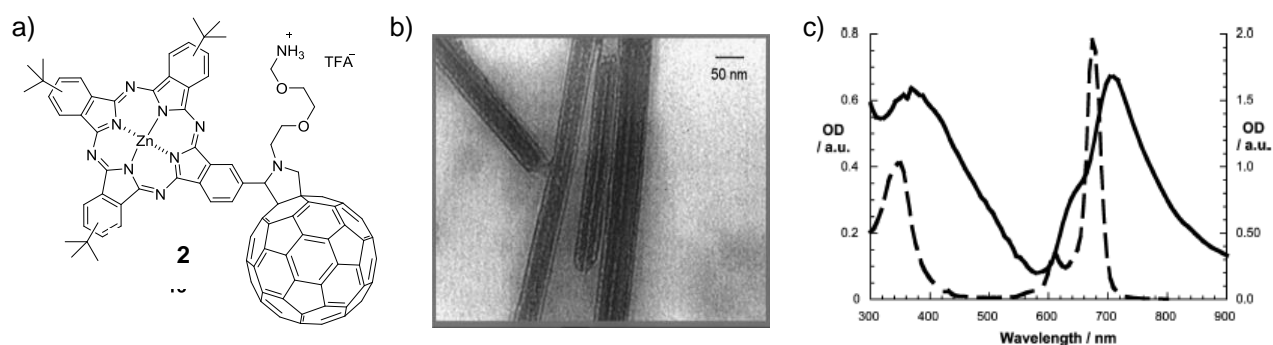


**Figure 2.** a) Molecular structure of Pc-C<sub>60</sub> dyad **2**. b) TEM image of the nanotubules formed by dyad **2** in water. c) Ground-state absorption spectra of Zn(II)Pc-C<sub>60</sub> Boc-protected (dashed spectrum) in THF and ZnPc-C<sub>60</sub> (solid spectrum) in H<sub>2</sub>O. Adopted with permission from J. Am. Chem. Soc., 2005, 127, 5811, copyright 2005, American Chemical Society (ACS).

<sup>37</sup> a) M. A. Loi, P. Denk, H. Hoppe, H. Neugebauer, C. Winder, D. Meissner, C.J Brabec, N. S. Sariciftci, A. Gouloumis, P. Vazquez, T. Torres, J Mater. Chem., **2003**, 13, 700-704; b) M. A. Loi, M. A. Loi, P. Denk, H. Hoppe, H. Neugebauer, D. Meissner, C. Winder, C. J. Brabec, N. S. Sariciftci, A. Gouloumis, P. Vazquez, T. Torres, Synth. Met. 2003, 137, 1491-1492.

<sup>38</sup> D. M. Guldi, A. Gouloumis, P. Vazquez, T. Torres, V. Georgakilas, M. Prato J. Am. Chem. Soc. **2005**, 127, 5811-5813.

<sup>39</sup> a) V. Georgakilas, F. Pellarini, M. Prato, D.M. Guldi, M. Melle-Franco, F. Zerbetto, Proc. Natl. Acad. Sci. U.S.A. **2002**, 99, 5075-5080; b) D. M. Guldi, G. M. A. Rahman, F. Zerbetto, M. Prato, Acc. Chem. Res. **2005**, 38, 871-878.

Steady-state and transient absorption studies showed that the self-organization ability of the amphiphilic ensemble **2** in water has a profound influence on the photophysical properties of these 1-D nano-objects. Particularly, transient absorption measurements on these nanotubules revealed the formation of a long-lived photoinduced charge-transfer product as inferred by the decay analysis of the radical pair species of this D-A supramolecular ensemble at 850 (i.e., Pc<sup>•+</sup>) and 1050 nm (i.e., C<sub>60</sub><sup>•-</sup>). For such a system, an impressive stabilization of more than 6 orders of magnitude was observed for the CS lifetime of self-assembled dyad **2** (i.e., 1.4 ms) with respect to a structurally related Pc-C<sub>60</sub> dyad which lacks the terminal ammonium unit and which is not able to form nanotubules (i.e., ~3 ns).

The use of supramolecular interactions for the “bottom-up” fabrication of Pc-C<sub>60</sub> nanoscale functional systems on solid surfaces has been recently exploited.<sup>40</sup> A structurally rigid, covalently-linked 2.8 nm long Pc-C<sub>60</sub> conjugate **3** (Figure 3) has been prepared, and its organization ability on highly ordered pyrolytic graphite (HOPG) and graphite-like surfaces has been investigated by using atomic force microscopy (AFM) and conductive AFM (C-AFM). The latter technique resulted to be a powerful tool for measuring electrical properties in nanostructured architectures. AFM studies revealed the formation of supramolecular fibers and films as a result of a combination of molecule-to molecule as well as molecule-to-substrate interactions, whereas C-AFM studies showed electrical conductivity values as high as 30  $\mu$ A for bias voltages ranging from 0.30 to 0.55 V (Figure 4). Control experiments revealed that the high electrical conductivity values recorded for the solid-supported, self-assembled Pc-C<sub>60</sub> conjugate are strongly related to the supramolecular order of the dyad within the nanostructures.

An idea about possible composition of these fibers could be taken from another recent work on a similar system (Figure 3c). Thus, a covalent Pc-C<sub>60</sub> dyad with a short and semiflexible bridge gave rise to a liquid crystalline material that exhibits efficient photocurrent generation and good short-range and long-range ambipolar charge transport properties.<sup>41</sup> Interestingly, preheated samples of this dyad showed a 5-fold increase in the charge mobility with respect to the unheated material, a phenomenon attributed to a better alignment of the Pc-C<sub>60</sub> units in columns upon thermal treatment, in turn, facilitating the charge transport.

---

<sup>40</sup> G. Bottari, D. Olea, C. Gomez-Navarro, F. Zamora, J. Gomez-Herrero, T. Torres, *Angew. Chem. Int. Ed.* **2008**, *47*, 2026-2031.

<sup>41</sup> H. Hayashi, W. Nihashi, T. Umeyama, Y. Matano, S. Seki, Y. Shimizu, H. Imahori, *J. Am. Chem. Soc.*, **2011**, *133*, 10736-10739.

## Introduction

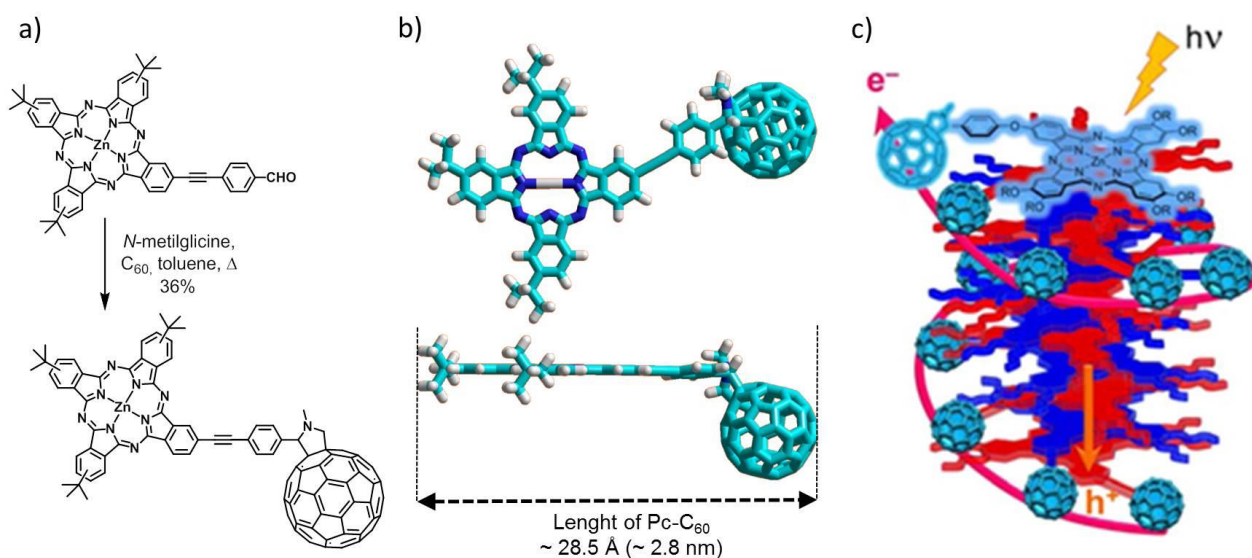


**Figure 3.** a) Molecular structure of Pc-C<sub>60</sub> conjugate 3, b) MM1 optimized structure of 3, c) Schematic representation of the columnar arrangement of liquid crystalline Pc-C<sub>60</sub> dyad. Reproduced with permission from *Acc. Chem. Res.*, 2015, 48, 900, copyright 2015, ACS.

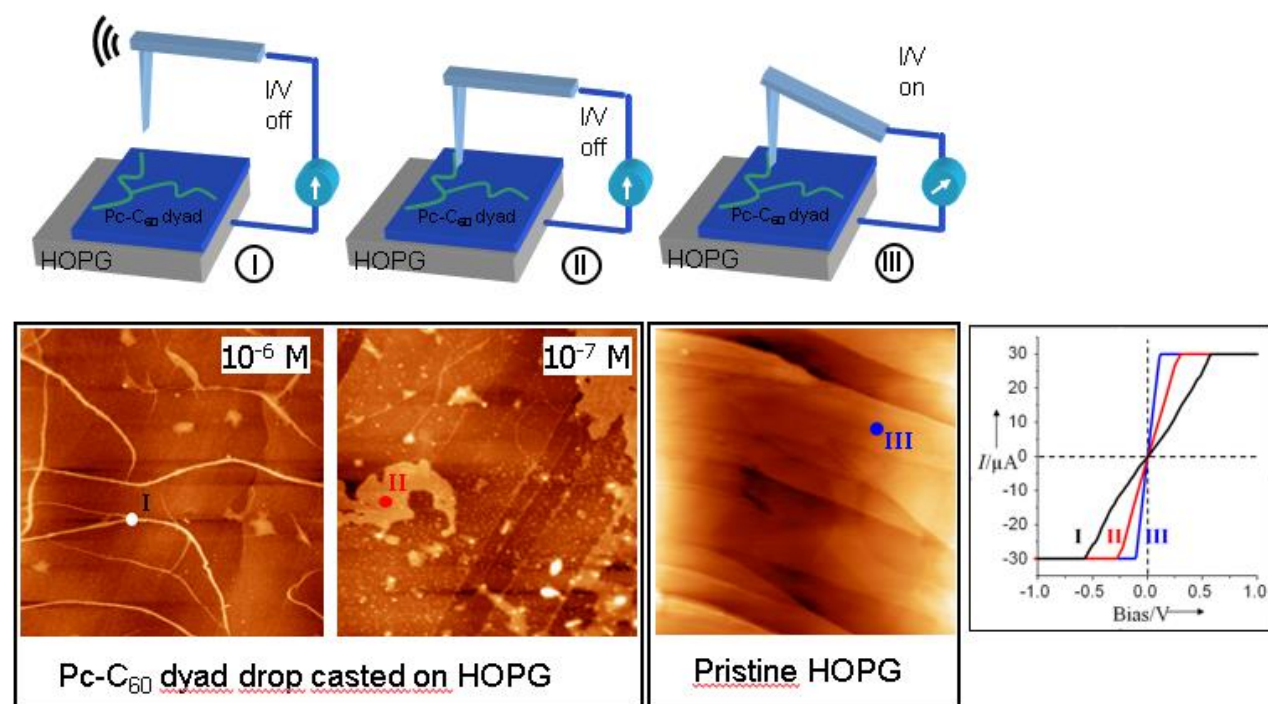


**Figure 4.** Conductive-AFM studies on HOPG. A region of the substrate is scanned with an AFM tip, when bias voltage is applied an electrical current flows through the dyad film. The  $I$ - $V$  values obtained for the fiber and the layer are very close to that of HOPG (an excellent electrical conductor with a very low resistivity), which is very remarkable for a supramolecularly-organized system. Adopted from Reference 120, by permission of John Wiley & Sons Ltd.

A different synthetic procedure toward the preparation of highly-ordered Pc-based systems was also utilized previously by Geerts and co-workers.<sup>42</sup> A mesogenic Pc-C<sub>60</sub> dyads **4a-d** were prepared by an esterification reaction between unsymmetrically substituted Pcs bearing a terminal alkoxy group and a fullerene derivative bearing a terminal acid moiety (Figure 5). However, UV-vis and electrochemical studies on these conjugates did not show any sign of ground-state electronic communication between the acceptor and the donor moieties.

The thermotropic properties of these dyads were studied by polarized optical microscopy and differential scanning calorimetry, revealing the formation of liquid-crystalline mesophases in the case of Pc-C<sub>60</sub> ensemble **4d**. These results suggest that in this series, a long linker is necessary in order to allow the bulky C<sub>60</sub> moiety to be accommodated in the columnar liquid-crystalline mesophase formed by the Pc macrocycles. No information on their charge-transport characteristics was given. Following the same strategy, a mesogenic Pc-C<sub>60</sub> dyad **5** has been reported by Torres and co-workers, which consisted of a hexadecyl-substituted Zn(II)Pc covalently connected through a flexible spacer to a C<sub>60</sub> fullerene via a Bingel-Hirsch cyclopropanation reaction (Figure 5).<sup>43</sup> Polarized optical microscopy and differential scanning calorimetry studies on this dyad revealed its liquid-crystalline behavior between 80 and 180 °C. Complementary XRD studies showed that **5** adopts a rectangular symmetry. Similarly, no studies on their charge-transport behavior were performed.

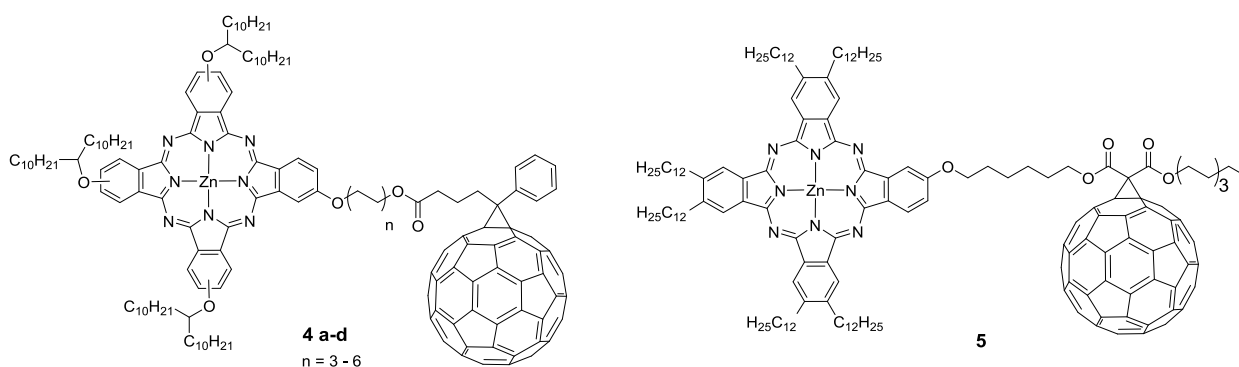


**Figure 5.** Molecular structures of mesogenic Pc-C<sub>60</sub> dyads **4** and **5**.

<sup>42</sup> Y. H Geerts, O. Debever, C. Amato, S. Sergejev, *Beilstein J. Org. Chem.* **2009**, *5*, 49.

<sup>43</sup> M. Ince, M. V. Martinez-Diaz, J. Barbera, T. Torres, *J. Mater. Chem.* **2011**, *21*, 1531-1536.

Optimization of the intermolecular  $\pi$ - $\pi$  stacking ordering and directions relative to the substrate represents a key issue towards enhancing charge transporting properties of organic semiconductors and, consequently, defines their performance in organic electronic materials and devices. It has been shown that  $\pi$ - $\pi$  stacking arrangements significantly improve the charge transporting properties of the active layer in organic solar cells (OSCs),<sup>44</sup> organic light emitting diodes (OLEDs),<sup>45</sup> and photodetectors.<sup>46</sup>

A straightforward solution-processed approach towards large-scale, ultra-dense and vertically standing  $\pi$ - $\pi$  stacks on indium tin oxide (ITO) substrate has been reported by Lu *et al.*<sup>47</sup> ZnPc with four terminal carboxylic functions armed through four amide groups has been used for the preparation of a face-on monolayer by anchoring ZnPc on ITO substrate (Figure 6a). Synergy of the  $\pi$ - $\pi$  stacking interactions and H-bonds involving amides and carboxyls caused the formation of coherent perpendicular  $\pi$ - $\pi$  stacks on the single molecular layer (Scheme 6a). AFM and SEM images suggested the typical diameter of the nanorods ranging from 30 to 45 nm, whereas TEM studies revealed the face-to-face packing of ZnPcs seen as a 1 nm-long horizontal lines within the rods (Figure 6b). The conductivity of the ZnPc nanorods was found to be of the order of  $10^{-3}$  S cm<sup>-1</sup>, as it is shown in the Figure 5c, approximately 100 times greater than that of an amorphous ZnPc film (av.  $2.0 \times 10^{-5}$  S cm<sup>-1</sup>). The hole mobilities were estimated from the space charge limited current region ( $I-V^2$ ) of the  $I-V$  curves, with the average value of  $2.9 \times 10^{-3}$  cm<sup>2</sup> V<sup>-1</sup> s<sup>-1</sup>, that is smaller than the reported values of  $10^{-2}$  to  $10^1$  cm<sup>2</sup> V<sup>-1</sup> s<sup>-1</sup>, typical for discotic liquid crystals and bulk crystals.<sup>48</sup> The linear dependence between conductivity/mobility values and the length of the nanorods indicated uniformity and reproducibility of their structures. Finally, ZnPc nanorod arrays were used as hole-transporting materials in OSCs with configuration of with the configurations of ITO|ZnPc|P3HT:PC<sub>61</sub>BM|Ca|Al, obtaining power conversion efficiencies comparable to those of the reference cell based on PEDOT:PSS

---

<sup>44</sup> a) C. Y. Chang, C. E. Wu, S. Y. Chen, C. H. Cui, Y. J. Cheng, C. S. Hsu, Y. L. Wang and Y. F. Li, *Angew. Chem. Int. Ed.*, **2011**, 50, 9386–9390; b) H. Imahori, T. Umeyama and S. Ito, *Acc. Chem. Res.*, **2009**, 42, 1809–1818.

<sup>45</sup> a) J. E. Anthony, *Chem. Rev.*, **2006**, 106, 5028–5048; b) A. P. Kulkarni, C. J. Tonzola, A. Babel and S. A. Jenekhe, *Chem. Mater.*, **2004**, 16, 4556–4573.

<sup>46</sup> a) H. L. Dong, H. F. Zhu, Q. Meng, X. Gong and W. P. Hu, *Chem. Soc. Rev.*, **2012**, 41, 1754–1808; b) B. Mukherjee, M. Mukherjee, *Org. Electron.*, **2011**, 12, 1980–1987.

<sup>47</sup> Z. Lu, Ch. Zhan, X. Yu, W. He, H. Jia, L. Chen, A. g Tang, J. Huang, J. Yao, *J. Mater. Chem.*, **2012**, 22, 23492–23496.

<sup>48</sup> a) S. Laschat, A. Baro, N. Steinke, F. Giesselmann, C. Hägele, G. Scalia, R. Judele, E. Kapatsina, S. Sauer, A. Schreivogel, M. Tosoni, *Angew. Chem., Int. Ed.*, **2007**, 46, 4832–4887; b) Y. Shirota, *J. Mater. Chem.*, **2000**, 10, 1–25.

(Figure 6b), and exceeding those of the cells fabricated with amorphous ZnPc powder, strongly suggesting the impact of oriented  $\pi$ - $\pi$  stacks of ZnPC on photovoltaic performance.

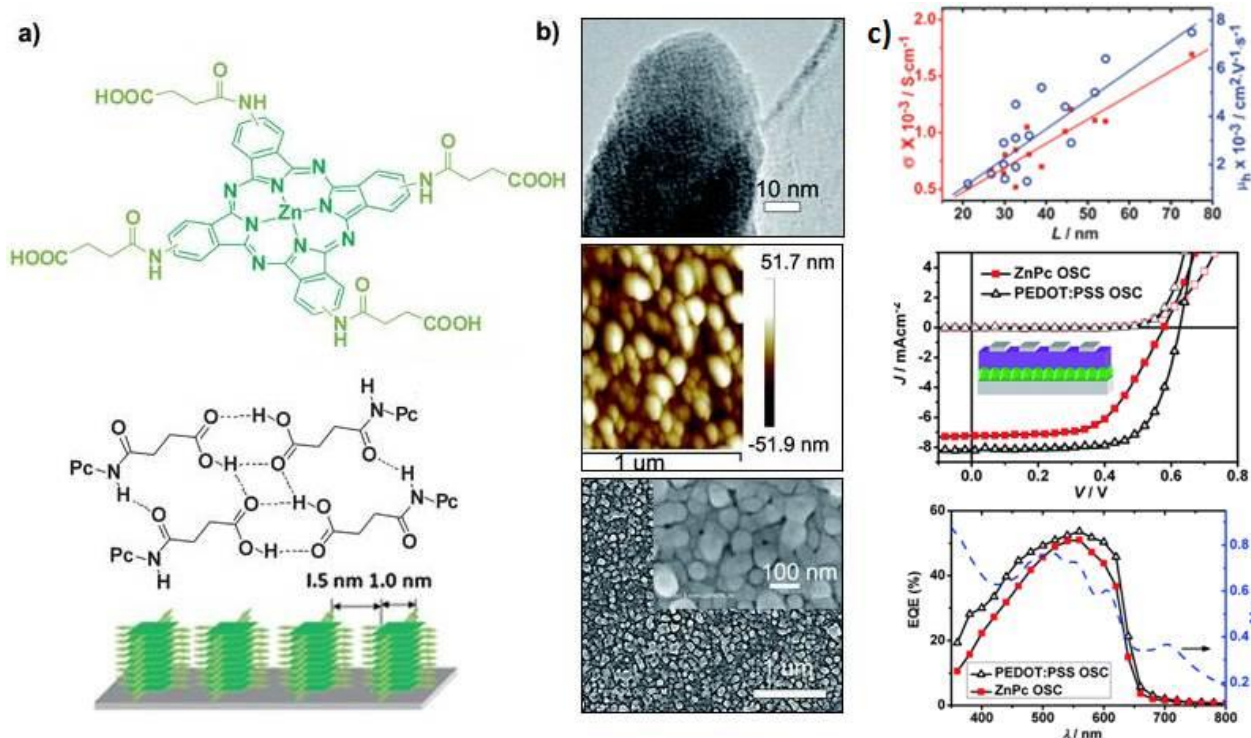


**Figure 6.** a) (Top) Molecular structure of ZnPc and (down) schematic representation of H-bonds and the  $\pi$ - $\pi$  stacks. b) (Top) TEM of a typical ZnPc nanorod, (middle) AFM and (down) SEM images of a dense nanorod-arrayed ZnPc film. c) (Top) Plots of the calculated conductivity and hole mobility vs. nanorod length, (middle) the  $J$ - $V$  curves and (down)  $EQE$  characteristics of OSCs based on the hole-transporting layer of a dense nanorod-arrayed ZnPc film. Dashed line shows the absorption spectrum of the film of a dense nanorod- ZnPc array (av. 36 nm) and P3HT:PCBM (av. 200 nm) on the ITO. Adopted from Reference 47 with permission from RSC.

Considering study of on-surface events for the Pc-based systems, the last recent example is worthy of mentioning. Thus, tunable photovoltage responses of Pc-C<sub>60</sub> dyads with modulated polarity have been described by Lemmetyinen *et al.*<sup>49</sup> The synthesized dyads had polar OH- tails either on the Pc electron donor side or on the fullerene electron acceptor side of the dyad (Figure 7a). The Pc-C<sub>60</sub> dyads were deposited successfully onto solid substrates as highly oriented phases using the Langmuir-Schäfer method (Figure 7b). For-

<sup>49</sup> J.Ranta, K. Kaunisto, M. Niskanen, A. Efimov, T. I. Hukka, H. Lemmetyinen, *J. Phys. Chem. C*, **2014**, 118, 2754–2765.

## Introduction

mation of a vertically oriented monolayer and the following electron transfer from the photoexcited phthalocyanine to fullerene was demonstrated by the time-resolved Maxwell displacement charge method. The electron transfer direction was found to be reversed for the dyads with reversed polarity (Figure 7c), demonstrating the ability to control charge transfer direction in the film.

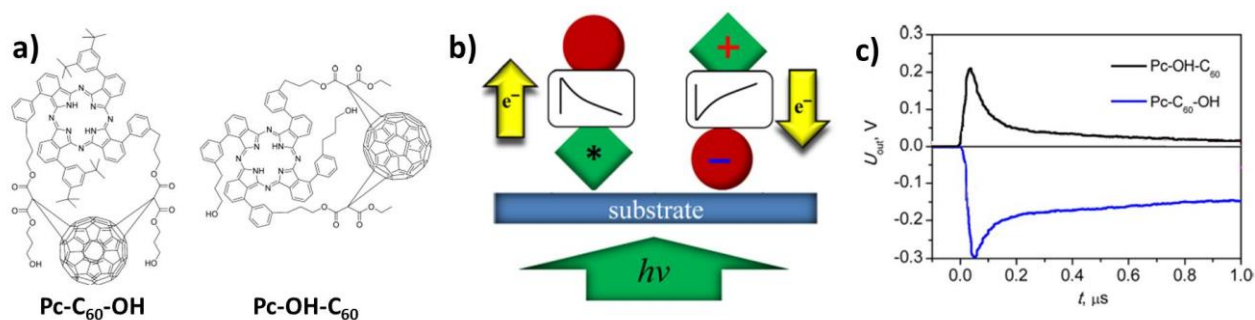


**Figure 7.** a) Molecular structures of ZnPc-based C<sub>60</sub> conjugates. b) Signal polarity in electron transfer experiments. c) Photovoltage responses of the dyad monolayers,  $\lambda_{\text{exc.}} = 720 \text{ nm}$  ( $U_{\text{bias}} = 0.5 \text{ V}$ ). Adopted with permission from J. Phys. Chem. C 2014, 118, 2754, copyright 2014, ACS.



## 1.3 DNA interstrand cross-linking on surface

### 1.3.1 Biosensors in cardiovascular diseases detection

According to The World Health Organization (WHO), cardiovascular disease (CVD) remains the leading cause of death in the world and Europe. By 2030 it is estimated that almost 23.6 million people in the world will die from CVDs, mainly from heart disease and stroke.<sup>50</sup> The latest data showed that CVD causes more than 4 million deaths each year in Europe, accounting for 45% of all deaths. Figure 8 shows the distribution of all woman deaths in Europe, the number of deaths from CVD is higher in women than men in Europe, with CVD accounting for 49% (2.2 million) of all deaths in women and 40% (1.8 million) of all deaths in men. Although many advances have been made in through early detection and treatment of CVD, it still remains the leading cause of death worldwide. The WHO informed that out of the 16 million deaths under the age of 70 are due to non-communicable diseases, 82% are in middle and low-income countries and 37% are caused by CVDs. During the World Economic Forum it was shown that in 2010 CVD represented 50% of non-communicable disease deaths and the estimated global cost of CVD was \$ 863 billion, and it is estimated to rise to \$ 1044 billion by 2030.<sup>51</sup>

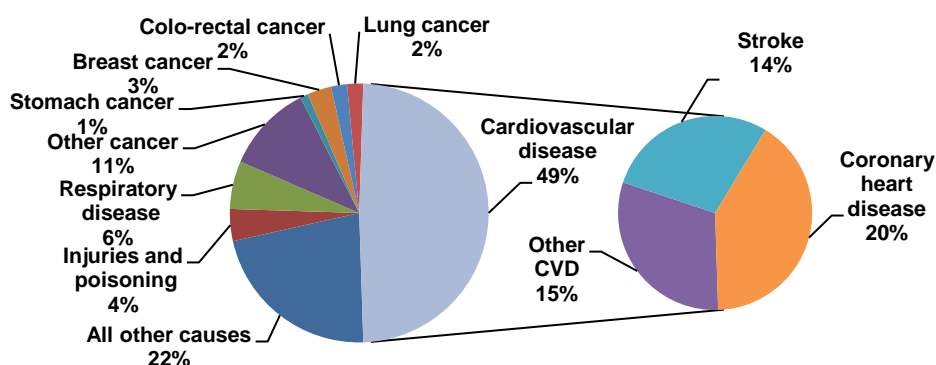


**Figure 8.** Representation of the proportion corresponding to women deaths in Europe.

<sup>50</sup> WHO, Cardiovascular Disease (CVDs) Fact Sheet, World Health Organisation, Mediacentre, 2011.

<sup>51</sup> a) Bloom, D.E., Cafiero, E.T., Jané-Llopis, E., Abrahams-Gessel, S., Bloom, L.R., Fathima, S., Feigl, A.B., Gaziano, T., Mowafi, M., Pandya, A., Prettner, K., Rosenberg, L., Seligman, B., Stein, A.Z., & Weinstein, C. "The Global Economic Burden of Noncommunicable Diseases", World Economic Forum, 2011; b) N. Townsend, L. Wilson, P. Bhatnagar, K. Wickramasinghe, M. Rayner and M. Nichols, "Cardiovascular disease in Europe: epidemiological update 2016", Eur. Heart J., 2016.

## Introduction

Thus, for many reasons CVD represents a considerable important social and clinical issue and effective preventive measures are necessary. By screening patients during the admission to the hospitals, the medical cost could be decreased by focussing the resources to those patients who have the special risk. Therefore, a rapid and more sensitive platform to fulfill the rapid diagnosis of CVD and the measurement of cardiac markers would play a key role in the diagnosis of CVD. Biosensors and biomarkers have a very important role in the diagnostic revolution of CVD diseases. The rapid advances in nanotechnology industry over the last years have resulted in the development of biosensors for diagnostics and many research groups are focussing on the development of new diagnostic devices as well as trying to enhance the existing immunological methods for the detection of cardiac markers,<sup>52</sup> which are biological analytes that can be detected in the blood upon the progression of a CVD disease.

The ideal cardiac biomarkers should be highly specific for cardiac tissue and absent from non-myocardial tissue as well as the need to be easily accessible to achieve high diagnostic sensitivity. For early diagnosis, small soluble molecules with rapid clearance from injured can be useful as suitable biomarkers. Nevertheless, a highly stable biomarker with a long plasma half-life is essential in the case of late diagnosis. As a result, peak levels should be reached relatively quickly and the biomarker should persist in circulation for a few hours.

Troponins are cardiac proteins. The Troponin complex has three subunits on the thin filament combined with myocardial contractile muscle to control the calcium ions bindings: cTnC (responsible for calcium binding), cTnT (the tropomyosin-binding) and cTnI (inhibits the ATPase activity of actomyosin). Cardiac muscle and skeletal muscle share troponin C isoforms, rendering this protein unsuitable for diagnostic use. Whereas, cTnI is found only in heart tissue and is not expressed in any type of skeletal muscle. Troponins T and I have unique cardiac isoforms and are considered the gold standard for the detection of myocardial injury (MI).<sup>53</sup> The complex formed by cTnI and cTnC is the predominant form

---

<sup>52</sup> a) B. McDonnell, S. Hearty, P. Leonard and R. O'Kennedy, *Clin. Biochem.*, **2009**, 42, 549-561; b) G.-J. Zhang, Z. H. H. Luo, M. J. Huang, J. A. J. Ang, T. G. Kang and H. Ji, *Biosens. Bioelectron.*, **2011**, 28, 459-463; c) Z. Altintas, W. M. Fakanya and I. E. Tothill, *Talanta*, **2014**, 128, 177-186; d) Q. Wang, F. Liu, X. Yang, K. Wang, H. Wang and X. Deng, *Biosens. Bioelectron.*, **2015**, 64, 161-164. e) B. Rezaei, M. Ghani, A. M. Shoushtari and M. Rabiee, *Biosens. Bioelectron.*, **2016**, 78, 513-523; f) D. Bhatnagar, I. Kaur and A. Kumar, *Int. J. Biol. Macromol.*, **2017**, 95, 505-510.

<sup>53</sup> a) P.G. Steg, S.K. James, D. Atar, L.P. Badano, et al., *Eur. Heart J.*, **2012**, 33, 2569–619; b) P.T. O'Gara, F.G. Kushner, D.D. Ascheim, et al., *J. Am. Coll. Cardiol.*, **2013**, 61, 78–140.

which comprises 95% of cTnI in human blood. The detection of unusual cTn levels occurs generally 4–6 h after the myocardial injury and remains in the blood for at least 7 days.

Heart-type fatty acid binding protein (hFABP) is a small heart protein located in the cytoplasm. It is also being expressed at low levels in extra-cardiac tissues including kidneys and skeletal muscle.<sup>54</sup> Because of its location and low molecular weight hFABP is released rapidly into the circulation right after (1-3 h) myocardial injury and is helpful in the early diagnosis of MI.<sup>55</sup> It is not useful for monitoring patients more than 6 h after first symptoms onset because its plasma clearance is relatively short,<sup>56</sup> usually the hFABP level can return to be normal within 24 hours.

The C-reactive protein (CRP) is an acute-phase protein reactant, which is released in response to acute injury, infection or inflammatory stimulation. CRP is the most widely used inflammatory biomarker. Because CRP induces the expression of adhesion molecules and other inflammatory cells, CRP also has pro-inflammatory effects. It has been shown that CRP can be useful to predict future cardiovascular events, including stroke, development of peripheral arterial disease and first-ever acute myocardial infarction (AMI).<sup>57</sup> Figure 9 shows the structure of the cardiac biomarkers described above.

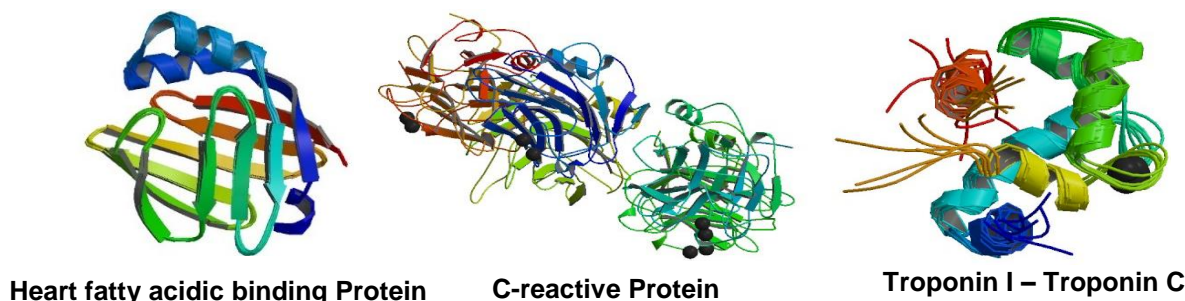


**Figure 9.** Crystal structure of heart fatty acidic binding protein,<sup>58</sup> human C-reactive Protein,<sup>59</sup> and cardiac troponin C - troponin I complex.<sup>60</sup>

<sup>54</sup> A. Colli, M. Josa, J. L. Pomar, C. A. Mestres and T. Gherli, *Cardiology*, **2007**, 108, 4-10.

<sup>55</sup> a) C. Carroll, M. Al Khalaf, J. W. Stevens, J. Leaviss, S. Goodacre, P. O. Collinson and J. Wang, *Emerg. Med. J.*, **2013**, 30, 280-286; b) R. Jankovic, et al., *BioMed Res. In.t*, **2015**, 8.

<sup>56</sup> G. Haltern, S. Peiniger, A. Bufe, G. Reiss, H. Gülker and T. Scheffold, *Am. J. Cardiol.*, **2010**, 105, 1-9.

<sup>57</sup> a) S. De Servi, M. Mariani, G. Mariani, A. Mazzone, *J. Am. Col. I Cardiol.*, **2005**, 46, 1496–502; b) S. J. Aldous, *Int. J. Cardiol.*, **2013**, 164, 282-294; c) D. del Val Martín, M. Sanmartín Fernández and J. L. Zamorano Gómez, *IJC Metab. Endocr.*, **2015**, 8, 20-23.

<sup>58</sup> C. Lücke, M. Rademacher, A. W. Zimmerman, H. T. van Moerkerk, J. H. Veerkamp and H. Rüterjans, *Biochem. J.*, **2001**, 354, 259-266 (RCSB PDB: 1G5W).

<sup>59</sup> A. K. Shrive, G. M. T. Gheetham, D. Holden, D. A. A. Myles, W. G. Turnell, J. E. Volanakis, M. B. Pepys, A. C. Bloomer and T. J. Greenhough, *Nat. Struct. Mol. Biol.*, **1996**, 3, 346-354 (RCSB PDB: 1GNH).

<sup>60</sup> M. X. Li, L. Spyrapoulos and B. D. Sykes, *Biochemistry*, **1999**, 38, 8289-8298 (RCSB PDB: 1MXL).

**Table 1.** Summary of clinically utilized cardiac biomarkers (MI: myocardial infarction). Adapted from Reference 51b with permission from RSC.

Cardiac biomarker	MW (kDa)	Clinical cut-off levels	Initial elevation above clinical cut-off (h)	Duration till peak elevation (h)	Duration of elevation	CVD indicator type	Biomarker Specificity
Troponin I	23.5	0.01–0.1 ng/ml	4–6	18–24	4–7 days	Detection of MI and tool for risk stratification	High: specifically increased following myocardial necrosis
h-FABP	15	6 ng/ml	1–3	6–8	24–36 h	Early detection of MI	Low: released following skeletal muscle injury, rapid clearance following necrosis and perceived increases due to compromised renal function
C-reactive Protein	125	< 1 µg/ml low risk, 1–3 µg/ml intermediate risk, >3–15 µg/ml high risk. Still no definitive consensus	No clinical consensus	No clinical consensus	No clinical consensus	CVD-related inflammatory response based biomarker	High: a large body of evidence to suggest a direct link between elevations above clinical cut-offs and recurrent ischemic events

*Biosensors* are one type of small devices for detecting target analytes that are usually biomolecules such as proteins, peptides and nucleic acids. Biosensors use biological molecules to recognize the target and employ output elements (so-called transducers) which are able to translate the biorecognition process into mass-sensitive, optical or electrical signals.

Biosensors are probably one of the most promising tools for a fast, cost effective and sensitive measurement which are used as a rapid screening tool to detect CVD at the earliest stage.<sup>61</sup> Immunosensors are biosensors with immunoreagents as sensing elements. These are principally antibodies immobilized in close contact with physicochemical transducers, for example, optical fibers and electrodes or free antibodies that bind to immobilized antigens. Optical, Electrochemical, piezoelectric, magnetic and thermometric transducers are the common types. Where the measurement of the analytes is achieved

<sup>61</sup> a) M. Mascini and S. Tombelli, *Biomarkers*, **2008**, 13, 637-657; b) E. B. Bahadır and M. K. Sezgentürk, *Anal. Biochem.*, **2015**, 478, 107-120; c) M.-I. Mohammed and M. P. Y. Desmulliez, *Lab. Chip*, **2011**, 11, 569-595; d) S. R. Shin, Y. S. Zhang, D.-J. Kim, A. Manbohi, H. Avci, A. Silvestri, J. Aleman, N. Hu, T. Kilic, W. Keung, M. Righi, P. Assawes, H. A. Alhadrami, R. A. Li, M. R. Dokmeci and A. Khademhosseini, *Anal. Chem.*, **2016**, 88, 10019-10027.

by the selective transduction of the receptor–target binding, obtaining a quantifiable electrical or optical binding signal as result. Immunosensors can achieve continuous detection of a broad variety of analytes. Electrochemical immunosensors are appropriate when on-site monitoring capabilities are required and they offer high sensitivity and selectivity due to the use of immunochemical interactions. Optical transducers include measuring fluorescence, optical density, surface plasmon resonance (SPR), or luminescence.

In colorimetric and fluorescence-based detection, either target or biorecognition molecule is labelled with a chromogenic or fluorescent tag, such as dyes. An enzyme can also be the label for the conversion of a colourless to a chromogenic substrate. The change of the colour/fluorescence intensity signal indicates the presence of the target molecules, which can be extremely sensitive and detect even a single molecule. There are also label-free detection methods, in those the target molecules are detected in their native forms and do not need a label, these methods allow quantitative/kinetic measurement of molecular interactions such as surface plasma resonance biosensors. One of the limitations of the immunochemical sensors is the cross-reactivity or interference, which depends on the type of the target analytes as well as the application of the immunosensor. Figure 10 shows some possible biosensors applications for the detection of biomarkers.

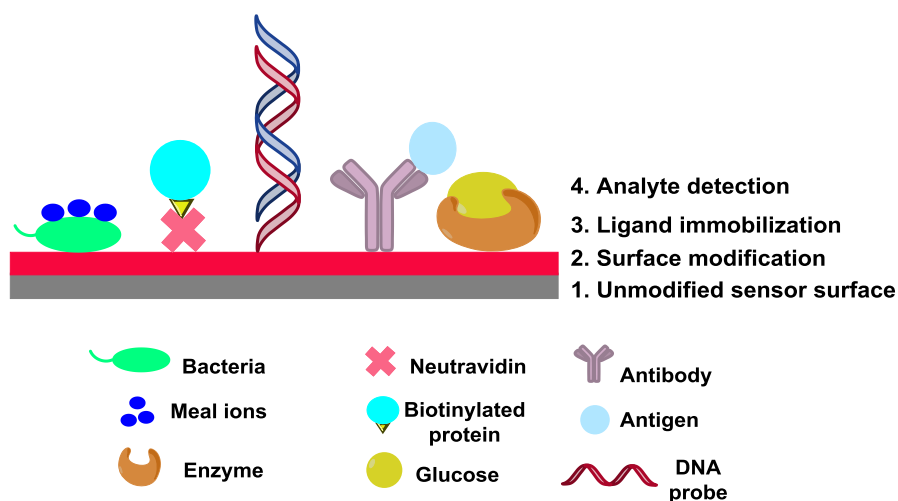


**Figure 10.** Examples of biosensor applications and possible surface modification.

## Introduction

The analysis of cardiac markers can be performed using antibody-based methods such as immunoassays. Originally, protein assays were developed in microtiter plate format for enzyme-linked immunosorbent assay (ELISA). ELISA is a method for quantification and detection of a specific analyte in a complex mixture. Within this method, the visualization of the target molecule is realized through a colour-generating enzyme which is covalently linked to a specific detection molecule such as an antibody. The colour formation is indirectly proportional to the concentration of the analyte and can be used for quantification by measuring the absorbance.

The major role in immunoassays is played by the antibodies. Those are produced by B-cells as part of the immune response that identifies and neutralizes foreign species such as pathogens. Antibodies have been used as recognition elements in immunoassay and subsequently immunosensor development due to their high specificity, affinity and versatility as well as their commercial availability. The antibodies which are derived from separate cell lines that recognize various regions on the immunogen are known as polyclonal antibodies, and those derived from single cell line are known as monoclonal antibodies. There are five major classes or isotypes of antibodies- IgG, IgD, IgE, IgA, and IgM, they are classed according to the heavy chain they contain – alpha, delta, epsilon, gamma or mu respectively. The IgG is the most abundant class in serum (70-80%), it is monomeric with a molecular weight of approximately 150 kDa. It is the major class of antibody of the secondary immune response and has the longest half-life (20-24 days). For the detection of proteins, there are four main types of immunoassay protocols: direct, indirect, competitive, and sandwich immunoassays.

Figure 11 shows the schematic illustrations of direct, indirect and sandwich immunoassays. The basic principles for the assays are similar and include the capture of the analyte of interest, blocking of the non-reacted surface, and addition of the detection component. In the case of competitive-direct assay, the analyte and an analyte-enzyme conjugate compete for the binding sites of the primary antibody. The indirect immunoassay format has the ability to improve the sensitivity of the detection. In competitive-indirect immunoassay the competition for the binding sites of the primary antibody is between the immobilized analyte-protein conjugate and the analyte in solution. In this method, the analyte of interest is bound to a specific antibody and after a labelled secondary antibody against this primary antibody is then added for detection. It is very important that the secondary antibody be raised in another species than the primary antibody to avoid non-specific binding.

In the sandwich immunoassay the unlabeled protein is sandwiched between two antibodies and then labelled specific detection antibodies are used to detect bound proteins.

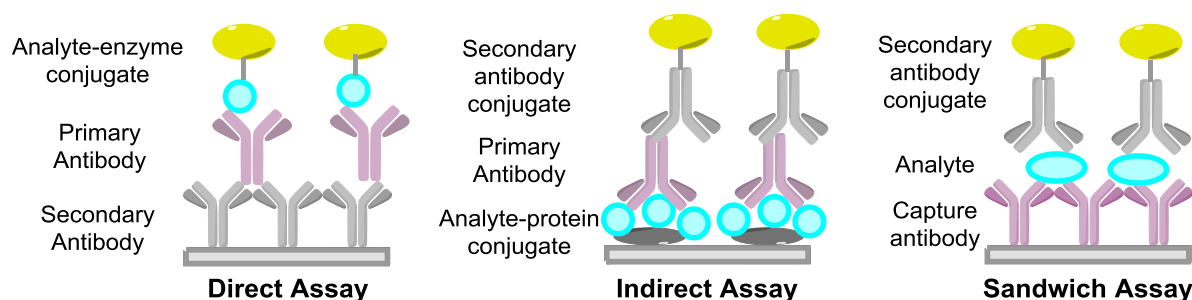


**Figure 11.** Schematic illustration of direct, indirect, and sandwich immunoassays.

Even though ELISA has been since long the standard for quantitative bioanalysis, this technique offers not enough throughput, due to lack of low multiplexing ability, and has high sample and reagents consumption. Therefore, the development of fast multiplex methods for the quantification of proteins is very important. Antibody microarrays may be a very useful tool for molecular diagnosis due to its ability to measure multiple proteins in complex mixtures using a small amount of sample. This multiple analysis can reduce false positive and negative results relative to the tests based on single markers. In Figure 12 are compared ELISA and microarray immunoassays.

In the microarray platforms, the antibody is immobilized on a chemically modified solid support in an array format for the following quantification of proteins in biological samples. Mostly, glass microscope slides are used as platforms and there are many commercially available different kinds of surface modification of glass slides. Generally, fluorescence signal can be achieved by using fluorophore-conjugated with the detection antibody or with streptavidin molecules, which binds to biotin-labeled detection antibodies to generate a fluorescent signal.

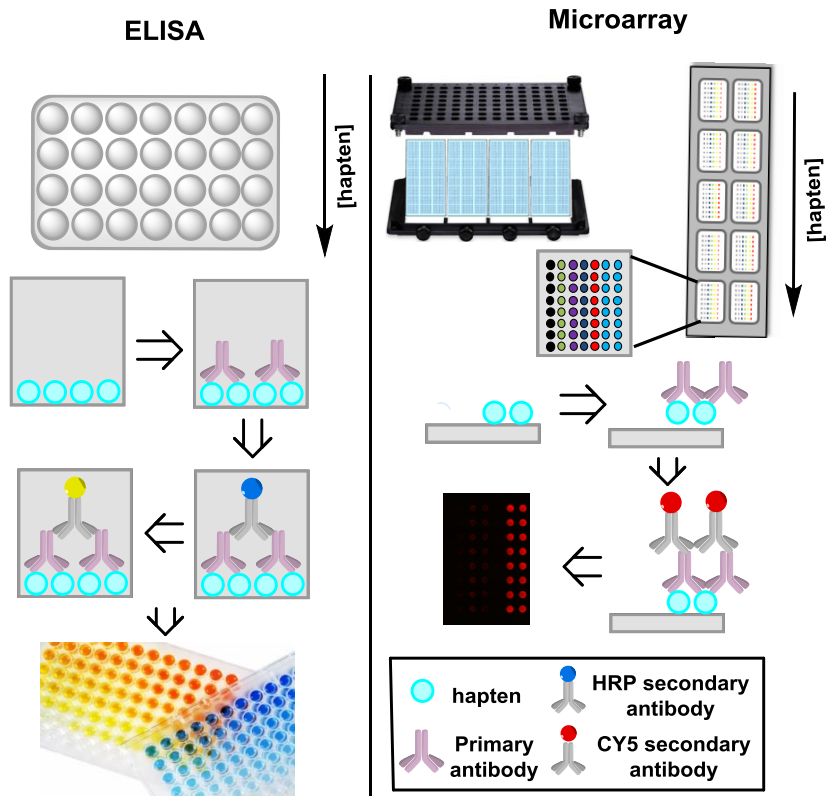
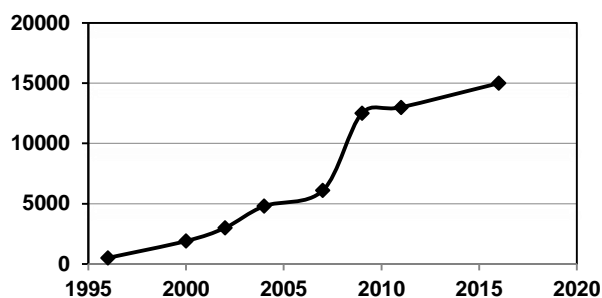


Figure 12. ELISA vs. protein microarray.



## 1.3.2 Biosensors and DNA in nanotechnology

During the last decade, nanotechnology has shown to have a clear impact on the development of biosensors. Biosensors have achieved great success both in the academic and commercial areas due to the need of multiplex applications that this versatile technology can have. Theranostics, defined as diagnostic test directly linked to the application of specific therapies, influence the development of biosensors since the pharmaceutical companies seek to deliver an efficacious therapeutic. The demand for more analytical data and facilitating that the patients can add data themselves is promoting the development of biosensors as well. The world market for biosensors estimated from several commercial sources over the last years and the prediction for the future is shown in the following Figure 13.<sup>62</sup>



**Figure 13.** Biosensors world market in million US dollars.

The boom in personal diagnostics is expanding the field to the development of new and inexpensive sensor platforms that are able to satisfy costumers' needs. Therefore, next generation diagnostics manufacturing is heading for creating complete sensing systems that can interface seamlessly with modern telecommunications. New technologies are focussing on fusion electronic printed systems and the future mobile technology such as smartphones. The research is becoming more and more interesting in the development of new sensors for the delivery of molecular information with high sensitivity and specificity avoiding the instability and cross-reactivity with other natural molecules present in the system to analyze. Currently, deoxyribonucleic acid (DNA), peptide, antibody, aptamers arrays, as well as molecularly imprinted polymers, are particularly promising tools within this research area. The opportunities for success are enhanced by the potential utility of some of these nanomaterials for novel diagnostic platforms. Synthetic biology analogs can

<sup>62</sup> A. P. F. Turner, *Chem. Soc. Rev.*, **2013**, 42, 3184-3196.

## Introduction

facilitate biochemical reactions in order to improve diagnostic processes by using self-assembled systems to build supramolecular structures.

It has been more than sixty years since the structure of DNA was first revealed in 1953 by Watson and Crick.<sup>63</sup> In 1962 they were awarded the Nobel Prize since their work established the chemical basis for discerning genetics. DNA is a long polymer of nucleotides and is formed by three different components: a heterocyclic base, a deoxyribose sugar, and a phosphate group. There are two purine bases, adenine (A) and guanine (G), and two pyrimidines, thymine (T) and cytosine (C) (Figure 14).

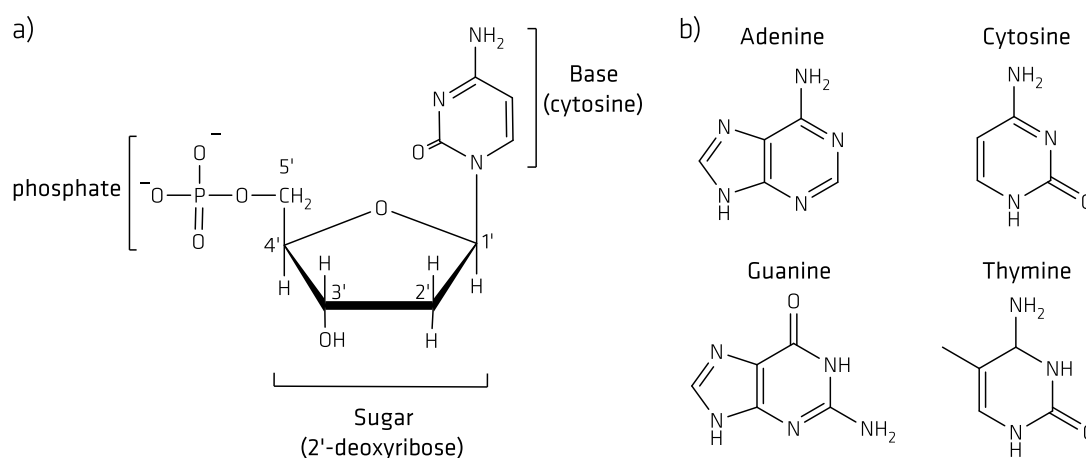


**Figure 14.** a) Nucleotide structure, the repeat unit of DNA. b) Purine and pyrimidine DNA bases.

To form the polynucleotide chain, the sugars are connecting by a 3'-5' phosphodiester linkage, which is a covalent bond formed between the 3'-hydroxyl group of one sugar and the 5'-hydroxyl of the next sugar (Figure 15a). The direction of the polynucleotide chain is given by the chemistry of the phosphodiester bond, from the 5'- to the free 3', the two strands of the duplex DNA are antiparallel, meaning that the strands are oriented in opposite directions. Figure 14b shows the base-pairing in DNA, the purine bases pair with the pyrimidine bases by hydrogen bonds, in this way the two units of backbones are pulled together and form the double helix structure.<sup>64</sup> The structure of the DNA double helix is shown in Figure 15c. The diameter of the molecule is 2 nm and one total rotation takes place every 3.4 nm, consisting of 10 - 10.5 base pairs (bp) which are separated by 0.34 nm. This classical form of the double helix is known as the B-form and represents the form found in cells. B and A-form are the most common type duplexes.

<sup>63</sup> J. D. Watson and F. H. C. Crick, *Nature*, **1953**, 4356, 737-738.

<sup>64</sup> J. D. Watson, *The double helix*, **1968**.

The A type (11 bp/helical turn, 2.6 nm molecule diameter) of the helix is observed under conditions of low humidity or in solutions that contain organic solvents or high salt concentrations.

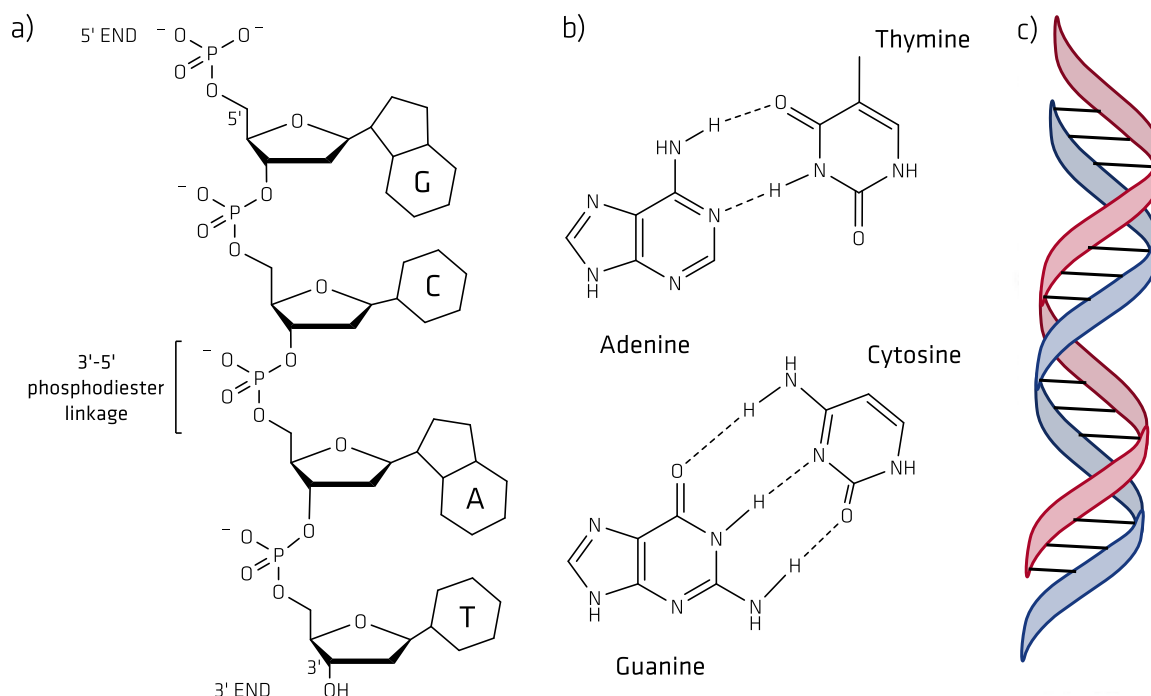


**Figure 15.** a) DNA polynucleotide chain b) Base-pairing of DNA bases, dotted lines represent hydrogen bonds. c) DNA double helix structure.

The double helix is a relatively stable structure due to its non-covalent interactions, the hydrogen bonds of the base pairs and the  $\pi$ - $\pi$  interactions of the stacked base pairs. This provides the thermodynamic stability of the double helix. Because of these relatively weak interactions, the two strands could separate easily during the DNA replication and transcription. When the double helix molecule is exposed to high temperature or pH conditions, the strands can be separated because the hydrogen bonds that hold both strands are broken, a process known as denaturation. Denaturation is reversible when the denatured DNA is slowly cooled, as single-stranded, complementary strands can reform double helices. This process is called renaturation, hybridization or annealing. The capacity of the DNA molecule to renature/denature allows the formation of artificial hybrid DNA and is the basis for several fundamental techniques in molecular biology like DNA addressable arrays and Southern blot. The DNA denaturation and hybridization can be monitored by measuring the absorbance of ultraviolet light of a DNA solution. DNA absorbs ultraviolet light maximally at a wavelength of 260 nm, the bases are responsible for this absorption. Upon denaturation the absorption of light at 260 nm by DNA increases, this is called hyperchromic

## Introduction

effect. When complementary DNA reforms the duplex structure its absorbance at 260nm decreases, the so-called hypochromic effect. The temperature at which half of the DNA molecule is denatured or unwound is the melting temperature  $T_m$ .<sup>65</sup> DNA goes through a transition from a very well ordered double-helical structure to a much less ordered single-stranded structure. The sharpness of the increase in absorbance at the  $T_m$  indicates that the denaturation and renaturation processes are highly cooperative, a zipper-like process. Renaturation probably occurs as a slow nucleation process, a relatively small stretch of DNA bases of one strand pair with its complement on the corresponding complementary strand. After this, the remainder of the two strands is very quickly zipped up from the nucleation site to reform the double helix.

The base composition of each DNA molecule affects the  $T_m$  and is mostly determined by the Guanine-Cytosine (GC) content and the ionic strength of the solution. The higher the percent of GC base pairs in the DNA, the higher the  $T_m$ . The reason of this is because it takes more heat energy to break three hydrogen bonds of a GC base pair than the two hydrogens bonds of an AT base pair. An increase of the  $T_m$  also occurs at a higher salt concentration (high ionic strength) of the solution; The phosphoryl groups of the DNA backbone carry negative charges. If these charges are not shielded, they can induce that the strands repel each other when the two DNA strands are close and facilitate their separation. At high ionic strength, these negative charges are shielded by cations and by that, they are stabilizing the double helix. Automated DNA synthesis allows the introduction of chemical modification in oligonucleotides in a site-specific and efficient way.<sup>66</sup>

DNA has become a popular material in nanotechnology due to its previously described specific properties of structural stability, self-direction and the possibility to modify DNA sequences.<sup>67</sup> The advantage of the DNA for being easily assembled makes this molecule a useful tool for the design and fabrication of nanostructures.<sup>68</sup> DNA has been employed to build structures in different dimensions with several geometries. To construct dynamic nanoscale structures with different features most of the scientists have used the bottom-

---

<sup>65</sup> Burton E. Tropp, "Molecular Biology, genes to proteins", 4th edition, *Jones & Bartlett Learning*, **2012**.

<sup>66</sup> S. L. Beaucage and R. P. Iyer, *Tetrahedron*, **1993**, 49, 1925-1963.

<sup>67</sup> a) M. Zahid, B. Kim, R. Hussain, R. Amin and S. H. Park, *Nanoscale Res. Lett.*, **2013**, 8, 1-13; b) Y. Krishnan and F. C. Simmel, *Angew. Chem. Int. Ed.*, **2011**, 50, 3124-3156; c) J. J. Thiaville, et al., *Proc. Natl. Acad. Sci. USA*, **2016**, 113, E1452-E1459.

<sup>68</sup> a) N. C. Seeman, *Annu. Rev. Biochem.*, **2010**, 79, 65-87; b) D. Han, S. Pal, Y. Yang, S. Jiang, J. Nangreave, Y. Liu and H. Yan, *Science*, **2013**, 339, 1412-1415; c) V. Linko, et al., *Sci. Rep.*, **2015**, 5, 15634; d) S. Krishnan, et al., *Nat. Commun.*, **2016**, 7, 12787.

up approach of self-assembly.<sup>69</sup> DNA-based nanostructures allow to carry or organize peptides, proteins, viral capsids, carbon nanotubes as well as nanoparticles in a controllable manner, obtaining a nanomaterial with novel properties and function.<sup>70</sup> Several research disciplines in the field of DNA nanotechnology are identified in Figure 16.

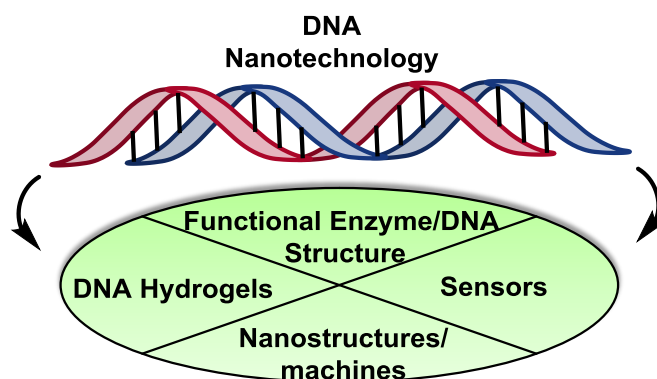


**Figure 16.** Representation of different areas bases on DNA nanotechnology.

DNA biosensors/genosensors and DNA chips/biochips/microarrays can allow sensitive and fast detection of DNA hybridization. In the DNA biosensors, the ODN probe is immobilized onto a transducer surface and allows single-shot measurements. On the contrary, DNA chips allow a multiple parallel detection in a single experiment on the surface which can be of silicon, plastic or glass. DNA based chips are an important tool for the high-throughput analysis on surfaces.<sup>71</sup>

A high sensitive DNA chip development depends on two factors: the method used for the immobilization of the probes (short ODN, 20-30mer; long ODN, 60-70mer), which should provide reproducibility of the attachment chemistry, and the good accessibility of the probes to the targets DNA.<sup>72</sup> The probes are pre-synthesized and then spotted on the surface chip by contact or non-contact printing.

<sup>69</sup> a) R.N. Kallenbach, et al., *Nature*, **1983**, 305, 829–831; b) A.V Pinheiro, D. Han D, W. M. Shih, H. Yan, *Nat. Nanotechnol.*, **2011**, 6, 12, 763–772; c) F. Wang, et al., *Chem. Rev.*, **2014**, 114, 2881-2941.

<sup>70</sup> a) N. Stephanopoulos, M. Liu, G.J. Tong, Z. Li, Y. Liu, H. Yan, M. B. Francis, *Nano. Lett.*, **2010**, 10, 2714–2720; b) R. Chhabra, J. Sharma, Y. Ke, Y. Liu, S. Rinker, S. Lindsay, H. Yan, *J. Am. Chem. Soc.*, **2007**, 129, 10304–10305; c) W.-W. Zhao, J.-J. Xu and H.-Y. Chen, *Chem. Rev.*, **2014**, 114, 7421-7441; d) W. Wang, et al., *Nucleic Acids. Res.*, **2016**, 670.

<sup>71</sup> a) A. S. Krylov, O. A. Zasedateleva, D. V. Prokopenko, J. Rouviere-Yaniv, A. D. Mirzabekov, *Nucleic Acids Res.*, **2001**, 29, 2654–2660; b) H. Ravan, et.al, *Anal. Biochem.*, **2014**, 444, 41-46; c) B. S. Nimse, et al., *Int. J. Mol. Sci.*, **2013**, 14, 5723-5733.

<sup>72</sup> a) P. Kumar, S. K. Agrawal, A. Misra, K. C. Gupta, P. Kumar, *Bioorg. Med. Chem. Lett.*, **2004**, 14, 1097-1099; b) A. Sassolas, et al., *Chem. Rev.*, **2008**, 108, 109-139.

## Introduction

Many immobilization techniques for fabrication of DNA chips have been developed and optimized to obtain high reactivity, stability and accessibility of the probes in order to increase the sensitivity of the detection methods.<sup>73</sup> The main techniques to immobilize ODNs are presented in Figure 17.

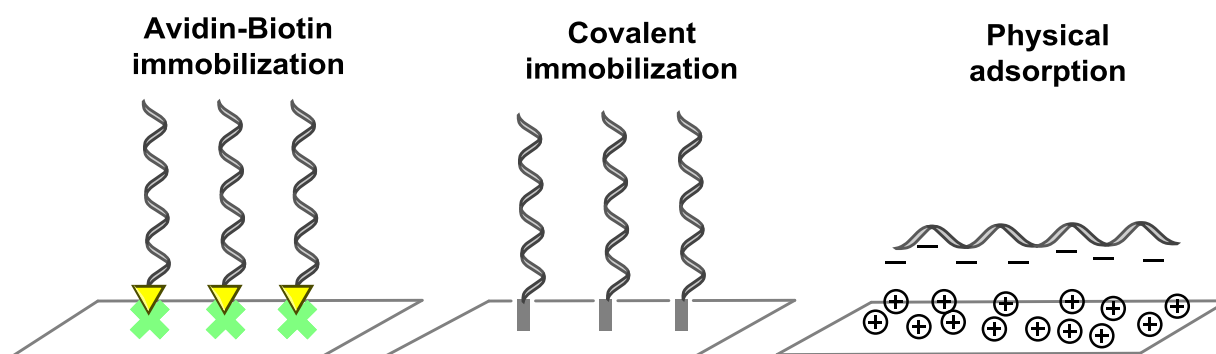


**Figure 17.** DNA immobilization techniques.

Physical adsorption is based on the ionic interaction between the negatively charged ODN probe and the positive charges from the surface,<sup>74</sup> the technique has been used to develop DNA microarrays.<sup>75</sup> By using this technique, the ODN can form many contacts with different orientations, is randomly oriented and weakly attached to the surface. Due to the electrostatic interactions, the ODN can be easily removed during the assay conditions by changes in pH, temperature or by the different ionic strength of the buffer solutions used.

The immobilization by covalent attachment provides the necessary high stability. The silanol groups (SiOH) at the glass surface are modified to obtain nucleophilic (carboxyl, epoxy, aldehyde, isothiocyanate) or electrophilic (maleimide, mercaptosilane) functionalities, which then react with the amino or thiol groups of ODNs, respectively (Table 2).

<sup>73</sup> a) A. N. Rao, C. K. Rodesch, D. W. Grainger, *Anal. Chem.*, **2012**, 84, 9379-9387; b) K.-S. Song, S. Balasaheb Nimse, J. Kim, J. Kim, V.-T. Nguyen, V.-T. Ta, T. Kim, *Chem. Comm.*, **2011**, 47, 7101-7103; c) B. J. Hong, S. J. Oh, T. O. Youn, S. H. Kwon, J. W. Park, *Langmuir*, **2005**, 21, 4257-4261; d) S. Nimse, K. Song, M. Sonawane, D. Sayyed T. Kim, *Sensors*, **2014**, 14, 22208; e) A. Chiadò, C. Novara, A. Lamberti, F. Geobaldo, F. Giorgis and P. Rivolo, *Anal. Chem.*, **2016**, 88, 9554-9563.

<sup>74</sup> S. V. Lemeshko, T. Powdrill, Y. Y. Belosludtsev and M. Hogan, *Nucl. Acids Res.*, **2001**, 29, 3051-3058.

<sup>75</sup> S. D. Conzone and C. G. Pantano, *Materials Today*, **2004**, 7, 20-26.

**Table 2.** Functional groups for DNA immobilization with the corresponding ODN.

Surface modification	Group structure	ODN probe modification
Aldehyde	CHO	
Carboxyl	COOH	
Epoxy	CHCH <sub>2</sub> O	-NH <sub>2</sub>
Isothiocyanate	N=C=S	
Maleimide	HC <sub>2</sub> (CO) <sub>2</sub> NH	
Mecaptosilane	Si-R-SH	-SH

The interaction between biotin and all proteins from the avidin family (avidin, streptavidin, neutravidin) are useful in a wide variety of applications. Avidin proteins are composed of four identical subunits, each one being able to form a strong complex with biotin (vitamin H or B7) as it can be observed in Figure 18.

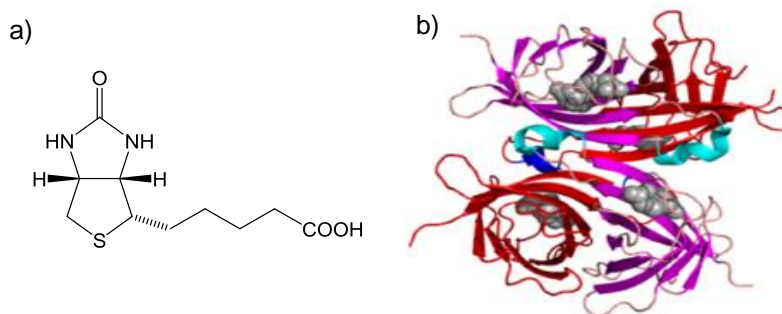
**Figure 18.** a) Biotin structure. b) Avidin-biotin complex formed with four biotin guests.<sup>76</sup>

Table 3 shows the comparison of the avidin proteins. Their association constant can be up to  $K_a = 10^{15} \text{ M}^{-1}$  and is comparable with covalent bonds. Avidin has a basic isoelectric point, therefore, at physiological pH, it is positively charged and can bind non-specifically to negatively charged molecules. Streptavidin and neutravidin are used more than avidin because their isoelectric points around 6 makes them more specific. Another good advantage of this system is that the carboxylic acid group of the biotin can be modified *via* ester or amide formation. This allows the easy biotinylation of antibodies, enzymes or amino-modified DNA strands.

<sup>76</sup> M. Holzinger, A. Le Goff, S. Cosnier, *New J. Chem.*, **2014**, 38, 5173-5180.

## Introduction

All previous outstanding properties result in the biotin–streptavidin/neutravidin system, an important tool for immobilization *via* affinity interactions on any kind of surfaces.<sup>77</sup>

**Table 3.** Comparison of biotin binding proteins.

	<b>Avidin</b>	<b>Streptavidin</b>	<b>Neutravidin</b>
Molecular Weight	67 K	53 K	60 K
Isoelectric point	10	6.8-7.5	6.3
Specificity	Low	High	Highest

The utilization of novel nanomaterials has promoted the study of DNA chips and biosensors towards the development of simple, inexpensive and smart detection of targets. But there are still some issues to improve the utilization of new magnification methods to decrease the limit of detection, new output signals to improve the existing detection methods, the enhancement of the assembly production of the DNA probes and targets to increase the sensitivity. In this concept, DNA nanotechnology provides new opportunities by allowing the modification of the properties of nucleic acids.

Protein microarrays are frequently used in several applications such as protein-protein interaction analysis, drug screening, and biomarker detection.<sup>78</sup> Even if the protein microarray has the ability to become an important tool for many diagnostics applications, its production is limited by the technical challenges related to microarray production, being the printing of the proteins on the microarray surface one of this challenges. The intensity of the signal obtained is related to the amount of analyte that is captured by the immobilized antibody, It is important that the antibody is attached to the surface with its binding sites oriented towards the solution.<sup>79</sup>

<sup>77</sup> a) T. Liebermann, W. Knoll, P. Sluka, R. Herrmann, *Colloids Surf. A.*, **2000**, 169, 337-350; b) C. Larsson, M. Rodahl, F. Höök, *Anal. Chem.*, **2003**, 75, 5080-5087; c) J. Ladd, C. Boozer, Q. Yu, S. Chen, J. Homola and S. Jiang, *Langmuir*, **2004**, 20, 8090-8095; d) X. Su, Y.-J. Wu, R. Robelek, W. Knoll, *Langmuir*, **2005**, 21, 348-353; e) C. M. Dundas, D. Demonte and S. Park, *Appl. Microbiol. Biotechnol.*, **2013**, 97, 9343-9353; f) A. Jain and K. Cheng, *J. Control. Release*, **2017**, 245, 27-40; g) Y. He and B. Jiao, *Talanta*, **2017**, 163, 140-145.

<sup>78</sup> a) G. Mac Beath and S. L. Schreiber, *Science*, **2000**, 289, 1760-1763; b) H. Sun, Grace Y. J. Chen and Shao Q. Yao, *Chem. Biol*, **2013**, 20, 685-699.

<sup>79</sup> a) P. Peluso, D. S. Wilson, D. Do, H. Tran, M. Venkatasubbaiah, D. Quincy, B. Heidecker, K. Poindexter, N. Tolani, M. Phelan, K. Witte, L. S. Jung, P. Wagner and S. Nock, *Anal. Biochem.*, **2003**, 312, 113-124; b) A. K. Trilling, J. Beekwilder and H. Zuilhof, *Analyst*, **2013**, 138, 1619-1627; c) I. Hospach, Y. Joseph, M. Mai, N. Krasteva and G. Nelles, *Microarrays*, **2014**, 3, 282.



Figure 19 shows the possible orientation of antibodies on solid surfaces and DNA-directed immobilization (DDI) strategy to enhance the immobilization.<sup>80</sup>

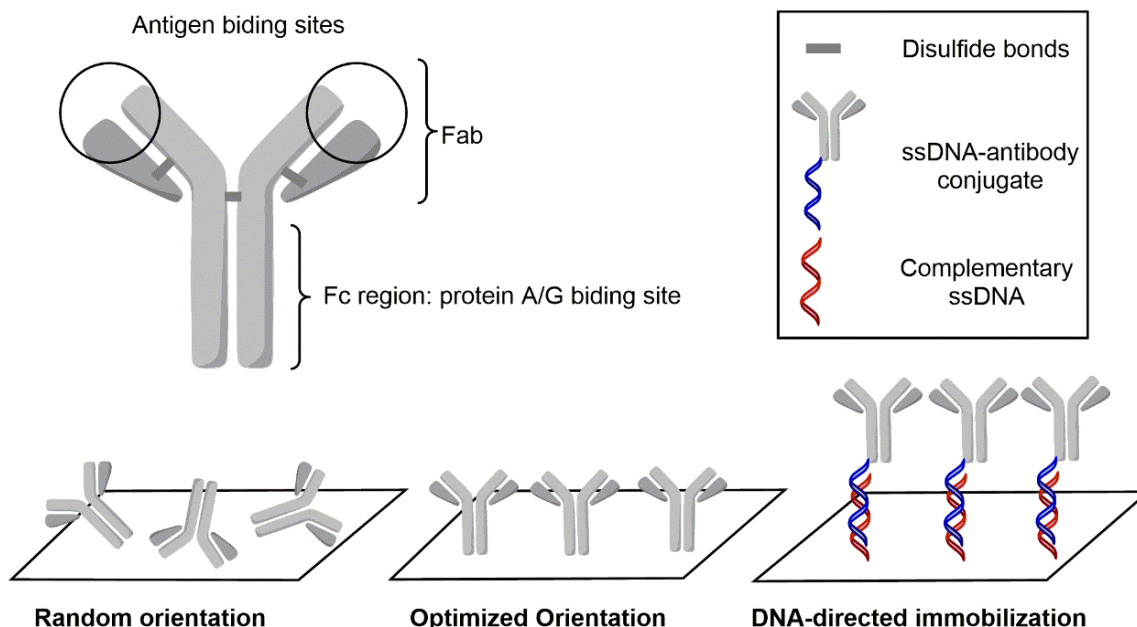


**Figure 19.** The structure of antibody (Fc: fragment, crystallizable, Fab: fragment, antigen binding, disulfide bridges and antigen binding sites are indicated) and some strategies for antibody immobilization.

Amine-reactive traditional surface chemistry, such as producing carboxyl, epoxy, aldehyde or isothiocyanate groups on surface can mask the antibody binding site due to multiple covalent interactions that are possible between the antibody and the surface groups.<sup>81</sup> Additionally, variable protein immobilization yields within and across microarrays, as well as inconsistency in the morphology and uniformity of printed microspots are parameters that affect the robustness and accuracy of the assay.<sup>82</sup>

<sup>80</sup> Y. Jung, J. Y. Jeong and B. H. Chung, *Analyst*, **2008**, 133, 697-701.

<sup>81</sup> H. Sun, Grace Y. J. Chen and Shao Q. Yao, *Chem. Biol*, **2013**, 20, 685-699.

<sup>82</sup> a) U. B. Nielsen and B. H. Geierstanger, *J. Immunol. Methods*, **2004**, 290, 107-120; b) S. L. Seurnck-Servoss, A. M. White, C. L. Baird, K. D. Rodland and R. C. Zangar, *Anal. Biochem.*, **2007**, 371, 105-115; c) V. Romanov, S. N. Davidoff, A. R. Miles, D. W. Grainger, B. K. Gale and B. D. Brooks, *Analyst*, **2014**, 139, 1303-1326.

## Introduction

Researchers have explored alternative methods of protein immobilization to address the mentioned issues and enhance the activity of the antibody to improve the sensitivity of the assay. The developments of bioconjugation techniques made possible the modification of the molecules to obtain versatile surface chemistries to immobilize proteins. DDI is one of those techniques which combines DNA microarrays with proteins for diagnostic purposes by using protein-DNA conjugates (Figure 20a), being the proteins covalently attached to a specific DNA sequence.<sup>83</sup> The antibodies are directed and immobilized on the surface via sequence specific DNA-DNA hybridization. Due to the DNA spacer between the immobilized molecule and the surface the antigen binding capacity of antibodies is enhanced by allowing a better orientation and decreasing the steric hindrance.<sup>79</sup> Moreover, DNA microarray production is less laborious than protein microarray fabrication due to easy optimization of DNA printing.<sup>84</sup>

The use of nucleic acid hybridization for directed immobilization of components on surfaces is not limited to proteins; with the aim to detect protein–ligand interactions it can also be applied to small molecules such as steroids,<sup>85</sup> for directing steroid-oligonucleotides on surface plasmon resonance (SPR) gold chip as is shown in Figure 20b. Colloidal compounds, such as metal nanoparticles can also be directed to a sensor surface by DDI.<sup>86</sup> Figure 20c). As well, DDI has proven to be a powerful tool for nucleic acid analyses and a versatile technique within the research and biomedical diagnostics fields.<sup>87</sup>

---

<sup>83</sup> a) C. M. Niemeyer, L. Boldt, B. Ceyhan, D. Blohm, *Anal. Biochem.*, **1999**, 268, 54-63; b) R. C. Bailey, et al., *J. Am. Chem. Soc.*, **2007**, 129, 1959-1967; c) A. L. Washburn, et al., *Anal. Chem.*, **2011**, 83, 3572-3580; d) C. Boozer, et al., *Anal. Chem.*, **2006**, 78, 1515-1519.

<sup>84</sup> a) H. H. Cao, N. Nakatsuka, A. C. Serino, W.-S. Liao, S. Cheunkar, H. Yang, P. S. Weiss and A. M. Andrews, *ACS Nano*, **2015**, 9, 11439-11454; b) J. Fredonnet, et al., *Microarrays*, **2016**, 5, 25; c) A. H. Loo, C. K. Chua and M. Pumera, *Analyst*, **2017**, 8, 15-28; d) R. Castagna, et al, *Langmuir*, **2016**, 32, 3308-3313.

<sup>85</sup> N. Tort, J. P. Salvador, A. Aviñó, R. Eritja, J. Comelles, E. Martínez, J. Samitier and M. P. Marco, *Bioconjugate Chem.*, **2012**, 23, 2183-2191.

<sup>86</sup> a) T. A. Taton, C. A. Mirkin and R. L. Letsinger, *Science*, **2000**, 289, 1757-1760; b) C. M. Niemeyer and U. Simon, *Eur. J. Inorg. Chem.*, **2005**, 3641-3655.

<sup>87</sup> a) N. L. Rosi and C. A. Mirkin, *Chem. Rev.*, **2005**, 105, 1547-1562; b) S. Nimse, K.-S. Song, J. Kim, D. Sayyed and T. Kim, *Int. J. Mol. Sci.*, **2013**, 14, 5723; c) R. Meyer, et al., *Curr. Opin. Chem. Biol.*, **2014**, 18, 8-15; d) M.-X. Chen, et al., *PLoS. Negl. Trop. Dis.*, **2016**, 10, 12; e) S P Flynn, et al., *Nanotechnology*, **2016**, 27, 465501.

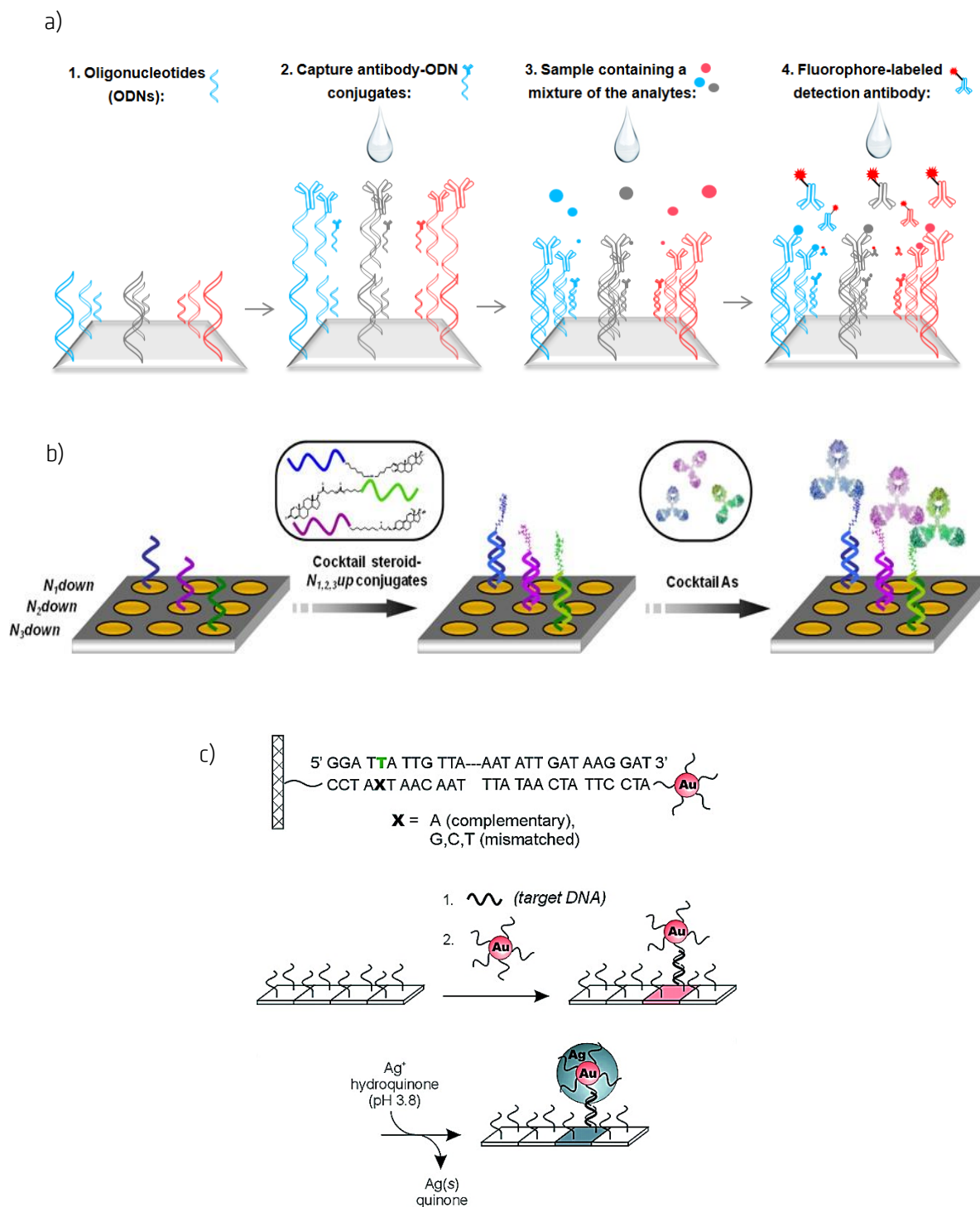


**Figure 20.** a) Scheme of DNA microarrays using protein-DNA conjugates, b) Schematic representation of functionalization of an SPR chip with steroid-oligonucleotide bioconjugates, c) DNA arrays using oligonucleotide-modified gold nanoparticle probes. With copyrights permissions of the ACS (b) and The American Association for the Advancement of Science (c).

### 1.3.3 Furan mediated DNA-ICL cross-linking

Many types of research are inspired by the toxicity of furan, which is classified by the International Agency for Research on Cancer as a possible human carcinogenic compound.<sup>88</sup> Furan is oxidized by cytochrome P450 to cis-2-butene-1,4-dialdehyde, which reacts with proteins<sup>89</sup> (amino acid side chains) and nucleosides<sup>90</sup> (exocyclic amines) (Figure 21).

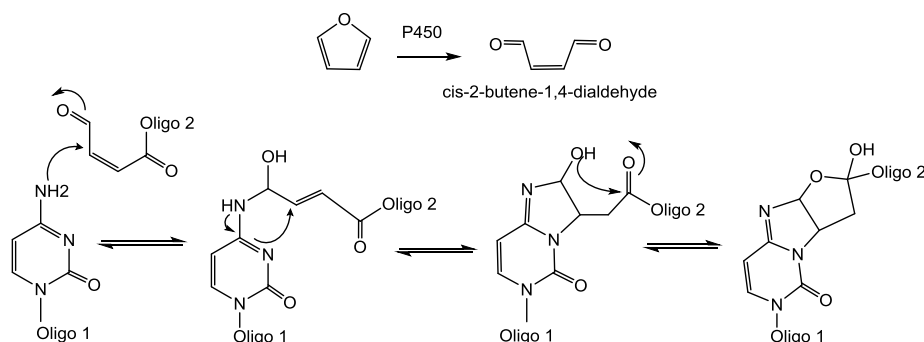


**Figure 21.** Cis-2-butene-1,4-dialdehyde product and the reaction mechanism with nucleosides.

A new cross-linking methodology has been developed by Halila and co-workers<sup>91</sup> (Figure 22). They observed a selective in situ oxidation of a furan unit incorporated in an oligonucleotide nucleoside, resulting in a fast site-specific cross-link formation between complementary oligonucleotide strands. Oxidation was achieved with N-bromosuccinimide (NBS).

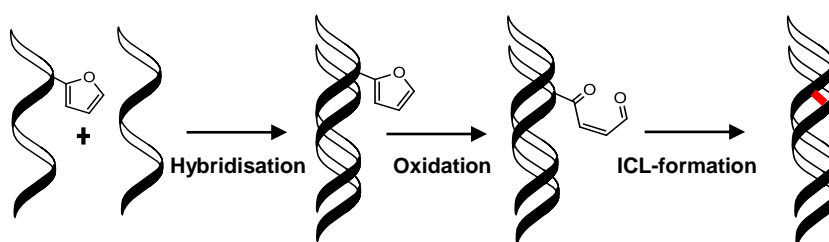


**Figure 22.** Furan-oxidation triggered DNA cross-linking. After hybridization with the right target, furan is selectively oxidized to a keto-butenal functionality which forms a covalent bond with the nucleophiles (exocyclic amines) of the complementary oligonucleotide sequence.

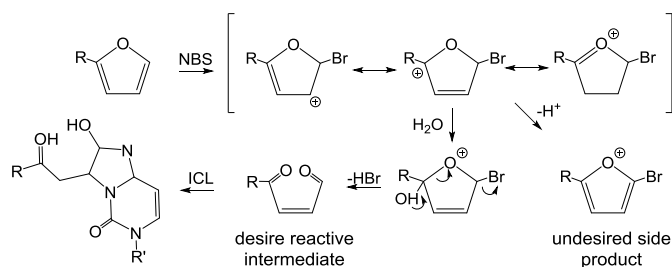
<sup>88</sup> International Agency for Research on Cancer. Dry-Cleaning, some Chlorinated Solvents and Other Industrial Chemicals. IARC Monographs on the Evaluation of Carcinogenic Risks to Humans, **1995**, 393-407.

<sup>89</sup> M. B. Phillips, M. M. Sullivan, P. W. Villalta, L. A. Peterson, *Chem. Res. Toxicol.*, **2014**, 27, 129-135.

<sup>90</sup> a) L. A. Peterson, *Drug Metab. Rev.*, **2006**, 38, 615-626; b) D. Verzele, L. Carrette, A. Madder, *Drug Discov. Today Technol.*, **2010**, 7, 115-123.

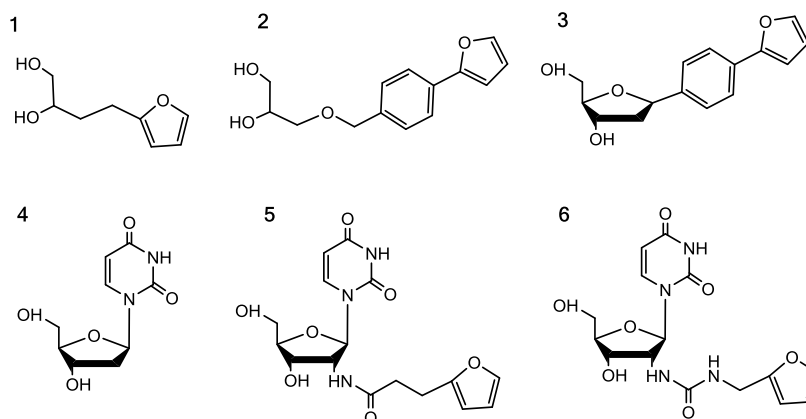
<sup>91</sup> S. Halila, T. Velasco, P. D. Clercq, A. Madder, *Chem. Commun.*, **2005**, 936-938.

Figure 23 shows the results of the furan oxidation using NBS and the ICL formation with a cytosine nucleoside. There is a competitive bromination reaction on the furan moiety, which occurs in the case of an extended aromatic system.<sup>92</sup>



**Figure 23.** Oxidation mechanism of furan with NBS and the undesired side reaction product.

DNA interstrand cross-link (ICL) formation possesses important clinical applications.<sup>93</sup> Therefore, the development of new ICL methodologies is an area of significant interest. A series of furan-modified building blocks were designed by the group of A. Madder in order to improve the furan cross-linking methodology by favouring the reaction of the keto-but-tenal with the nucleophiles of the complementary oligonucleotide sequence. Figure 24 shows the structures of some of these furan building blocks, which can be selected depending on the desired cross-link outcome, site selectivity or high cross-linking yield. Furan-modified nucleosides 1, 2, 3, and 4 formed cross-links both to complementary A or C bases. Building blocks 5 and 6 allowed a more selective cross-linking and only yielded a cross-linked product if a complementary C base was present.



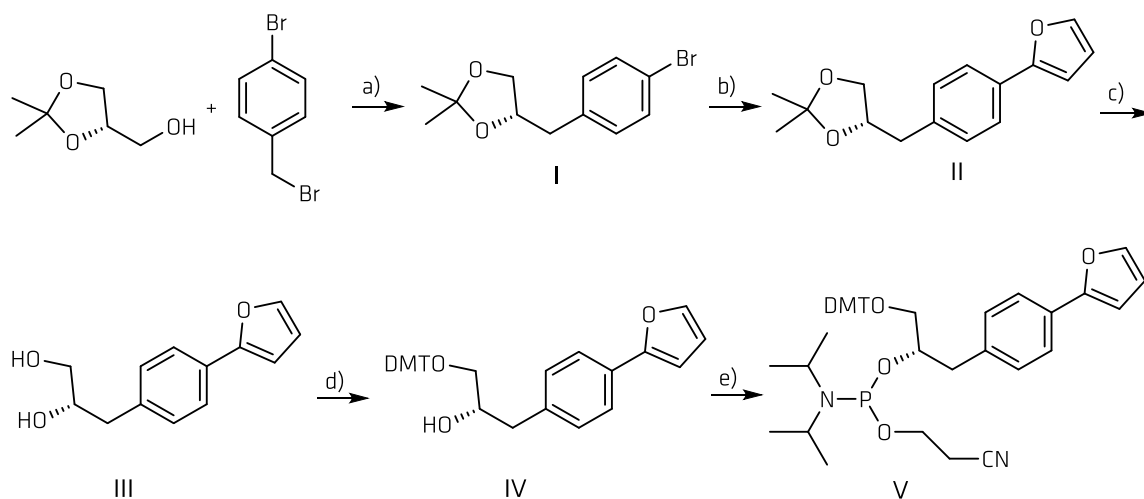
**Figure 24.** Furan-modified building blocks.

<sup>92</sup> a) K. Stevens, D. D. Claeys, S. Catak, S. Figaroli, M. Hocek, J. M. Tromp, S. Schürch, V. Van Speybroeck and A. Madder, *Chem. Eur. J.*, **2011**, 17, 6940 – 6953; b) L. L. G. Carrette, E. Gyssels, J. Loncke and A. Madder, *Org. Biomol. Chem.*, **2014**, 12, 931-935.

<sup>93</sup> a) S. R. Rajski and R. M. Williams, *Chem. Rev.*, **1998**, 98, 2723-2795; b) M. L. Dronkert and R. Kanaar, *Mutat. Res.*, **2001**, 486, 217-247; c) D. L. Boger, J. Desharnais, K. Capps, *Angew. Chem.*, **2003**, 42, 4138-4176; d) Y. Huang and L. Li, *Transl. Cancer. Res.*, **2013**, 2, 144-154.

## Introduction

The acyclic phenyl extended nucleoside **2** can be synthesized according to a method optimized in the laboratory of Professor A. Madder.<sup>92</sup> The compounds obtained along the synthesis are shown in Scheme 7.



**Scheme 7.** Synthesis of the furan modified phosphoramidite **V**: a) KOH, toluene, T= 135°C, 24h; b) furan boronic acid, Pd(PPh<sub>3</sub>)<sub>4</sub>, Na<sub>2</sub>CO<sub>3</sub>, toluene, MeOH, T= 48°C; c) HCl (4M), THF, 2h; d) DMTrCl, pyridine, T= 0°C, 3h; e) (iPrN)<sub>2</sub>(NCCH<sub>2</sub>CH<sub>2</sub>O)P, N,N-diisopropylammoniumtetrazolide, DCM, 0°- kT, 48h.

The synthesis of the furan modified phosphoramidite **V** involves the following steps: first, SN<sub>2</sub> substitution reaction where hydroxyl group of the (S)-Solketal attacks the electrophilic 4-bromobenzyl bromide to form compound **I**. Suzuki-Miyaura cross-coupling of the aromatic bromide **I** with 2-furan boronic acid and catalyzed by palladium triphenyl phosphine (Pd(PPh<sub>3</sub>)<sub>4</sub>) generates **II**. After, hydrogen chloride completes the deprotection of the diol skeleton **III**. By addition of DMTrCl as a limiting reagent in the next step, selective protection of the primary alcohol is guaranteed because ditritylation is avoided. Subsequent protection of the primary alcohol results in the formation of the dimethoxytritylated protected nucleoside **IV**. 2-Cyanoethyl-diisopropylphosphoramidite in the presence of diisopropylammoniumtetrazolide as an activating species is used in the phosphorylation reaction to obtain the building block **V** ready for incorporation into the desired oligonucleotide sequences.

To open up the pathway to biological applications, a more biocompatible oxidation method based on the use of singlet oxygen for ICL formation was developed inspired by the studies of singlet oxygen-mediated furan oxidation in the aqueous solution shown in Figure 25.<sup>94</sup> Comparison of the cross-linking yields triggered by singlet oxygen upon red light irradiation in the presence of methylene blue (MB), and NBS, showed that for all furan-modified nucleosides building blocks except 2, NBS oxidation led to higher crosslink yields.<sup>95</sup>

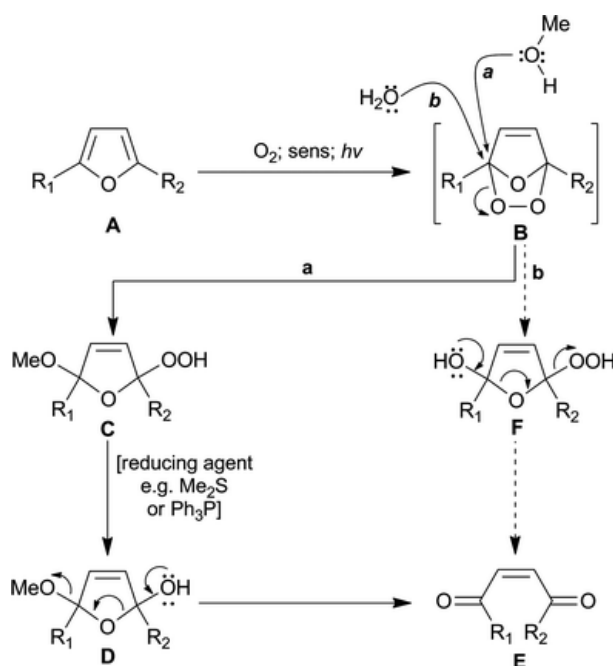


**Figure 25.** Oxidation of furan by the traditional path **a** versus the singlet oxygen mediated path **b**. Reproduced with copyright permission from RSC.

Other photosensitizers (PS), e.g. phthalocyanines that show high absorption and produce singlet oxygen in good quantum yields<sup>96</sup> were also proposed as PSs for DNA cross-linking.

Mechanism of  $^1\text{O}_2$  generation through electron or charge transfer from the excited state of a photosensitizer to the molecular oxygen ( $\text{O}_2$ ) present in the media is shown in Figure 26.<sup>97</sup> Herein, the PS is first excited from the ground singlet state to the excited singlet state by absorption of a photon upon irradiation with light. The PS can relax to the

<sup>94</sup> D. Noutsias, I. Alexopoulou, T. Montagnon, G. Vassilikogiannakis, *Green. Chem.*, **2012**, 14, 601-604.

<sup>95</sup> M. Op de Beeck and A. Madder, *J. Am. Chem. Soc.*, **2012**, 134, 10737-10740.

<sup>96</sup> C. M. Allen, W. M. Sharman and J. E. Van Lier, *J. Porphyr. Phthalocya.*, **2001**, 5, 161-169.

<sup>97</sup> T. Dai, B. B. Fuchs, J. J. Coleman, R. A. Prates, C. Astrakas, T. G. St. Denis, M. S. Ribeiro, E. Mylonakis, M. R. Hamblin, G. P. Tegos, *Front. Microbiol.*, **2012**, 3, 120.

## Introduction

longer lived triplet state, microseconds compared to the nanoseconds of the excited singlet state, and can interact with molecular oxygen in two pathways, type 1, which leads to the formation of reactive oxygen species (ROS) and type 2, which leads to the formation of singlet oxygen.

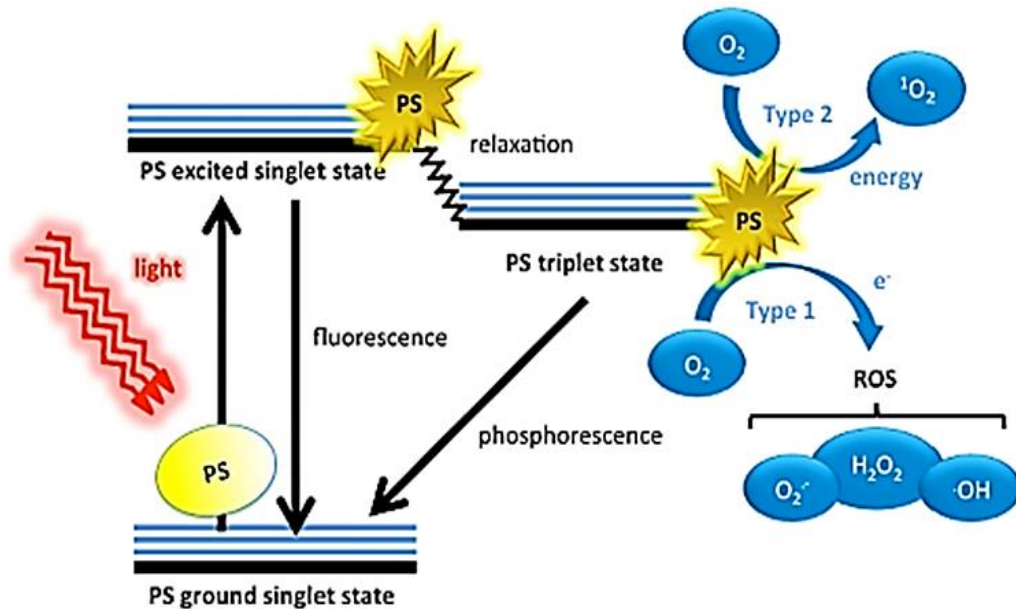


**Figure 26.** Schematic illustration of singlet oxygen generation including the Jablonski diagram to describe the states of the photosensitizer molecule (PS). Credits to the authors of Reference 97.



## **2. Objectives**

---



## 2.1 Phthalocyanine-fullerene dyads

Considering the above-mentioned examples, the objective of this work is to synthesize four novel covalently-linked Pc-C<sub>60</sub> conjugates **6-9** with better self-organization ability (Figure 27). To achieve this goal, we will employ peripherally non-substituted ZnPcs to maximize the  $\pi$ - $\pi$  stacking interactions between planar conjugated poliaromatic species, and, in the same time, to avoid the presence of regioisomeric products which are obtained when monosubstituted phthalonitriles are used as precursors in the Pc synthesis. Worth notable, the preparation and further synthetic modification of non-substituted Pcs represents a non-trivial task due to their poor solubility, and, thus, has been scarcely explored in the literature, being represented by carboxy-<sup>98</sup> and amido-<sup>99</sup> monosubstituted ZnPcs as the only examples. In this work, we will establish a straightforward route for the preparation of mono-substituted asymmetric ZnPc suitable for its easy purification and further incorporation in Pc-C<sub>60</sub> dyads.

In their turn, for the preparation of these covalent conjugates two main functionalization strategies will be used, the 1,3-dipolar cycloaddition reaction between Pc moieties bearing an azomethyne ylide function and C<sub>60</sub> (Prato reaction,<sup>100</sup> dyads **6-7**) or the cyclopropanation reaction (Bingel-Hirsch reaction,<sup>101</sup> dyads **8-9**). Moreover, the distance between ZnPcs and C<sub>60</sub> fullerene will be modulated as a function of the molecular spacer connecting both species. Its variable flexibility will additionally assist in possible improvement of supramolecular packing of the dyads. In order to see if these Pc-C<sub>60</sub> conjugates will be able to give rise to ordered structures being deposited on surfaces, AFM, STM and TEM studies will be performed. Their electron transfer reactivity will be investigated to estimate the potential applicability of the hybrids for the energy conversion schemes.

---

<sup>98</sup> Chen, J.; Chen, N.; Huang, J.; Wang, J.; Huang, M., *Inorg. Chem. Commun.* **2006**, 9, 313.

<sup>99</sup> Li, L.; Luo, Z.; Chen, Z.; Chen, J.; Zhou, Sh.; Xu, P.; Hu, P.; Wang, J.; Chen, N.; Huang, J., *Bioconjugate Chem.*, **2012**, 23, 2168.

<sup>100</sup> M. Maggini, G. Scorrano, M. Prato, *J. Am. Chem. Soc.*, **1993**, 115, 9798-9799.

<sup>101</sup> C. Bingel, *Eur. J. Inorg. Chem.*, **1993**, 126, 8, 1957-1959.

## Objectives

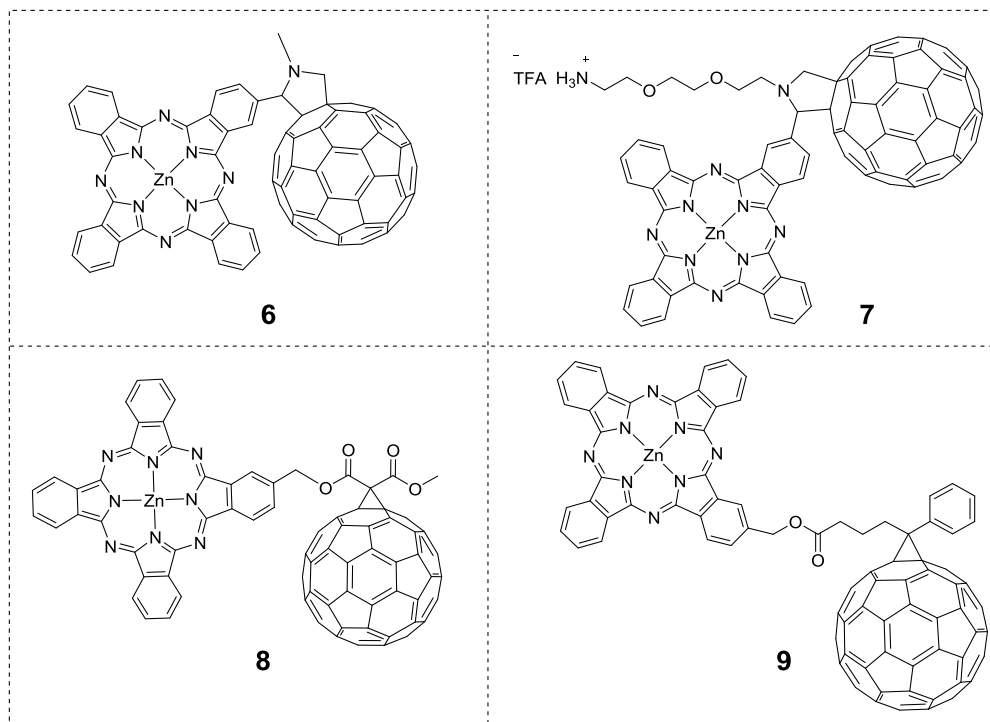


**Figure 27.** Molecular structures of ZnPc-based C<sub>60</sub> conjugates.

## 2.2 DNA interstrand cross-linking on surface

The main objective of this work was to establish a method for ICL on surface (using methylene blue and TT1 phthalocyanine as photosensitizers) towards a DDI based platform which possesses a considerable enhancement of its DNA duplex stability. This new platform, formed by furan-modified DNA oligonucleotides should be used to address an antibody previously conjugated with the short DNA (approx. 10mer) target that is required. Then, the ICL methodology would be implemented in a multiplex addressable immunoarray for the detection of three cardiac biomarkers (CRP; h-FABP; TI).

Three platforms were going to be used to perform the experiment: Enzyme-linked Immunosorbent Assay (ELISA), SPR and microarrays. Proof-of-principle of the ICL on surface will be demonstrated by SPR measurements on a Biacore system using complementary oligonucleotide pairs for hybridization and cross-linking and an FITC/anti-FITC probe as a model system, in order to generate strong signal. In addition to the SPR measurements, the aim of the ELISA experiments was to know the conditions for ICL formation and to confirm the high efficiency of the principle.

A first objective was to know the minimum length of the immobilized DNA duplex that will ensure hybridization stability. The next objective was to conjugate the antibody with these possible minimum lengths to find the optimal length of the ODN target that should be used to address in an efficient way the antibody-DNA conjugate. Since the future application would be a multiplex addressable immunoarray, the third objective is to select three DNA sequences very specific with no cross-reactivity between them.

Towards the development of a multiplex for cardiac markers, studies of cross-reactivity between the different components of the immunoassay would be performed by SPR and microarray experiments, as well as studies of stability of the system using ELISA in order to see the availability to implement the ICL method within the multiplex assay).



## **3. Materials and Methods**

---





## 3.1 Phthalocyanine-fullerene dyads

### 3.1.1 Chemicals and instrumentation

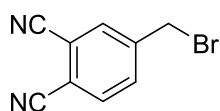
Chemicals were purchased from Aldrich Chemical Co. and Alfa Aesar Chemicals and used as received without further purification. Solvents were dried in according with standard procedures. Reactions were monitored by thin-layer chromatography (TLC) on silica gel (F<sub>254</sub> E. Merck). Column chromatography was carried out on silica gel Merck-60 (230-400 mesh, 60 Å) as a solid support. UV-vis spectra were recorded on Jasco V-660 spectrophotometer. MALDI-TOF MS spectra were obtained by an Applied Biosystem 4700 instrument equipped with a Nd:YAG laser operating at 335 nm. <sup>1</sup>H NMR and <sup>13</sup>C NMR spectra were obtained on a Bruker AC-300 spectrometer. TEM and high-resolution transmission electron microscopy (HRTEM) images were recorded with a Philips CM 300 UT. For the AFM investigations, a Digital Instrument (Veeco) Nanoscope IIIa (Tapping Mode) with Veeco RTESP5 Tips was used. In the case of the UHV-STM experiments with dyads **18** and **20**, these experiments were carried out in an ultra-high vacuum chamber (base pressure of 10<sup>-10</sup> mbar). Dyads molecules were subjected to thermal sublimation onto clean glass surface, which was held at room temperature (temperature of deposition was raised slowly from room temperature to 620 K, until first traces of deposited compound of green color could be observed). Thin liquid chromatography experiments showed the deposited compounds to be different from initial dyads, confirming thermal decomposition occurred during sublimation. STM measurements were not performed.

**Femtosecond transient absorption** measurements were carried out with a CPA-2101 femtosecond laser (Clark MXR). The excitation wavelength was generated with an NOPA (Clark MXR). **Nanosecond transient absorption laser photolysis** measurements were performed with the output from the third harmonic (355 nm) of a Nd/YAG laser (Brilliant B, Quantel). The optical detection is based on a pulsed (pulser MSP 05 – Müller Elektronik-Optik) Xenon lamp (XBO 450, Osram), a monochromator (Spectra Pro 2300i, Acton Research), a R928 photomultiplier tube (Hamamatsu Photonics), and a 1-GHz digital oscilloscope (WavePro7100, LeCroy).

### 3.1.2 Synthesis of dyad precursors

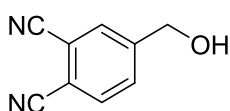
#### 4-(Bromomethyl)phthalonitrile **24**

4-Methylphthalonitrile (2 g, 14.06 mmol), NBS (2.8 g, 15.5 mmol) and AIBN (254.5 mg, 1.55 mmol) were introduced to a round bottom flask and the mixture purged with argon. Degassed  $\text{CCl}_4$  (100 mL) was added and the reaction mixture refluxed under argon atmosphere while illuminating with a 200 Watt tungsten lamp during 6 hours until the disappearance of the starting material. The reaction mixture was then let to cool down to room temperature and filtered in order to remove the succinimide. The filtrate was finally evaporated affording a residue consisting of mono-, di-, and tribromination products at the benzylic position (in an approximate 1/2/1 ratio by  $^1\text{H}$  NMR). This mixture was dissolved in dry THF (7 mL), cooled down to 0 °C and diethyl phosphite (0.7 mL) and DIPEA (0.8 mL) added dropwise. The solution was then stirred for 30 minutes at 0 °C and then at room temperature for 4 hours while monitoring the progress of the reaction by TLC and  $^1\text{H}$  NMR until the complete disappearance of the di- and tribrominated products. After this time, the solvent was evaporated, the residue obtained dissolved in  $\text{CHCl}_3$  (30 mL) and washed with an aqueous HCl 0.1M solution (30 mL), then with a saturated solution of  $\text{NaHCO}_3$  (60 mL), and finally with brine (30 mL). The organic phase was then dried over  $\text{Na}_2\text{SO}_4$ , filtered and the resulting solution reduced to dryness affording a brown solid which was purified by column chromatography ( $\text{SiO}_2$ , hexane/ethyl acetate 4/1) affording 4-(bromomethyl) phthalonitrile **24** as a yellow solid. Yield: 2.3 g, 87%.  $^1\text{H}$  NMR (300 MHz,  $\text{CDCl}_3$ ):  $\delta$  7.84 (s, 1H,  $^4J_{\text{H-H}} = 1.7$  Hz, H3), 7.80 (d, 1H,  $^3J_{\text{H-H}} = 8.1$  Hz, H6), 7.75 (dd, 1H,  $^4J_{\text{H-H}} = 1.7$  Hz,  $^3J_{\text{H-H}} = 8.1$  Hz, H5), 4.48 ppm (s, 2H,  $\text{CH}_2$ );  $^{13}\text{C}$  NMR (75 MHz,  $\text{CDCl}_3$ ): d =144.0 (C5), 134.0 (C4), 133.9 (C6), 133.7 (C3), 116.4 (C1), 115.4 (C2), 115.1 (CN), 115.0 (CN), 29.8 ppm ( $\text{ArCH}_2\text{Br}$ ).

**24**

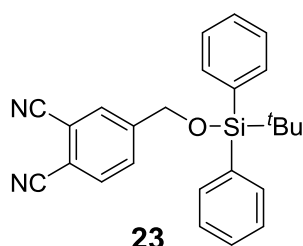
## 4-(Hydroxymethyl)phthalonitrile **25**

4-(Bromomethyl)phthalonitrile **24** (4 g, 18.1 mmol) was added to a suspension of calcium carbonate (7.24 g, 72.3 mmol) in dioxane/water (1:1.5, 200 mL) and the mixture stirred at reflux for 48 h. The reaction mixture was then filtered in order to remove the CaCO<sub>3</sub>, and the filtrate washed with Et<sub>2</sub>O (3 x 250 mL). The combined organic layers were then dried over Na<sub>2</sub>SO<sub>4</sub> and the filtrate concentrated under reduced pressure obtaining a yellow oil that solidified upon standing. Finally, the compound was purified by column chromatography (SiO<sub>2</sub>, DCM/AcOEt 2/1) affording hydroxymethylphthalonitrile **25** as a white solid. Yield: 2.81 g, 98% yield. <sup>1</sup>H NMR (300 MHz, CDCl<sub>3</sub>): δ 7.85 (s, 1H, H3), 7.81-7.71 (d broad, 2H, H5, H6), 4.86 (d, 2H, CH<sub>2</sub>), 2.07 (t broad, 1H, OH); <sup>13</sup>C NMR (75 MHz, CDCl<sub>3</sub>): d = 147.4 (C4), 133.6 (C5), 131.1 (C3), 130.7 (C6), 116.1 (CN), 115.4 (CN), 114.4 (C1), 114.3 (C2), 63.1 ppm (CH<sub>2</sub>OH).

**25**

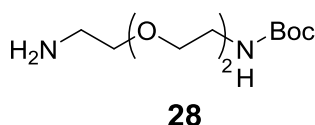
## Synthesis of TBDPS-protected, hydroxymethylphthalonitrile **23**

4-Hydroxymethylphthalonitrile **25** (100 mg, 0.63 mmol) was silylated by reaction with TBDPS chloride (0.24 mL, 0.94 mmol) in imidazole (85.8 mg, 1.26 mmol) and DMF (0.4 mL). The reaction mixture was washed with a water/DCM mixture and the isolated organic layer dried over Na<sub>2</sub>SO<sub>4</sub> and filtered. The filtrate was then reduced in volume and purified by column chromatography (SiO<sub>2</sub>, hexane/AcOEt 4/0.7) affording TBDPS-protected hydroxyphthalonitrile **23**. Yield: 170 mg, 68% yield. <sup>1</sup>H NMR (300 MHz, DMSO-*d*<sub>6</sub>) δ 7.78-7.74 (m, 2H, CH<sub>phthalonitrile</sub>), 7.68-7.61 (m, 5H, CH<sub>phthalonitrile</sub> + CH<sub>phenyl</sub>), 7.50-7.35 (m, 6H, CH<sub>phenyl</sub>), 4.81 (s, 2H, CH<sub>2</sub>), 1.12 ppm (s, 9 H); <sup>13</sup>C NMR (75 MHz, CDCl<sub>3</sub>): □ = 147.7 (C4), 135.6 (C10), 133.6 (C6), 132.5 (C5), 130.9 (C13), 130.4 (C12), 130.3 (C14), 128.2 (C11, C13, C15), 116.1 (CN), 115.6 (C2), 114.3 (C1), 64.3 (CH<sub>2</sub>OH), 26.9 (C(CH<sub>3</sub>)<sub>3</sub>), 19.4 (C(CH<sub>3</sub>)<sub>3</sub>).

**23**

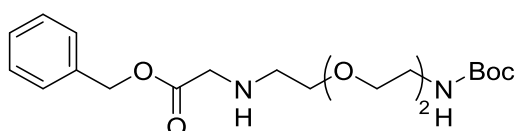
### Synthesis of {2-[2-(2-amino-ethoxy)-ethoxy]-ethyl}-carbamic acid *tert*-butyl ester **28**

To a solution of 2,2'-(ethylene-dioxy)bis(ethylamine) (5,18 g, 68 mmol) in anhydrous 1,4-dioxane (80 ml), a solution of Boc<sub>2</sub>O (5.45 ml, 23.7 mmol) in 1,4-dioxane (30 ml) was added dropwise over a period of 3 hours and the reaction mixture stirred overnight at room temperature. Once finished, the reaction solvent was removed under reduced pressure and the residue obtained dissolved in DCM (40 ml) and washed with water (3 × 100 ml). The organic layer was then dried over Na<sub>2</sub>SO<sub>4</sub>, filtered and the filtrate evaporated to dryness and purified by flash chromatography in DCM/MeOH 8/2. Yield: 3.29 g, 56%. <sup>1</sup>H NMR (300 MHz, CDCl<sub>3</sub>): δ 5.13 (s, 1H, NH), 3.62 (s, 4H, OCH<sub>2</sub>CH<sub>2</sub>O), 3.54 (m, 4H, OCH<sub>2</sub>), 3.31 (m, 2H, NH<sub>2</sub>CH<sub>2</sub>), 2.89 (t, 2H, <sup>3</sup>J<sub>H-H</sub> = 6 Hz, NHCH<sub>2</sub>), 1.89 (s, 2H, NH<sub>2</sub>), 1.44 (s, 9H, CH<sub>3</sub>).



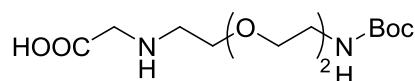
### Synthesis of {2-[2-(2-benzyloxycarbonylamino-ethoxy)-ethoxy]-ethyl}-carbamic acid *tert*-butyl ester **29**

To a solution of **28** (1.13 g, 4.55 mmol) in 1,4-dioxane (30 ml) cooled to 0 °C, a solution of benzylbromoacetate (0.24 ml, 1.53 mmol) in 1,4-dioxane (15 ml) was added dropwise over a period of 1.5 hours. The reaction mixture was then gently warmed up to room temperature and stirred for 3 hours. After this time, the solvent was removed under reduced pressure and the residue obtained dissolved in DCM (40 ml) and washed with water (3×100 ml). The organic layer was then dried over Na<sub>2</sub>SO<sub>4</sub>, filtered and the filtrate evaporated to dryness. Compound **29** was finally purified by flash chromatography in CHCl<sub>3</sub>/MeOH 2/1.5. Yield: 0.93 g, 51%. <sup>1</sup>H NMR (300 MHz, CDCl<sub>3</sub>): δ 7.35 (s, 5H, CH<sub>Ar</sub>), 5.17 (s, 2H, CH<sub>2</sub>Ph), 3.60 (s, 6H, OCH<sub>2</sub>), 3.52 (m, 2H, OCH<sub>2</sub>), 3.50 (s, 2H, NHCH<sub>2</sub>CO), 3.31 (m, 2H, CH<sub>2</sub>NHCH<sub>2</sub>CO), 2.82 (t, 2H, <sup>3</sup>J<sub>H-H</sub> = 6 Hz, CONHCH<sub>2</sub>), 1.72 (s, 1H, NHCH<sub>2</sub>CO), 1.43 (s, 9H, CH<sub>3</sub>).



## Synthesis of {2-[2-(2-*tert*-butoxycarbonylamino-ethoxy)-ethoxy]-ethylamino}-acetic acid **27**

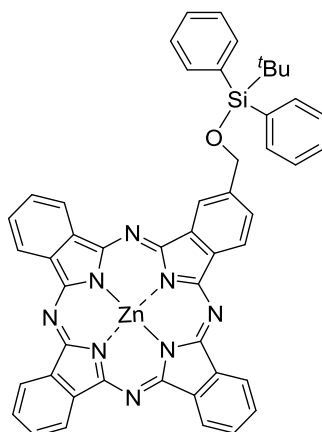
To a solution of **29** (0.2 g, 0.5 mmol) in methanol (10 ml), 20 mg of Pd/C (10%) were added and H<sub>2</sub> bubbled, and the reaction mixture stirred for 5 hours at room temperature. The solution was then filtered through a celite pad and the solvent was evaporated under reduced pressure obtaining the desired compound pure. Yield: 0.15 g, 97%. <sup>1</sup>H NMR (300 MHz, CDCl<sub>3</sub>): δ 5.56 (s, 1H, NH), 3.83 (m broad, 2H, OCH<sub>2</sub>), 3.65-3.55 (m broad, 8H, OCH<sub>2</sub>), 3.48 (s, 2H, NHCH<sub>2</sub>CO), 3.35 (d broad, 2H, OCH<sub>2</sub>), 1.43 (s, 9H, CH<sub>3</sub>).



**27**

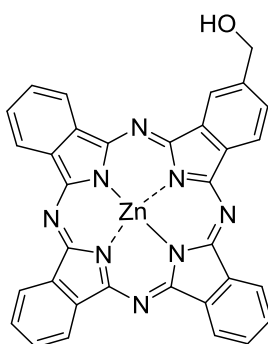
## Synthesis of TBDPS-protected hydroxymethylPc **26**

A solution of TBDPS-protected phthalonitrile **23** (3.2 g, 25 mmol) and unsubstituted phthalonitrile (3.20 g, 25 mmol) were refluxed in DMAE (30 mL) in the presence of DBU (0.75 mL, 5mmol), and then Zn(OAc)<sub>2</sub> (2.29 g, 12.5 mmol) added. The reaction was stirred overnight at reflux and then cooled to room temperature. To the resulting solution, 100 mL of H<sub>2</sub>O/MeOH (4/1) were added affording a blue precipitate that was collected by filtration and dried under vacuum. The TBDPS-substituted ZnPcs were easily extracted from the crude mixture in Soxhlett apparatus refluxing in acetone overnight. The non-substituted ZnPc was discharged, being insoluble in acetone. The mono-substituted TBDPS-ZnPc was isolated from the mixture by column chromatography (SiO<sub>2</sub>, hexane/toluene/EtOAc 2/2/0.05). The product obtained was triturated in methanol obtaining Pc **26** as blue powder. Yield: 410 mg, 10%. <sup>1</sup>H NMR (300 MHz, DMSO-*d*<sub>6</sub>) δ 9.20-8.71 (m, 8H, PcH), 8.20-8.05 (m, 6H, PcH), 8.01-7.82 (m, 5H, PcH + CH<sub>Ar</sub>), 7.65-7.50 (m, 6H, Ar), 5.35 (s, 2H, CH<sub>2</sub>), 1.30 ppm (s, 9H, CH<sub>3</sub>); UV/Vis (toluene/pyridine = 2mL/10μL, [C] = 2.94 × 10<sup>-6</sup> M): λ<sub>max</sub> = 673, 647, 606, 347 nm; MALDI-TOF MS (DCTB) (positive mode): 844,2-851.2 m/z (isotopic pattern) [M]<sup>+</sup>.

**26**

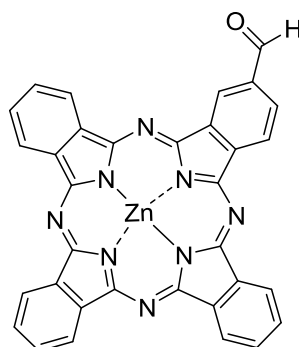
### Synthesis of hydroxymethylPc 21

A mixture of TBAF (2 mL) and glacial acetic acid (AcOH) (114.5  $\mu$ L) was added dropwise at room temperature to a solution of TBDPS-protected Pc **26** (50 mg, 0,06 mmol) in dry THF (10 mL) under stirring. The reaction was stirred for 30 min, reduced to dryness and the resulting crude purified by column chromatography (toluene/THF 2:0.05) obtaining Pc **21** as a blue solid. Yield: 35.9 mg, 98%.  $^1\text{H NMR}$  (300 MHz,  $\text{DMSO-}d_6$ ),  $\delta$  9.28-9.03 (m, 8H, Pch), 8.28-8.01 (m, 7H, Pch), 5.72 (t, 1H,  $^3J_{\text{H-H}} = 6$  Hz, OH), 5.13 (d, 2H,  $^3J_{\text{H-H}} = 6$  Hz,  $\text{CH}_2$ ); UV/Vis (THF,  $[\text{C}] = 3.472 \times 10^{-6}$  M):  $\lambda_{\text{max}} = 667, 641, 602, 342$  nm; MALDI-TOF MS (dithranol) (positive mode): 606.2-614.2 m/z (isotopic pattern)  $[\text{M}]^+$ .

**21**

## Synthesis of aldehyde-substituted Pc 22

DMSO (2 mL) was added at room temperature, under stirring, to a mixture of hydroxymethylPc **21** (45 mg, 0.074 mmol) and IBX (41.45 mg, 0.148 mmol). The reaction was stirred for 30 min and then diluted with THF (40 mL), and the resulting solution washed with a NaHCO<sub>3</sub> solution (40 mL) and a brine solution (2 × 40 mL). The organic layer was then dried over MgSO<sub>4</sub>, filtered and the filtrate evaporated obtaining a crude material which was purified by column chromatography (toluene/THF 4/1). Yield: 39.1 g, 87%. <sup>1</sup>H NMR (300 MHz, DMSO-*d*<sub>6</sub>), δ 10.47 (s, 1H, CHO), 9.20-8.88 (m, 8H, PcH), 8.39-8.21 (m, 7H, PcH); UV/Vis (THF, [C] = 4.651 × 10<sup>-6</sup> M): λ<sub>max</sub> = 681, 628, 348 nm; MALDI-TOF MS (dithranol) (positive mode): 604.2-612.2 m/z (isotopic pattern) [M]<sup>+</sup>.

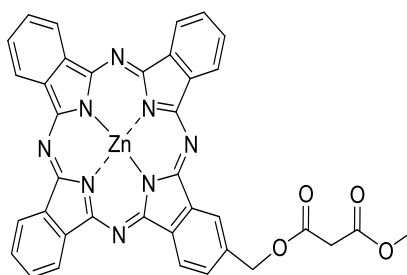


**22**

## Synthesis of malonyl-substituted Pc 31

A solution of methyl malonyl chloride (13.46 mg, 0.0986 mmol) in dry THF (1 mL) was added dropwise at 0 °C to a solution of Pc **21** (30 mg, 0.0493 mmol) in pyridine/dry THF (3 μL/5 mL). The reaction was stirred at room temperature under argon atmosphere for 15 min, and the formation of a fine precipitate observed. Afterwards, THF (100 mL) was added to the reaction mixture, and the resulting solution washed with a saturated solution of NH<sub>4</sub>Cl (2 × 50 mL) and brine (100 mL). The organic layer was then dried over MgSO<sub>4</sub>, filtered and the filtrate evaporated to dryness. The resulting material was purified by column chromatography (toluene/THF 2/0.2). Yield: 30 mg, 87%. <sup>1</sup>H NMR (300 MHz, DMSO-*d*<sub>6</sub>), δ 9.42-9.08 (m, 8H, PcH), 8.30-8.05 (m, 7H, PcH), 5.78 (s, 2H, CH<sub>2</sub>O), 3.85 (s, 2H, O<sub>2</sub>CCH<sub>2</sub>CO<sub>2</sub>), 3.81 ppm (s, 3H, OCH<sub>3</sub>); UV/Vis (THF, [C] = 3.338 × 10<sup>-6</sup> M): λ<sub>max</sub> = 667, 637, 602, 349 nm; MALDI-TOF (DCTB) (positive mode): 706.2-713.2 m/z (isotopic pattern) [M]<sup>+</sup>.

## Material and Methods



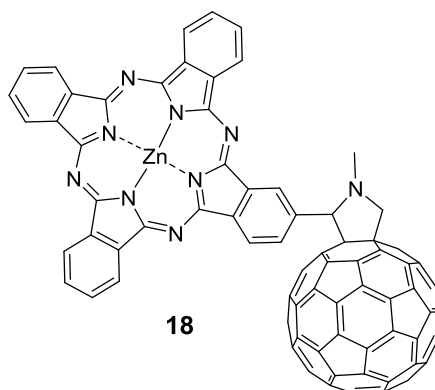
**31**



### 3.1.3 Synthesis of Zn(II)Pc-C<sub>60</sub> fullerene dyads

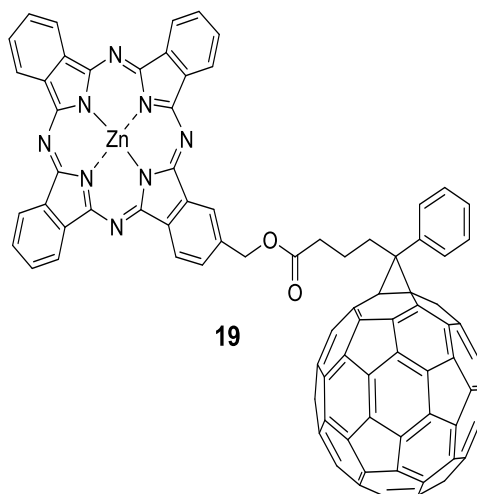
#### Synthesis of Zn(II)Pc-C<sub>60</sub> fullerene dyad 18

A mixture of aldehyde-substituted Pc **22** (15 mg, 0.0025 mmol), C<sub>60</sub> (45.04 mg, 0.0625 mmol), and sarcosine (7.79 mg, 0.0875 mmol) in dry *o*-DCB:DMF (30/5 mL) was refluxed under argon for 1h. The crude reaction was diluted with THF (25 mL), and washed with brine (3 × 100 mL). The organic layer was dried over MgSO<sub>4</sub>, filtered and the filtrate evaporated obtaining a crude material which was purified by column chromatography (toluene/THF 2:0.05). Finally, the product obtained was triturated using MeOH. Yield: 20.6 mg, 60%. <sup>1</sup>H NMR (300 MHz, CS<sub>2</sub>/THF-*d*<sub>8</sub> (1/1)), δ 9.47-9.33(m, 8H, PcH), 8.15-8.02 (m, 7H, PcH), 5.70 (s, 1H, CH pyrrolidine), 5.30 (d, 1H, CHH pyrrolidine, <sup>2</sup>J<sub>H-H</sub> = 12 Hz), 4.59 (d, 1H, CHH, <sup>2</sup>J<sub>H-H</sub> = 12 Hz), 1.29 (s, 3H, CH<sub>3</sub>); UV/Vis (toluene, [C] = 7.097 × 10<sup>-6</sup> M): λ<sub>max</sub> = 676, 609, 338 nm; MALDI-TOF (DCTB) (positive mode): 1351.1-1359.1 m/z (isotopic pattern) [M]<sup>+</sup>, 631.0-637.0 m/z (isotopic pattern) [M-C<sub>60</sub>]<sup>+</sup>.



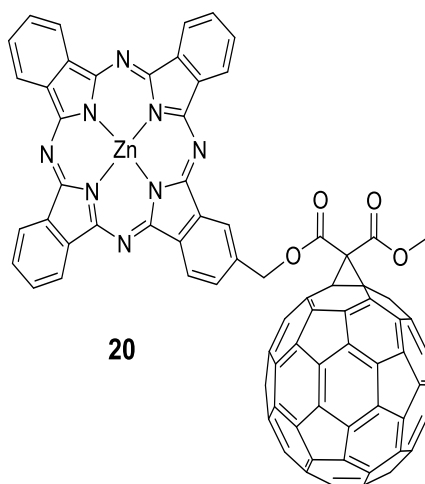
## Synthesis of Zn(II)Pc-C<sub>60</sub> fullerene dyad 19

A mixture of hydroxymethyl-substituted Pc **21** (30 mg, 0.033 mmol), PCBA (20.34 mg, 0.033 mmol), 1-ethyl-3-(3-dimethylaminopropyl)-carbodiimide (EDCI) (20.49 mg, 0.132 mmol) in *o*-DCB/pyridine (2/0.15 mL) was stirred overnight at room temperature under argon atmosphere. After this time, the solution was directly columned (toluene/THF 2:0.07) obtaining Pc **19** as a dark green product. Yield: 84 mg, 86%. <sup>1</sup>H NMR (300 MHz, CS<sub>2</sub>/THF-*d*<sub>8</sub> 1/1), δ 9.41-9.22 (m, 8H, PcH), 8.20-8.07 (m, 7H, PcH), 7.95 (d, 2H, CH<sub>2</sub>O), 7.52 (t, 2H, CH<sub>aryl</sub>), 4.45 (t, 1H, CH<sub>aryl</sub>), 7.20-7.05 (m, 2H, CH<sub>aryl</sub>), 5.68 (s, CH<sub>2</sub>), 3.00 (m, CH<sub>2</sub>), 2.75 (m, CH<sub>2</sub>); UV/Vis (toluene, [C] = 4.626 × 10<sup>-6</sup> M): λ<sub>max</sub> = 673, 612, 335 nm; MALDI-TOF (DCTB) (positive mode): 1484.2-1492.2 m/z (isotopic pattern [M]<sup>+</sup>).



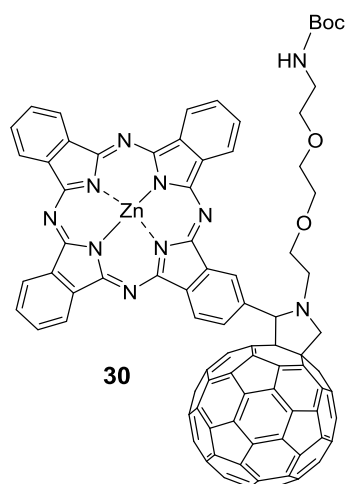
## Synthesis of Zn(II)Pc-C<sub>60</sub> fullerene dyad 20

A solution of malonyl-substituted Pc **31** (20 mg, 0.028 mmol) in dry DMF (2ml) was added to a solution containing C<sub>60</sub> (40.35 mg, 0.056 mmol) and CBr<sub>4</sub> (33.81 mg, 0.102 mmol) in dry toluene (15 mL) previously sonicated for 15 min. The solution was stirred for 10 minutes and then DBU (25.88 mg, 0.17 mmol) added. The mixture was stirred at room temperature, in the darkness, for 48h. After this time the solvent was removed and the resulting solid purified by column chromatography (toluene/THF 2/0.03). The compound obtained was finally triturated in MeOH obtaining a dark green solid. Yield: 30 mg, 70%. <sup>1</sup>H NMR (300 MHz, CS<sub>2</sub>/THF-*d*<sub>8</sub> 1/1), δ 9.38-9.12 (m, 8H, PcH), 8.19-8.05 (m, 7H, PcH), 6.08 (s, 2H, CH<sub>2</sub>O), 4.20 ppm (s, 3H, OCH<sub>3</sub>); UV/Vis (toluene, [C] = 1.122 × 10<sup>-5</sup> M): λ<sub>max</sub> = 673, 611, 332 nm; MALDI-TOF (DCTB) (positive mode): 1424.1-1432.1 m/z (isotopic pattern) [M]<sup>+</sup>.



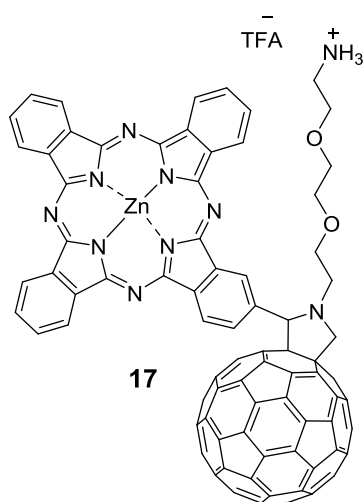
### Synthesis of Zn(II)Pc-C<sub>60</sub> fullerene dyad **30**

A mixture of Pc aldehyde **22** (15 mg, 0.03 mmol), C<sub>60</sub> fullerene (45 mg, 0.06 mmol), and aminoacid **27** (20.8 mg, 0.09 mmol) were added to a round bottom flask under argon and a mixture of dry *o*-DCB/DMF (30/5 mL) added. The reaction mixture was stirred at 120 °C overnight and then the solvent removed obtaining a crude product that was purified by column chromatography (toluene/THF 2/0.1) obtaining dyad **30** as a blue solid. Yield: 20.1 g, 58%. <sup>1</sup>H NMR (300 MHz, THF-*d*<sub>8</sub>), δ 9.51-9.01 (m, 8H, PcH), 8.15-7.95 (m, 7H, PcH), 6.00 (s broad, 2H, CH<sub>pyrrolidine</sub> + NHC=O), 5.61 (d, 1H, <sup>2</sup>J<sub>H-H</sub> = 12 Hz, CH<sub>2</sub> pyrrolidine), 4.65 (d, 1H, <sup>2</sup>J<sub>H-H</sub> = 12 Hz, CH<sub>2</sub>pyrrolidine), 4.05 (t, 2H, CH<sub>2</sub>), 3.91 (t, 2H, CH<sub>2</sub>), 3.81 (t, 2H, CH<sub>2</sub>), 3.31 (t, 2H, CH<sub>2</sub>), 3.25 (m, 4H, CH<sub>2</sub>), 1.41 (s, 9H, CCH<sub>3</sub>); UV/Vis (toluene, [C] = 6.061 × 10<sup>-6</sup> M): λ<sub>max</sub> = 675, 608, 335 nm; MALDI-TOF MS (dithranol) (positive mode): 1568.3-1576.3 m/z (isotopic pattern) [M]<sup>+</sup>, 848.3-853.2 m/z (isotopic pattern) [M-C<sub>60</sub>]<sup>+</sup>, 3136.1-3147.5 m/z (isotopic pattern) [2M]<sup>+</sup>.



## Synthesis of Zn(II)Pc-C<sub>60</sub> fullerene **17**

To a suspension of **30** (9 mg, 0.0057 mmol) in CH<sub>2</sub>Cl<sub>2</sub> (2 mL), 1 mL of TFA was added and the solution stirred overnight. The salt was precipitated from the reaction mixture, filtered, and the solid washed with hexane and dried under vacuum obtaining fullerene salt **17** as a blue solid. Yield: 8.8 g, 98%. UV/Vis (THF, [C] = 5.481 × 10<sup>-6</sup> M): λ<sub>max</sub> = 671, 606, 346 nm; MALDI-TOF (DCTB) (positive mode): 1468.3-1476.3 m/z (isotopic pattern) [M-H-TFA]<sup>+</sup>, 748.2-755.2 m/z (isotopic pattern) [M-H-TFA-C<sub>60</sub>]<sup>+</sup>.



## 3.1.4 Experimental techniques

### Atomic Force Microscopy (AFM)

AFM is primarily used to examine surface morphology and to measure interaction forces between the tip and sample (*i.e.* force spectroscopy).<sup>102</sup> In a contrast to STM, AFM is able to measure any solid material without the condition of surface conductivity. Atomic force microscope consists of a sharp nanometer-sized probe attached to a springboard or V-shaped cantilever which is positioned over a surface deposited sample as shown in Figure 28a. Piezoelectric scanners control subnanometer movements in the  $x$ ,  $y$ , and  $z$  dimensions, then images are compiled line-by-line as the sample is raster scanned. Additionally, a laser beam is focused on the back-tip of the cantilever to measure changes in cantilever deflection. Forces between the sample and the probe caused either by sample topography changes or the forces between the sample and the probe result in cantilever deflection. These changes in deflection are converted to force using Hooke's law, which allows for the quantification of forces on the pN scale and the employment of force spectroscopy.

The cantilever is excited into oscillations near the resonant frequency of the cantilever. The instrument then maintains constant oscillation amplitudes and taps along the surface. Any displacement in the  $z$  dimension is a measure of the height variation on the sample. Force spectroscopy is used to examine specific interaction forces between the tip and sample at forces as low as 10 pN. A typical measurement is diagramed in Figure 8b, where the tip starts far from the surface (1), comes in contact with the surface (2), applies a specific loading force to the sample (3), and then the process is repeated in reverse wherein the tip retracts from the surface. When an interaction between the tip and sample occurs, step (4) is observed. At the point the tip overcomes the force holding it at the surface the tip breaks away from the sample (5), and retracts to its original position (1). Therefore, this process enables force spectroscopy and allows for the direct quantification of interaction strength between the probe and the sample.

---

<sup>102</sup> G. Haugstad, Atomic Force Microscopy: Understanding Basic Modes and Advanced Applications, John Wiley & Sons, Inc., 2012.

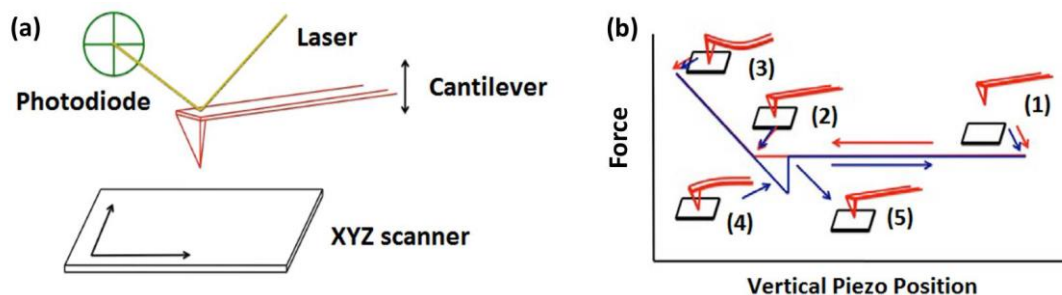


**Figure 28.** Schematic representation of a) AFM components, b) AFM force-distance measurement.

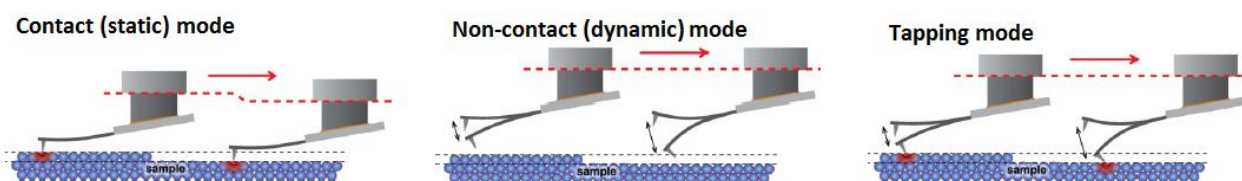


**Figure 29.** Different operational modes of AFM measurement.

The AFM techniques have been developed for twenty years during which three main operation modes have been established (Figure 29). In a *Contact (Static) mode*, the cantilever is in full contact with the surface. The repulsive interaction forces (topography) is determined by measuring the static deflection of the cantilever. This technique is capable of detecting the topography of atomic scale resolution. Due to the fact that strong repulsive interaction force and friction take place between tip and surface, this technique is harsh to the sample. In a *Non-contact (Dynamic) mode*, the cantilever is usually driven close to its resonant frequency, with vibration amplitudes less than 100 nm. The cantilever driver usually is a piezo-electric element, but many experiments have been performed with electrostatic, magnetic, thermo-optic or acoustical coupling drivers. The driver is mounted to the head of the microscope and the chip with the cantilever is mounted on top of the driver. The interaction force is modulating the vibration frequency, amplitude and phase. From the oscillator modulation can be distinguished surface topography. *Tapping mode* represents a combination of the static and dynamic modes. It allows minimizing friction between tip and measured surface which is strongly present in the contact mode. The oscillating tip only touches the measured surface at maximum deflection of the cantilever towards measured surface. In this moment, there is direct mechanical contact with strong repulsive interaction forces between tip and surface. Due to the dynamic operation of the cantilever and very short contact time this technique can be considered as non-contact. We will employ the tapping mode technique in our study.

## Transmission Electron Microscopy (TEM)

TEM is a form of microscopy in which a beam of electrons transmits through an extremely thin specimen and interacts with the specimen when passing through it.<sup>103</sup> The formation of images in a TEM can be explained by an optical electron beam diagram (Figure 30). Electrons are usually generated in an electron microscope by a thermionic emission from tungsten, in the same manner as a light bulb, or alternatively by field electron emission. The electrons are then accelerated by an electric potential (measured in volts) and focused by electrostatic and electromagnetic lenses onto the sample. The transmitted beam contains information about electron density, phase and periodicity. This beam is used to form an image.

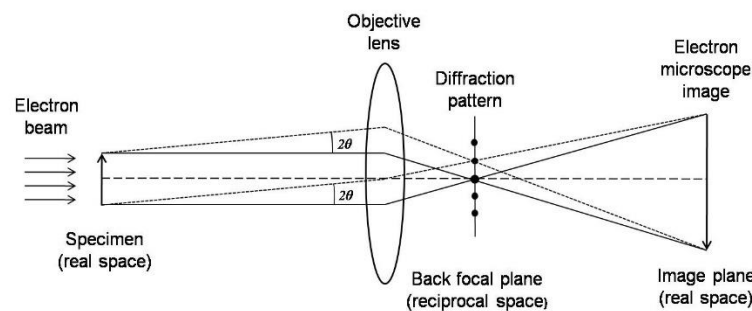


**Figure 30.** The optical electron beam diagram of TEM.

Transmission electron microscopes provide images with resolutions which are several thousand times higher than the highest resolution in a visible-light microscope because of the smaller de Broglie wavelength of electrons. Nevertheless, the magnification provided in a TEM image is in contrast to the absorption of the electrons in the material, which is primarily due to the thickness or composition of the material. For a sample to be transparent to electrons, the sample must be thin enough to transmit sufficient electrons such that enough intensity falls on the screen to give an image. A detrimental effect of ionizing radiation is that it can damage the specimen, particularly polymers and most organics. Some aspects of beam damage turn worse at higher voltages.

<sup>103</sup> C. B. Carter, *Transmission Electron Microscopy: A Textbook for Material Science*, 2nd Ed., Springer, New York, 2009.

## Transient absorption spectroscopy

The absorption of UV and/or visible light by an organic molecule causes the promotion of an electron from an initially occupied, low energy orbital to a higher energy, previously unoccupied orbital (Figure 31).<sup>104</sup> When such event happens, an excited state of the molecule is generated. Following light absorption, several processes contribute to the relaxation of the molecule and its return to the ground state. These processes can be either *radiative* (a photon is emitted during the transition) or *non-radiative* (the loss of energy is emitted as heat- infrared radiation- instead of UV-visible light).

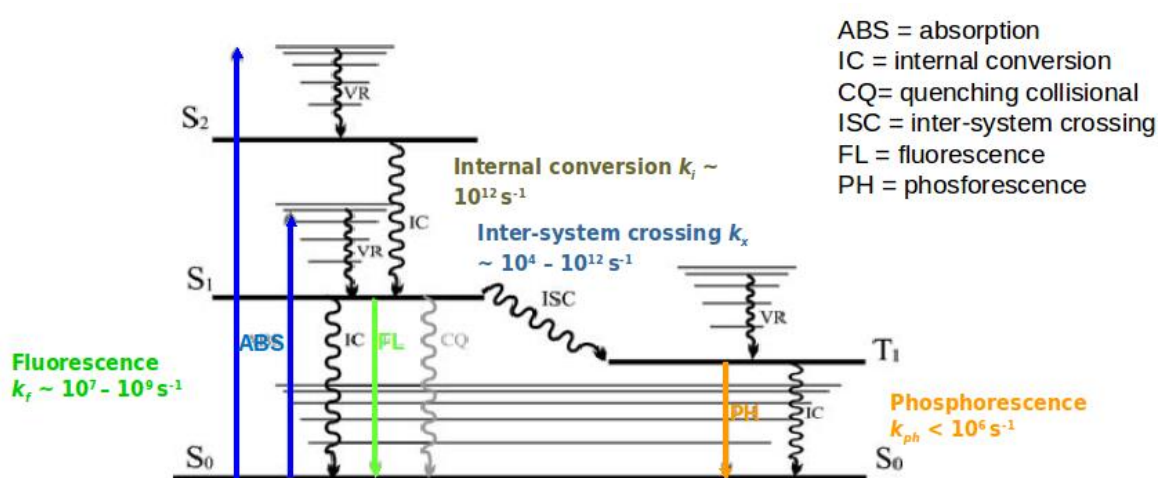


**Figure 31.** Yablonski diagram showing processes taking place in a chromophore upon photoexcitation.

After light absorption, and in the presence of other molecules in solution, chromophores can also undergo transformations like energy transfer, PET or other chemical reactions. These events are among the fastest events in nature. They occur on the time scales ranging from femtoseconds to nanoseconds. The development of ultrafast laser systems has enabled investigation of these events in real time. *Femtosecond transient absorption spectroscopy*, also referred to as *femtosecond pump-probe spectroscopy*, is one of the most common tools to investigate ultrafast photochemical reactions. In particular, this technique allows the observation of light-induced intra- and intermolecular processes on the time scale of the motion of atoms and electrons and, thus, provides one of

<sup>104</sup> a) Modern Molecular Photochemistry, N. J. Turro, University Science Books, 1991; b) Principles of Fluorescence Spectroscopy, 3rd Ed., J. R. Lackowicz, Springer Science, 2006.



the most effective methods for studying the behavior of transient species like radicals, ions and excited states.<sup>105</sup>

The principle of *transient absorption spectroscopy* is shown in Figure 32a. Here, the absorbance at a particular wavelength or range of wavelengths of a sample is measured as a function of time after excitation by a flash of light. In a typical experiment, both the light for excitation – pump – and the light for measuring the absorbance – probe – are generated by a pulsed laser. In each measurement, the absorbance of the probe pulse by the sample is recorded twice, the second time after a certain delay with respect to the pump pulse. Thus, in the first shot, the absorbance of the sample in the ground state is recorded. In contrast, the second time the probe pulse hits the fraction of molecules that has been promoted to an electronically excited state by means of the pump pulse. A difference absorption spectrum is then calculated. By changing the delay, a  $\Delta OD$  profile as a function of time and wavelength is obtained (Figure 32b). This profile contains information on the dynamic processes occurring in the system under study. Specifically, the analysis of the *differential absorption spectra* ( $\Delta OD$  vs wavelength) allows identification of the excited states or transient species formed upon excitation of the chromophore. On the other hand, the study of *decay profiles* ( $\Delta OD$  vs time) provides information on the kinetics of photo-physical or photochemical processes.

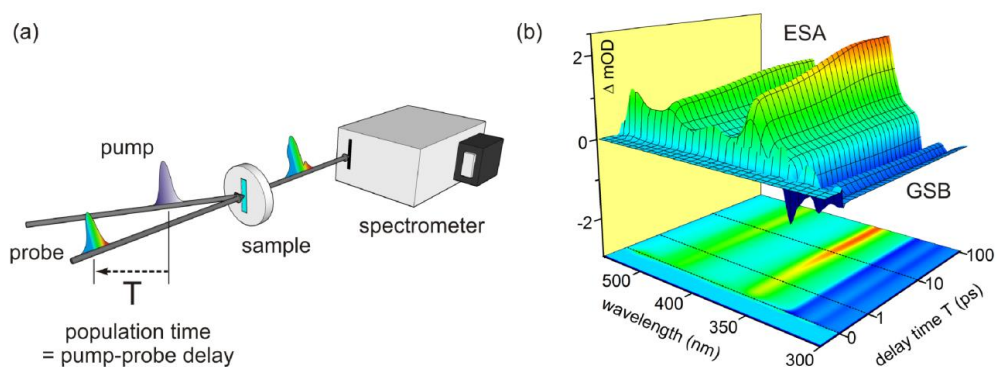


**Figure 32.** (a) Schematic representation of transient absorption (pump-probe) spectroscopy. (b) UV-light-induced changes in optical density ( $\Delta OD$ ) of pyrene showing dynamics of the  $S_1$  excited state absorption (ESA) and ground state bleaching (GSB) contribution.

<sup>105</sup> R. Berera, R. van Grondelle, J. T. M. Kennis, *Photosynth. Res.*, **2009**, *101*, 105-118.

## Material and Methods

In general, the bands observed in a transient absorption spectrum arise from three kinds of contributions:

- *Ground-state bleach*: as a fraction of molecules has been promoted to the excited state through the action of the pump pulse, population of the ground state has decreased. As a consequence, ground state absorption of the excited sample is lower than the non-excited. Hence, a negative signal in the  $\Delta OD$  spectrum is observed. This signal appears in the region of the ground state absorption (it mirrors the UV-Vis absorption band).

- *Stimulated emission*: upon population of the first excited state, stimulated emission may take place when the second probe pulse passes through the sample. This process will occur only for optically allowed transitions, and its spectral profile generally reflects the fluorescence spectrum of the chromophore. The photon thus generated is emitted in the same direction as the one of the probe pulse, and both are detected. Hence, stimulated emission produces a negative  $\Delta OD$  signal. Many chromophores present such a low Stokes shift that both ground state bleach and stimulated emission bands overlap and merge into one band.

- *Excited state absorption*: optically allowed transitions from the excited states (populated upon excitation with the pump pulse) to higher states might exist in certain wavelength regions. Absorption of the probe pulse at these regions is then observed as a positive band in the  $\Delta OD$  spectrum.

## 3.2 DNA interstrand cross-linking on surface

### 3.2.1 Chemicals and instrumentation

#### Chemicals

Methylene Blue (MB), N-hydroxysuccinimide (NHS), N-(3-dimethylaminopropyl)-N'-ethylcarbodiimide hydrochloride (EDC), and molecular biology grade buffer reagents were purchased from Sigma-Aldrich and used without further purification. The TT1 photosensitizer was prepared according to a method described previously.<sup>8</sup>

Buffers used for ELISA: PBS buffer (1 mM sodium phosphate, 0.015 M NaCl, pH 7.6), substrate buffer (220 mM potassium dihydrogen citrate, 0.5 mM sorbic acid potassium salt, pH 4.0), TMB solution (40 mM tetramethylbenzidine and 8 mM tetrabutylammonium borohydride in N,N-dimethylacetamide), substrate solution (540  $\mu$ L TMB solution and 3 mM hydrogen peroxide in 21.5 mL of substrate buffer). SPR Experiments were performed at 25 °C using PBST (0.05% (v/v) Tween™ 20) as running buffer. All buffers were filtrated using 0.2  $\mu$ m pore filters. 3,3',5,5'-Tetramethylbenzidine (TMB) and Tween™ 20 pure were from Serva.

The synthesis of the furan-modified oligonucleotides was performed as described previously.<sup>92</sup> Reagents for the synthesis of 5'-biotin furan-modified ODNs were obtained from Glen Research. The complementary 5'-FITC modified ODNs, streptavidin-coated 96-well microtiter plates and anti-FITC-HRP-monoclonal antibody (Lot P319, 0.73 mg/mL) from mouse were purchased from BioTeZ (Berlin, Germany).

Mouse monoclonal capture antibodies (FABP 10-7904: Lot 2622, 6 mg/L; Troponin I 10-T79H: Lot 2423, 5 mg/mL; CRP 10-C189B: Lot 2612, 4.5 mg/mL), human cardiac proteins (Troponin I 30-AT63: Lot A15032430, 0,621 mg/mL; FABP 30-1006, Lot A16031430, 2,2 mg/mL; CRP 30-AC05S, Lot A26031430 2,5 mg/L) and mouse monoclonal detection antibodies (FABP 10-7904: Lot 2421, 1,64 mg/mL; Troponin I 10-7967: Lot 3526, 0,52 mg/mL; CRP 10-C189A: Lot 2867, 1,49 mg/mL) were purchased from Fitzgerald Industries International (Acton, USA). N-Hydroxysuccinimide (NHS) activated glass slides were purchased from SCHOTT NEXTERION. Cy3 Maleimide Mono-Reactive dye (PA23031) was obtained from GE Healthcare Life Sciences and their conjugation protocol was followed for the synthesis of the antibody-Cy3 dye conjugate.

### **Instrumentation**

The SPR measurements were performed using a Biacore™ T200 device (T200 Sensitivity Enhanced, GE Healthcare Bio-Sciences AB, Uppsala, Sweden) and dextran-modified chips (G-COOH-sp) from Ssens (Enschede, The Netherlands).

The illuminator KL1500 LCD 150 W from Schott was used as a cold red light source for irradiation. The streptavidin-coated microtiter plates were read using a SpectraMax-Plus384 from Molecular Devices controlled by SoftMax® Pro software (v 5.2, Molecular Devices). The automatic 96-channel plate washer, ELx405 Select™ from BioTek Instruments was used to wash the plates and glass slides. The plate shaker was a Titramax 101 (Heidolph, Schwabach, Germany). An ABI 394 DNA synthesizer was used for ODN synthesis. The glass slide was scanned using an Axon GenePix 4300A reader controlled by GenePix Pro 7.1 software. The laser power and PMT were set to 60% and 400 respectively. Microarray printing was performed using a BioOdyssey Calligrapher MiniArrayer (Bio-RadLaboratories, Inc. USA).

## 3.2.2 Experimental procedures

### 3.2.2.1 Surface Plasmon Resonance

The following scheme shows the method used to detect the ICL of immobilized ODNs. As a result of the ICL formation, the short ODN should enhance its stability towards regeneration conditions using a denaturing  $\text{Na}_2\text{CO}_3$  solution. Figure 33a shows how the hybridized ODNs are efficiently separated after using  $\text{Na}_2\text{CO}_3$  for regeneration. Oxidation of the furan using  $^1\text{O}_2$  results in the formation of a rugged ICL, rendering the resulting short ODN duplex stable towards  $\text{Na}_2\text{CO}_3$  (Figure 33b). Therefore, the binding of the antibody is still possible. Sensorgrams were double-referenced using an empty flow cell or a flow cell with non-complementary DNA for subtraction of nonspecific effects and buffer injections for correction for artifacts.

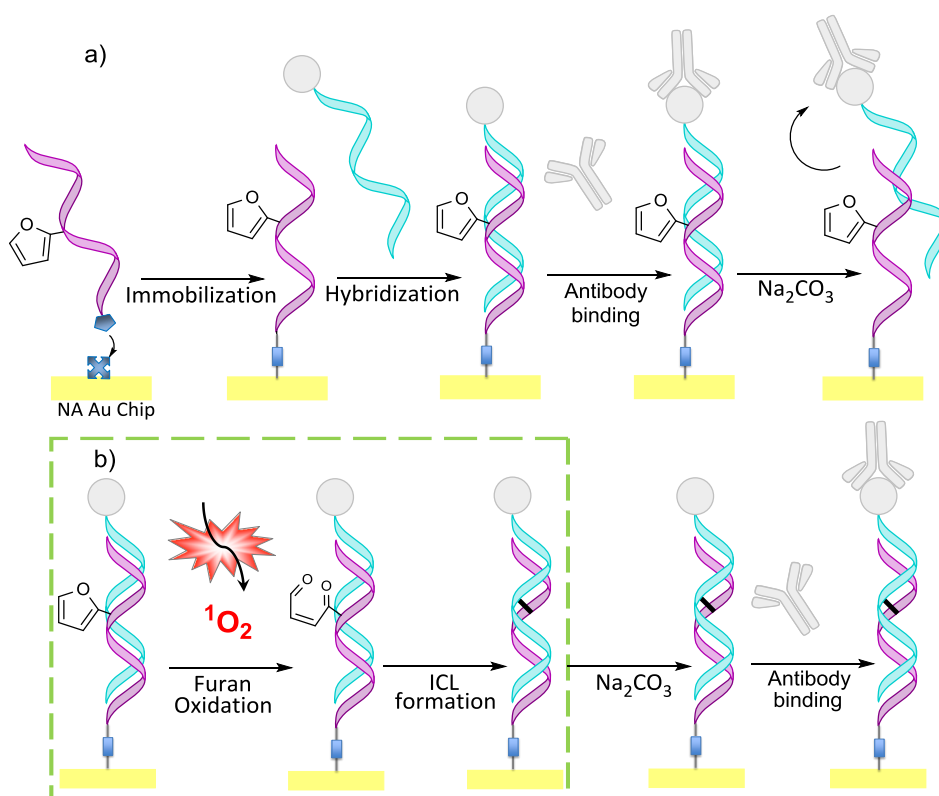


**Figure 33.** Schematic comparison between hybridized and cross-linked ODN.

## **General procedure for immobilization of biotinylated furan-modified ODNs**

The gold chip was coated with neutravidin (NA) by EDC/NHS coupling, followed by the immobilization of biotinylated ODNs. For this, the activation of the carboxylic groups was done by injecting into the Biacore™ device channel 0.4/0.1 M EDC/NHS for 3 min followed by 100 µg/mL solution of NA in 10 mM acetate buffer pH 5.5 and coupling was allowed for 13 min. Unmodified reactive sites were then blocked with 1 M ethanolamine pH 8.5 for 7 min. The respective biotinylated and furan-modified capture oligonucleotide (2 µM) in PBST pH 7.6 running buffer was then injected for 2 min. Blocking of the NA reactive sites was performed by using 10 µM biotin in running buffer for 1 min. All injections were carried out at a flow rate of 10 µL/min.

## **Hybridization procedure**

In order to obtain the association and dissociation curves of the DNA duplex, the complementary FITC-modified ODNs were allowed to hybridize to the capture ODNs by injecting different concentrations (0.01-10 µM) in running buffer for 2 min at a flow rate of 30 µL/min. Dissociation of hybridized immobilized ODNs was achieved by injecting running buffer for 10 min at a continuous flow rate of 30 µL/min.

## **Cross-linking experiments**

Before taking the chip out of the SPR instrument for the ICL experiments, the binding of 48 nM HRP-labelled anti-FITC antibody to hybridized FITC-ODN was performed, then 50 mM Na<sub>2</sub>CO<sub>3</sub> was injected for 1 min as a test for the instability of the DNA duplex. Hybridization and cross-linking were done in parallel by adding 100 µL of a mixture containing 1 µM FITC-ODN and the photosensitizer (5 µM MB or 5 µM TT1) to produce the necessary <sup>1</sup>O<sub>2</sub>. Afterwards, the chip was irradiated with red light (658 nm, 8 cm distance) for 45 min at 350 rpm at room temperature. After washing with running buffer and drying of the chip, it was again mounted into the SPR instrument, where a first regeneration was carried out by 50 mM Na<sub>2</sub>CO<sub>3</sub> for 1 min followed by the binding of 48 nM HRP-labelled anti-FITC antibody in running buffer. The immobilized ODN1 was cross-linked by incubation with 1 µM C.ODN1 in PBS pH 7.6 buffer and 5 µM MB. TT1 was initially dissolved in (DMSO due to its low water solubility; the final concentration of TT1 was 5 µM).

## Hybridization specificity experiments

Oligonucleotide sequences ODN2, 3 and 4 were immobilized using the method described before flowing 2  $\mu$ M solutions in separate flow cells and tested simultaneously for hybridization specificity. The complementary sequences C.ODN2, 3 and 4 were tested alone and in the mixture. For the hybridization, 1  $\mu$ M solutions of the C.ODNs in running buffer were injected over 2 min. Dissociation of hybridized ODNs was effected by injecting running buffer for 2 min. After each hybridization, the surface was regenerated flushing 1 min with 50 mM  $\text{Na}_2\text{CO}_3$  to prepare the chip for the next hybridization. Kinetic data were obtained using five successive injections of recombinant GFP (Green Fluorescent Protein; single-cycle kinetics). Loading of the chip was calculated considering one resonance unit (RU) corresponding to one  $\text{pg}/\text{mm}^2$  of bound biologic material.<sup>106</sup> Further data analysis of obtained sensorgrams was performed using Biacore™ T200 Evaluation Software v1.0.

---

<sup>106</sup> Karlsson, R.; Fagerstam, L.; Nilshans, H.; Persson, B., Analysis of active antibody concentration. Separation of affinity and concentration parameters. *J. Immunol. Methods*, **1993**, *166*, 75-84.

### **3.2.2.2 ELISA**

The streptavidin-covered microtiter plate was coated with 100  $\mu\text{L}$  of ODN1 (0.1  $\mu\text{M}$ ) in PBS buffer and incubated for 30 min on a plate shaker at 750 rpm. The plate was then washed with washing buffer. The immobilized ODN1 was allowed to hybridize for 45 min with 100  $\mu\text{L}$  of 0.1  $\mu\text{M}$  C.ODN1 at 350 rpm. The interstrand cross-linking reaction was carried out at a final concentration of 5  $\mu\text{M}$  MB by adding 20  $\mu\text{L}$  of an accordingly concentrated solution to each well. Afterward, the plate was irradiated with red light (658 nm; 8 cm distance) for 45 min at 350 rpm. After discarding the mixture 50 mM  $\text{Na}_2\text{CO}_3$  (150  $\mu\text{L}/\text{well}$ ) was added and the plate was shaken at 750 rpm for regeneration. The plate was washed after 10 min with washing buffer. A dilution of 1:10,000 HRP-labelled anti-FITC antibody in PBS buffer (100  $\mu\text{L}/\text{well}$ ) was incubated for 45 min at 750 rpm. After washing away unbound antibody, 100  $\mu\text{L}$  of substrate solution was added to the wells and incubated while shaking at 750 rpm. The reaction was stopped after 10 min by adding 50  $\mu\text{L}$  of 1 M sulphuric acid to each well. The optical density was measured at 450 nm using 650 nm as reference. All steps were carried out at room temperature. Experiments under dark and natural light conditions were done in parallel.

### **3.2.2.3 MALDI-TOF sample preparation procedures**

#### **DNA oligonucleotide**

To 20 mg of  $\alpha$ -cyano-4-hydroxycinnamic acid (CHCA) matrix in an Eppendorf was added 1 ml of 90:10 acetonitrile/0,1 % trifluoroacetic acid (TFA) and vortex 1 minute to dissolve (saturated solution 1, some undissolved matrix will remain). After, were mixing 345 $\mu\text{L}$  of solution 1 with 24 $\mu\text{L}$  100Mm Ammonium dihydrogen phosphate ( $\text{NH}_4\text{H}_2\text{PO}_4$ ) and 24  $\mu\text{L}$  10% TFA solution to obtain the matrix solution. Sample solution was mixed 50:50 with 0.025% TFA and centrifuged using a zeba spin column. The filtrate was then mix with matrix solution at sample to matrix ratios of 50:50. For the crystallization was: deposited 1 $\mu\text{l}$  of this final mix onto the Anchor target plate and allow to air dry.



## Antibody-oligonucleotide conjugate

To 20 mg of Sinapinic Acid (SA) matrix in an Eppendorf was added 1 ml of 70:30 water/0,1 % TFA. and vortex 1minute to dissolve. Sample solution was mixed 50:50 with water and centrifuged using a zeba spin column. 0.5- $\mu$ L of matrix stock solution was pre-spotted on the silver anchor target plate. After this spot was dried, 0.5  $\mu$ L of protein sample solution was added on top. The matrix sample crystals were allowed to form through solvent evaporation.

### 3.2.2.4 Cross-linking in solution

The product from the cross-linking in solution of ODN1-C.ODN1 using 5  $\mu$ L MB as photosensitizer was analysed by MALDI-TOF, RP-HPLC and PAGE experiments. Mass spectra were acquired using a Bruker Autoflex II MALDI mass spectrometer operated with a nitrogen laser. RP-HPLC and PAGE experiments were performed following previously published procedures.<sup>95</sup>

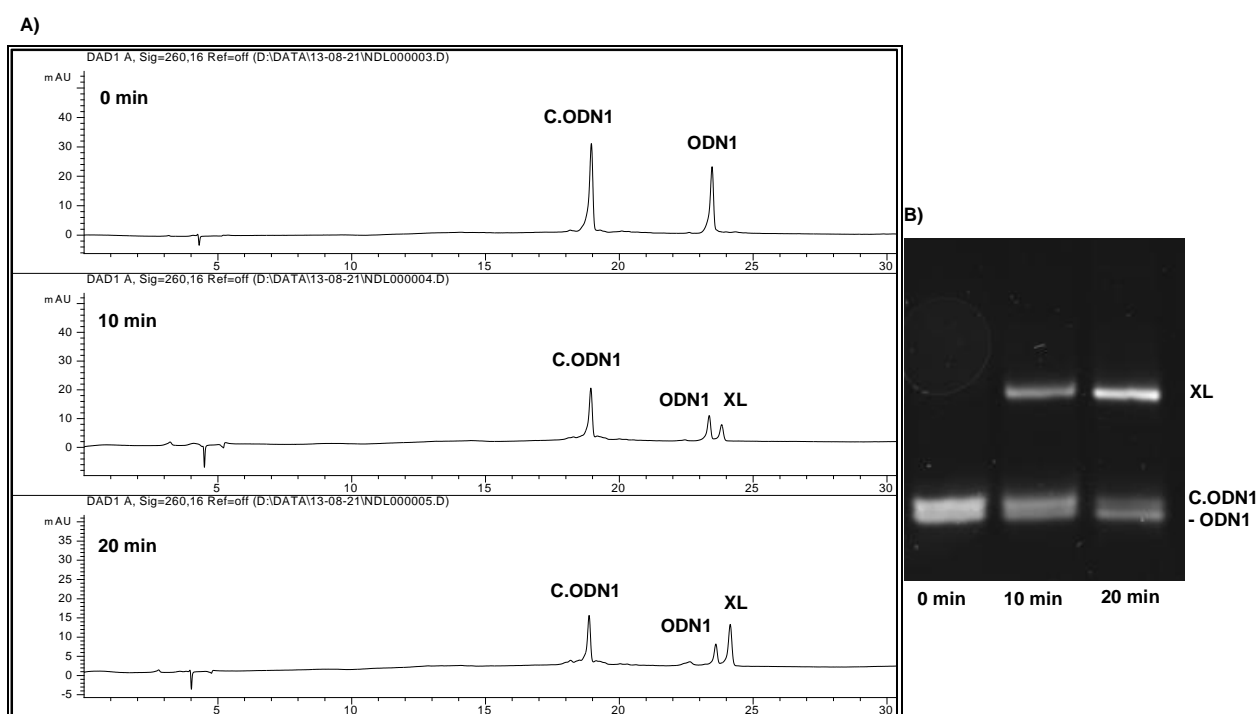


**Figure 34.** A) Reversed-phase HPLC chromatograms of the reaction mixture of furan-modified ODN1 and C.ODN1 (after annealing in a 1:1 ratio to obtain the duplex) with 5 $\mu$ M MB before reaction and after 10 and 20 minutes of irradiation. B) Denaturing PAGE results of the cross-link reaction. XL represents.

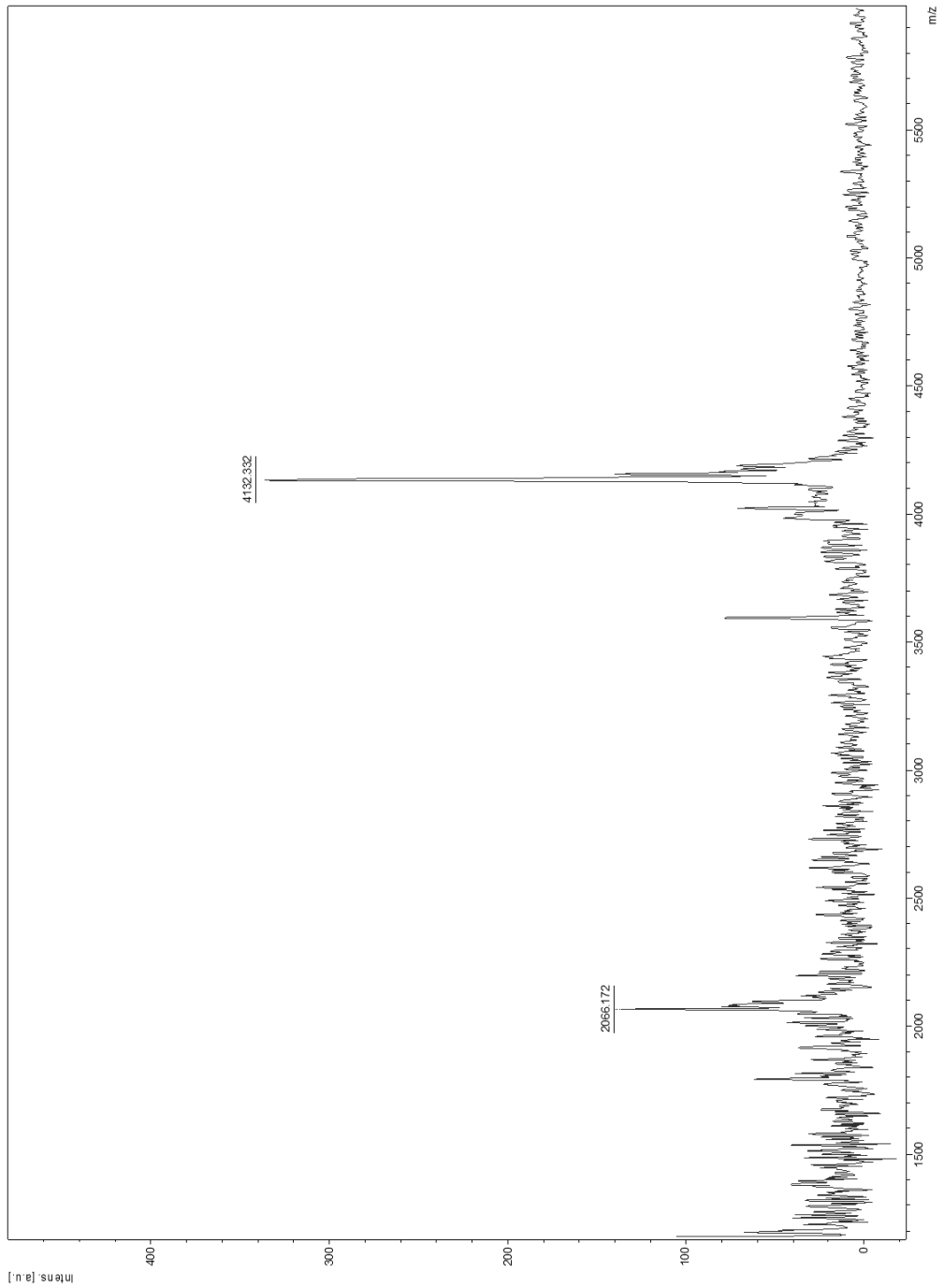


**Figure 35.** MALDI-TOF mass spectrum of the cross-linked oligonucleotide sequences ODN1-C.ODN1 in solution (calculated mass 8263.68 Da; observed mass  $[M+H^+]/2=4132.332$  and  $[M+H^+]/4=2066.172$ ).

### 3.2.3 Antibody-oligonucleotide conjugation

The conjugation of the antibody with the three oligonucleotides (10-mer, 12-mer, Poly T 12-mer (Sp 12mer)) was performed following the method describe Söderberg et al.<sup>123</sup> Compared with the native antibody, the MALDI-TOF mass spectrum of all conjugates were shifted  $\sim 4$  Da, which are corresponding to the mass of the oligonucleotide, indicating successful conjugation with the corresponding oligonucleotide.

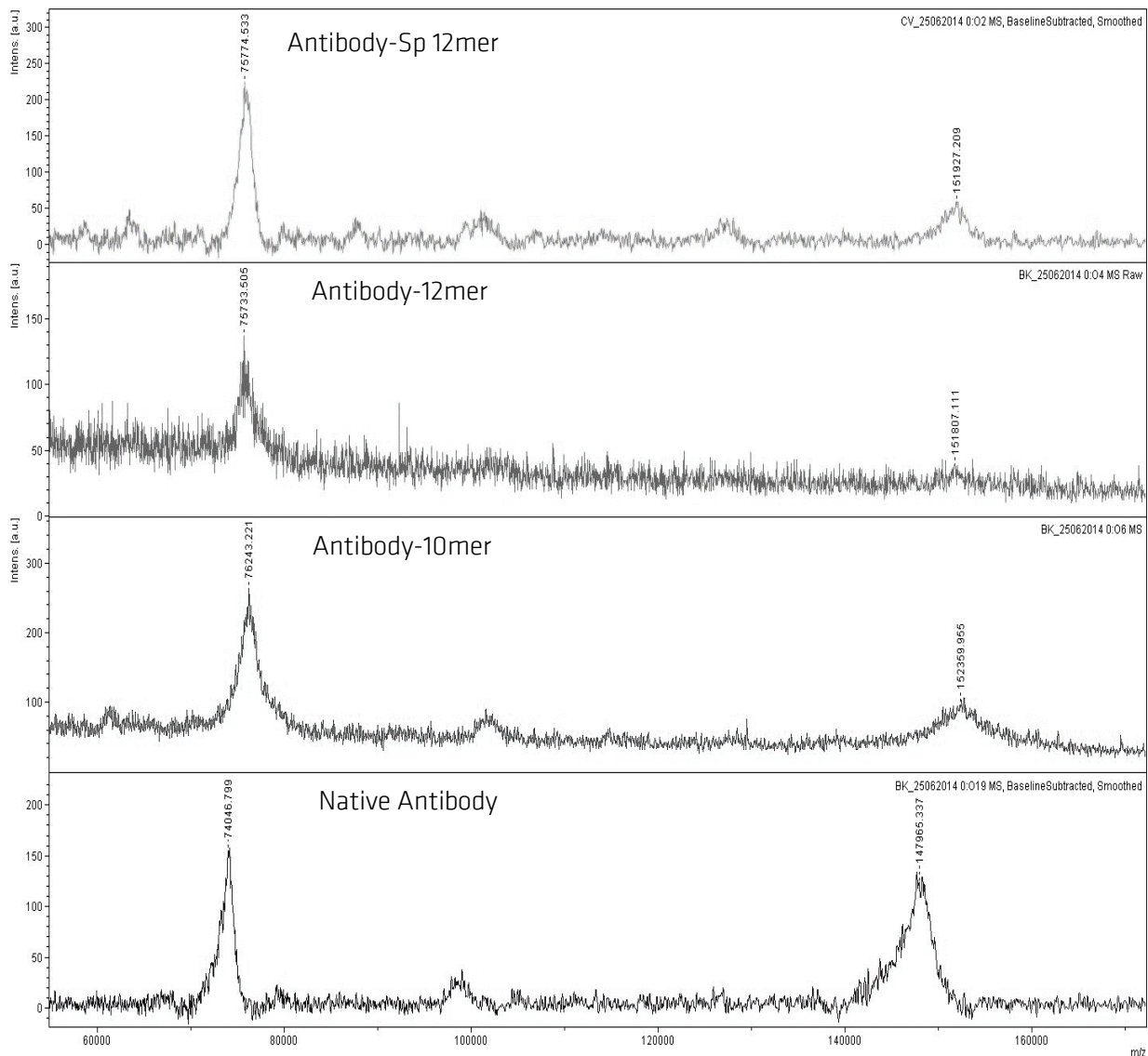


**Figure 36.** Comparison of MALDI-TOF mass spectrum of the native antibody with antibody-oligonucleotide conjugates.

### **3.2.4 Cross-reactivity experiments of the multiplex immunoassay**

#### **Surface plasmon resonance**

The capture antibody was immobilized on the gold chip by EDC/NHS coupling. For this, the activation of the carboxylic groups was done by injecting into the Biacore™ device channel 0.4/0.1 M EDC/NHS for 3 min followed by 20 µg/mL solution of the corresponding capture antibody in each flow cell, the coupling was allowed for 13 min. Unmodified reactive sites were then blocked with 1 M ethanolamine pH 8.5 for 7 min. The mixture of cardiac biomarkers (1- 500 ng/mL) was dissolved in PBST running buffer and was then injected for 2 min in all flow cells. Afterwards, 1 µg/mL of detection antibody was added in PBST buffer.

#### **Microarray**

The capture antibody was diluted to 20 µg/mL final concentration using printing buffer (150 mM PBS, pH 8.5, 5 % glycerol), spotted onto NHS glass slides in 60% humidity and incubated over night at room temperature. The slide was then washed twice with 30 mL of PBST buffer for 10 min at room temperature and dried under a stream of Argon gas. Subsequently, the slide was immersed in 30 mL of 70 mM ethanolamide in PBS for 1 h at room temperature to block the surface. Blocking and washing processes were performed with gentle shaking on a shaking plate. The slide was placed on a microarray hybridization cassette and the mixture of analytes (100 µL/well) diluted in different concentrations ranging from 1000 to 100 ng/mL in PBST solution containing 10% BSA. And then incubated for 1 h at room temperature. The slide was then washed manually with PBST solution. Finally, the slide was incubated with 1 µg/mL of detection antibody-Cy3 conjugate (100 µL/well) for 60 min at room temperature. Fluorescence intensity (mean value minus background) of each spot on the slide were expressed normalized as average and standard deviation of three replicate spots.

### 3.2.5 Experimental techniques

DNA hybridization can be detected by different techniques based on gravimetric, electrochemical, or optical detection. Two optical detection techniques, surface plasmon resonance (SPR) and an enzyme-catalyzed colorimetric assay, are going to be described.

#### Surface Plasmon Resonance (SPR)

This technique has been used frequently to develop biosensors, especially to detect DNA-DNA hybridization. SPR is an optical technique which allows the detection and quantification of molecular interactions- such as proteins, nucleic acid, peptides and small molecules - in real time, without the use of labels. One of the interactants (e.g. DNA probe) is immobilized on the sensor surface, usually composed of a 50 nm-layer of gold on a glass surface, and the other interactant is passed over the gold surface in solution by a microfluidic flow system. The opposite, glass side of the sensor stands has attached to it a prism illuminated by polarized light from a near infrared LED. The focus under the sensor is set to conditions of total internal reflection and a detector monitors the intensity of the light reflected (Figure 37).<sup>107</sup>

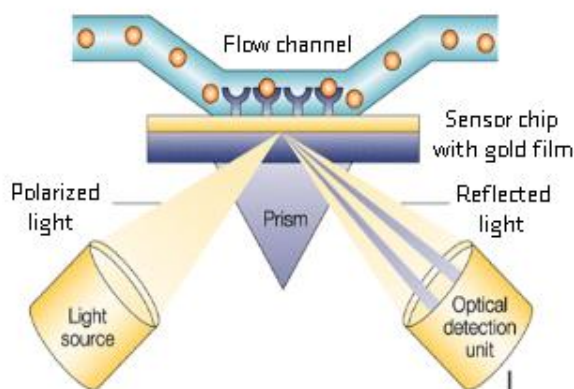


**Figure 37.** Surface Plasmon Resonance principle. Reproduced with copyrights permission from The Nature Publishing Group.

The light under conditions of total internal reflection leaks an electromagnetic wave field (evanescent) across the gold film into the sample solution. At a certain angle of incident light, the evanescent wave excites electrons in the gold producing the formation of

<sup>107</sup> M. A. Cooper, *Nat Rev Drug Discov*, **2002**, 1, 515-528.

surface plasmons (electron charge density waves) within the gold film with a drop in the intensity of the reflected light angle called SPR angle. When a change in mass occurs near the sensor chip surface (as a binding result), the angle of the light at which SPR should occur shifts which can be described as a change in refractive index near the sensor surface.

A sensorgram from an SPR experiment is shown in Figure 38. It shows responses measured in resonance units (RU) in real time. The sensorgram provides essentially two kinds of information: the rate of interaction (association, dissociation), which provides a) information on kinetic rate constants ( $k_{\text{ass}}$ ,  $k_{\text{diss}}$ ) and analyte concentration, and b) the binding level, which provides information on affinity constants. The sensorgram is a plot of response in resonance units versus time in seconds, which is presented continuously in real time. As the analyte binds to the surface, the refractive index of the medium adjacent to the sensor surface increases, which leads to an increase in the resonance signal and the association is measured. At the end of the analyte injection, the analyte solution is replaced by a system buffer, and the receptor-analyte complex is allowed to dissociate. A decrease in mass occurs due to dissociation and is measured. At equilibrium, by definition, the amount of analyte that is associating and dissociating with the receptor molecule is equal.

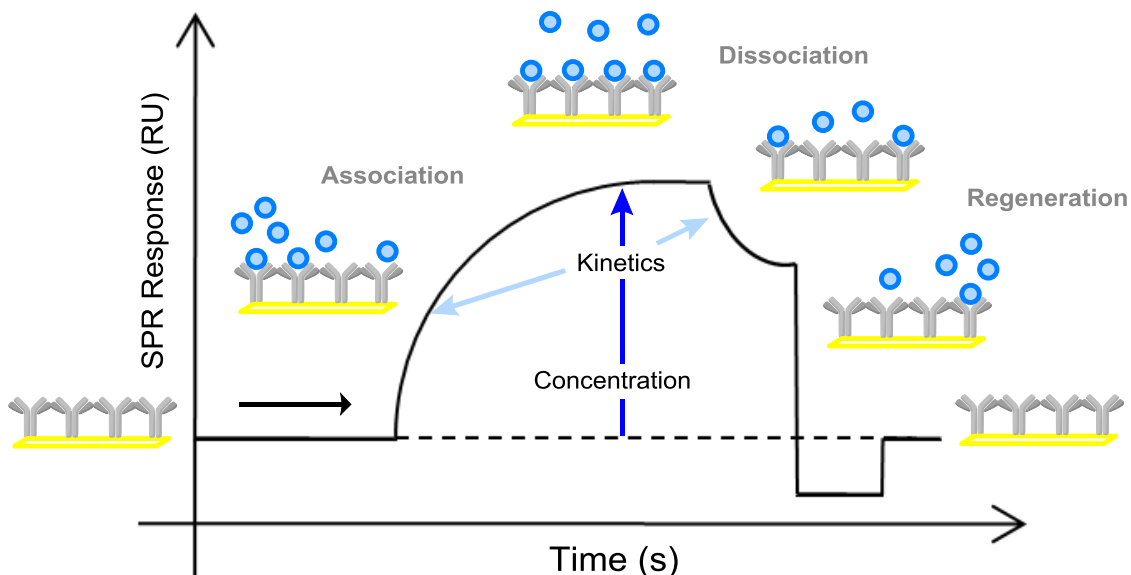


**Figure 38.** Typical phases and sensorgram of an SPR measurement.

One RU corresponds to  $0.0001^\circ$  shift of the SPR angle, or to  $1 \text{ pg/mm}^2$  of immobilized receptor molecule on the sensor surface. The response level at equilibrium is related to the concentration of an active analyte in the sample. It is possible to disturb the binding of many complexes and regenerate the free receptor on the surface by a regeneration solution (for example, with high salt concentration or low pH). The affinity of the interaction can be calculated from the ratio of the rate constants ( $k_d = k_{\text{diss}}/k_{\text{ass}}$ ) or by a linear or nonlinear fitting of the response at equilibrium at varying concentrations of analyte.

## Enzyme-catalyzed colorimetric assay

In the enzyme-catalyzed colorimetric assay used the optical density generated is proportional to the amount of analyte. This assay was performed using a 96-well microtiter plate. For a very sensitive detection of DNA hybridization, the colour-generating reaction is catalyzed by horseradish peroxidase (HRP) bound to a recognition molecule (e.g. Streptavidin) towards the hybridized biotin-labeled DNA strand.

HRP catalyzes the reaction of the peroxidase substrate 3,3',5,5'-tetramethylbenzidine (TMB) in the presence of hydrogen peroxide (Figure 39a). HRP converts the hydrogen peroxide to water, obtaining the two hydrogen atoms it needs for this from TMB, which acts as a donor molecule. So, at the same time that HRP is being reduced, TMB is oxidized. The TMB oxidation pathway by  $H_2O_2$  is described in Figure 39b.<sup>108</sup> TMB is colourless and its oxidation produces a blue colour with the maximum absorbance at 652 nm. After addition of sulfuric acid, the reaction is stopped, and the blue colour changes to yellow with maximum absorbance at 450 nm.

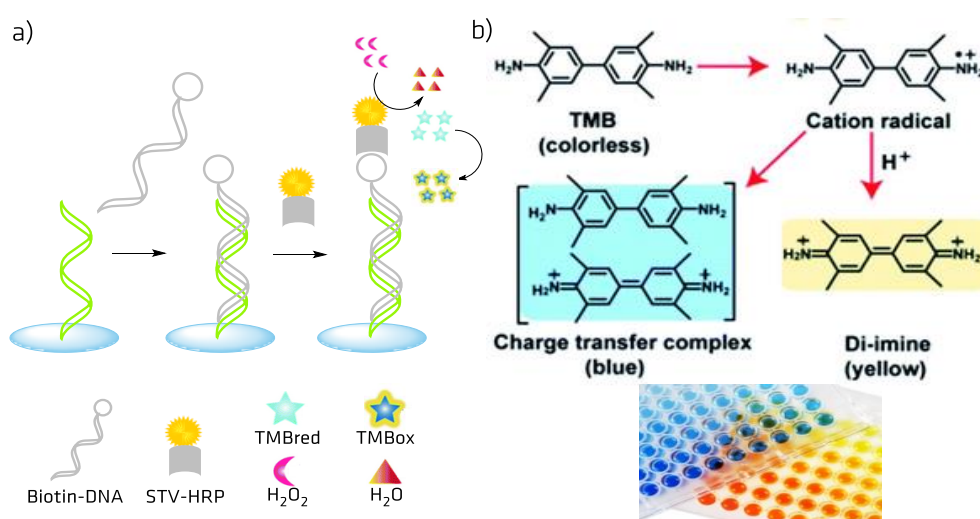


**Figure 39.** a) Schematic illustration of DNA hybridization detection via HRP-catalyzed TMB oxidation. b) Chemical structures resulting from the oxidation pathways of the TMB and the corresponding visual colour changes on microtiter plates. Adapted from Reference 76 licensed under a Creative Commons Attribution 3.0 Licence.

<sup>108</sup> Y. Lin, L. Wu, Y. Huang, J. Ren and X. Qu, *Chem. Sci.*, **2015**, 6, 1272-1276.



## Automated DNA synthesis

During the automated DNA synthesis of oligonucleotides the chain is built in the 3'-5' direction. The synthesis starts by the attachment of the first nucleoside of the desired sequence to a solid support via its 3'-hydroxyl group. The main step is the specific and sequential formation of the internucleoside 3'-5' phosphodiester bond. To ensure the coupling reactions to be selective, the 5'-hydroxyl group of the nucleoside is protected with an acid-labile dimethoxytrityl (DMTr) group. Afterwards, the 3'-hydroxyl group of the nucleoside is converted into a phosphoramidite function in order to enable coupling with the free 5'-OH of the previous nucleoside (Figure 40).<sup>66</sup>

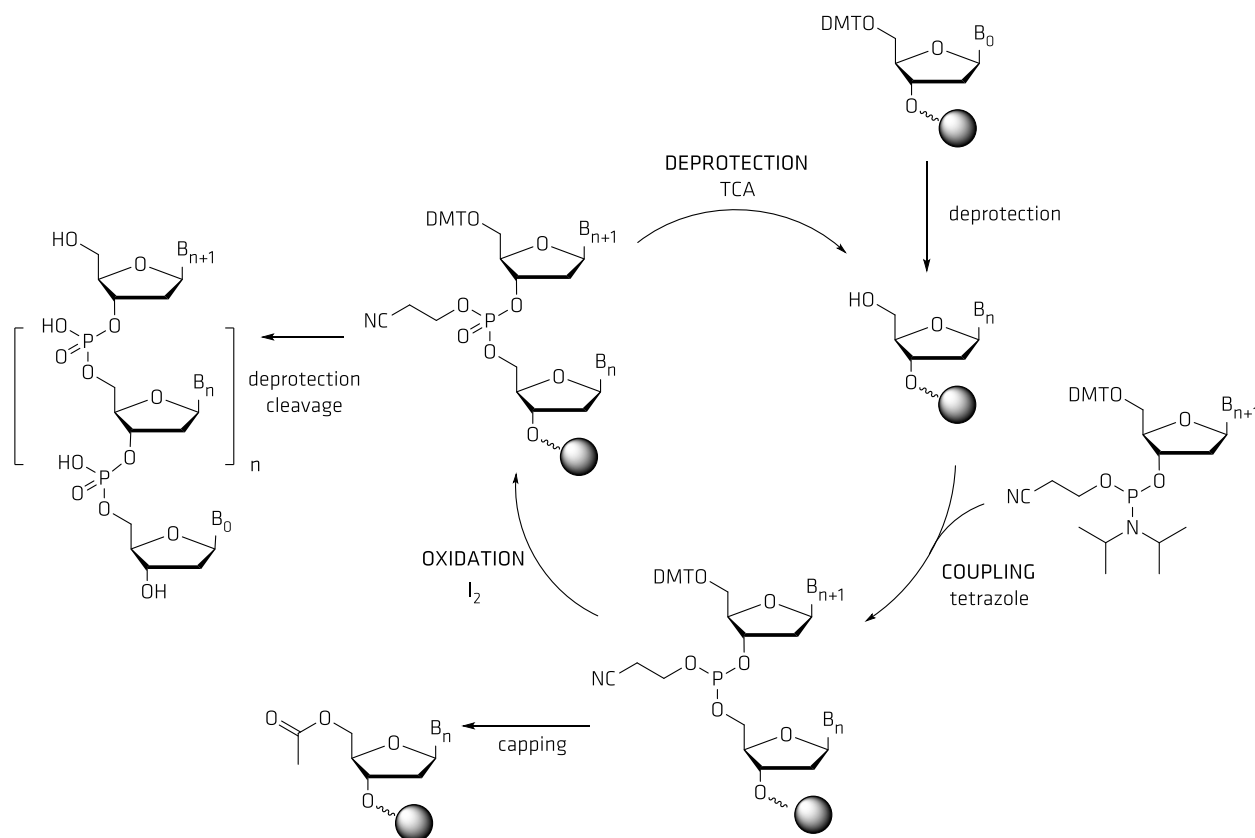


**Figure 40.** Scheme of automated DNA synthesis.

The cyclic procedure, containing a series of deprotection, coupling, capping and oxidation steps results in the formation of the desired oligonucleotide sequence. The first step in each chain elongation cycle is the deprotection of the 5'-hydroxyl nucleoside group with a solution of dichloroacetic acid in dichloromethane, after this solution is applied, the orange coloured trityl cation is released from the reaction column indicating that this step was successful. After deprotection, a new phosphoramidite can be coupled to the free 5'-hydroxyl terminal residue of the nucleic acid chain. First, the phosphoramidite is activated

## Material and Methods

with a solution of tetrazole in acetonitrile, after which the activated phosphoramidite is attached to the growing nucleic acid chain with the formation of a phosphite triester bond between the 5'-hydroxyl of the terminal nucleic acid residue and the 3'-end of the new monomer.

It is possible that a small amount of the unreacted deprotected terminal residue still remains. This would lead to the formation of the so-called deletion sequence, which is an oligonucleotide chain with a missing nucleotide. In order to avoid this deletion, a capping step is introduced into the cycle. In the capping step, the 5'-hydroxyl group of the unreacted terminal nucleoside is blocked by acetylation. In the last step, the phosphite triester is oxidized to the more stable phosphodiester bond with iodine and water in pyridine. This cycle is repeated until the desired oligonucleotide chain has been obtained. The oligonucleotide can be cleaved from the solid support by treatment with an ammonium solution and the protective groups can be removed by heating up to 55°C. The oligonucleotide can be isolated from the mixture containing also deletion sequences, cleaved protecting groups and capped oligonucleotides by several purification methods, such as, for example, ethanol precipitation, ion exchange or size-exclusion chromatography, RP-HPLC and reversed-phase cartridge purification. In the last one, the DMTr-protecting is not removed at the end of the synthesis cycle. Purification can be obtained based on the hydrophobicity of the DMTr group, which has a very high affinity for the hydrophobic column so the full-length DMTr-Oligonucleotide is retained on the column, while the other components are washed off. After cleaving of the DMTr on the cartridge (e.g. trifluoroacetic solution) it is possible to elute the oligonucleotide.

## **4.Results and Discussion**

---



## 4.1 Phthalocyanine-fullerene dyads

In this chapter, I will report on synthesis and properties of a different type of materials – polyconjugated nanocarbons – that possess interesting self-assembling properties, significantly affecting their physicochemical characteristics. Additionally, objects that will be described in present chapter are related to the renewable energy issue. Finding sustainable energy sources is a genuine challenge of modern society yet to be reached.<sup>109</sup> In this connection, screening of artificial photosynthetic systems stands out as one of the hot topics of contemporary science.<sup>110</sup>

### 4.1.1 Synthesis and characterization

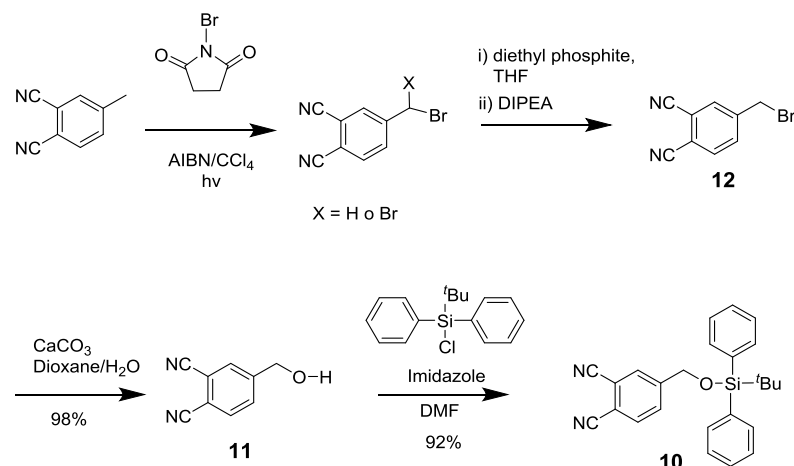
The *tert*-butyldiphenylsilane (TBDPS)-protected hydroxymethylphthalonitrile **10** is the key-compound towards the synthesis of all mono-substituted ZnPcs as it will be shown further in this section. Compound **10** was obtained according to reported procedure<sup>111</sup> in a multistep synthesis from 4-methyl phthalonitrile (Scheme 4). Thus, 4-methylphthalonitrile was subjected to the Wohl-Ziegler photoinduced bromination with *N*-bromosuccinimide (NBS) and catalytic amount of 2,2'-azobis(isobutyronitrile) (AIBN) as initiator for the selective bromination of benzylic hydrogens (Scheme 4). A mixture of mono-, di- and tribrominated compounds were obtained in a 1:2:1 ratio, respectively, as observed by TLC and <sup>1</sup>H-NMR. Treatment of this mixture with an excess of diethylphosphite and *N,N*-diisopropyl-*N*-ethylamine (DIPEA) yielded 4-(bromomethyl)phthalonitrile **12**. This latter compound was then refluxed in an aqueous solution of dioxane (dioxane/water 1/1.5) in the presence of calcium carbonate affording 4-(hydroxymethyl) phthalonitrile **11** with a yield of 98%. Finally, TBDPS-protected hydroxymethylphthalonitrile **10** was obtained in 92% yield upon silylation of phthalonitrile **11** using TBDPS chloride in DMF in the presence of imidazole.

<sup>109</sup> a) J. Twidell, T. Weir, *Renewable Energy Resources*, Routledge, **2015**, pp. 151-202; b) R. Wengenmair, T. Bührke, *Renewable energy: sustainable energy concepts for the future*, Wiley - VCH, Weinheim, **2013**, pp. 1-170.

<sup>110</sup> a) G.D. Scholes, G. R. Fleming, A. Olaya-Castro, R. van Grondelle, *Nat Chem.*, **2011**, *3*, 763-774; b) R. J Cogdell, T. H. P. Brotsudarmo, , A. T Gardiner, P. M Sanchez, L. Cronin, *Biofuels* **2010**, *1*, 861–876; c) Issue on “Artificial Photosynthesis and Solar Fuels”, *Acc. Chem. Res.*, **2009**, *42*, 1859-2029.

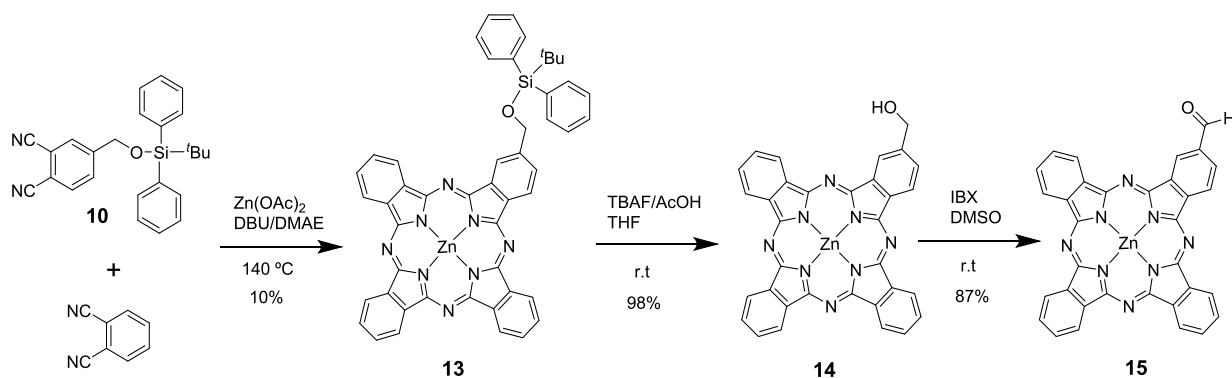
<sup>111</sup> R. F. Enes, J.-J. Cid, A. Hausmann, O. Trukhina, A. Gouloumis, P. Vázquez, J. A. S. Cavaleiro, A. C. Tomé, D. M. Guldi, T. Torres. *Chem. Eur. J.*, **2012**, *18*, 1727-1736.

## Results and Discussion



**Scheme 4.** Synthesis of TBDPS-phthalonitrile precursor **10**.

Statistical cyclotetramerization reaction between phthalonitrile **10** (1 eq.) and unsubstituted phthalonitrile (5 eq.) in refluxing *N,N*-dimethylaminoethanol (DMAE) in the presence of zinc acetate and 1,8-diazabicyclo(5.4.0)undec-7-ene (DBU) afforded TBDPS-protected hydroxymethyl-ZnPc **13** in 10% yield. Worth noting, the utilization of bulky TBDPS group as a substituent afforded a straightforward purification of the desired product by solving the problem of solubility. Thus, the major impurity of non-substituted ZnPc with limited solubility was easily separated from the TBDPS-ZnPcs using a hot extraction of the latter by acetone in a Soxhlett apparatus. The desired mono-substituted ZnPc was isolated from the statistical mixture of products by column chromatography. The TBDPS protecting group was then deprotected using tetra-*n*-butylammonium fluoride (TBAF) in acetic acid at room temperature affording hydroxymethyl-substituted Pc **14** in 98% yield. Interestingly, the use of present approach allowed us to isolate **14** in its pure form in 0.5 g scale. This goal would be hard to achieve considering the statistical condensation of phthalonitrile and **11** due to bad solubility of all the Pcs products impossible to separate via conventional column chromatography or recrystallization.



**Scheme 5.** Synthetic scheme leading to ZnPcs **14** and **15**.

Finally, Pc **14** was oxidized with 2-iodoxybenzoic acid (IBX) in DMSO obtaining, after column chromatography, formyl-substituted Pc **15** in 87% yield (Scheme 4). Structural characterization of these compounds was carried out by using mass spectrometry,  $^1\text{H}$  NMR and UV-vis spectroscopy analysis. Thus, characteristic signatures of protons of hydroxymethyl group in ZnPc **14** can be observed as the corresponding triplet at 5.72 ppm and the doublet at 5.13 ppm in its  $^1\text{H}$ NMR spectrum in DMSO- $d_6$  (Figure 41). Differently, the formyl proton of **15** possesses a pronounced singlet at 10.47 ppm. Aromatic protons of the Pc core resonate as two broaden multiplets between 9 and 7 ppm in both compounds.

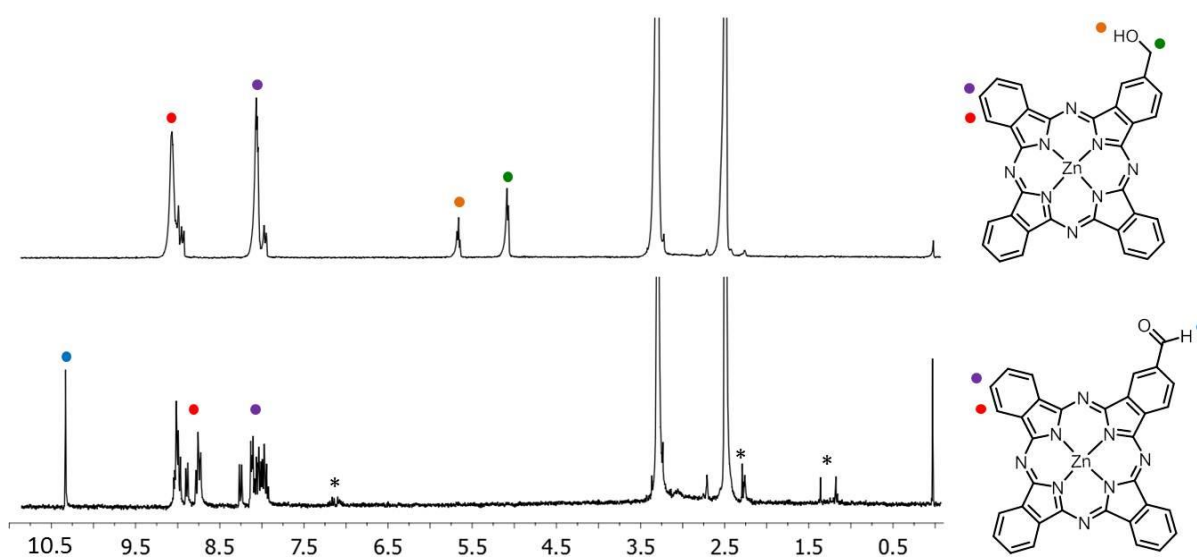
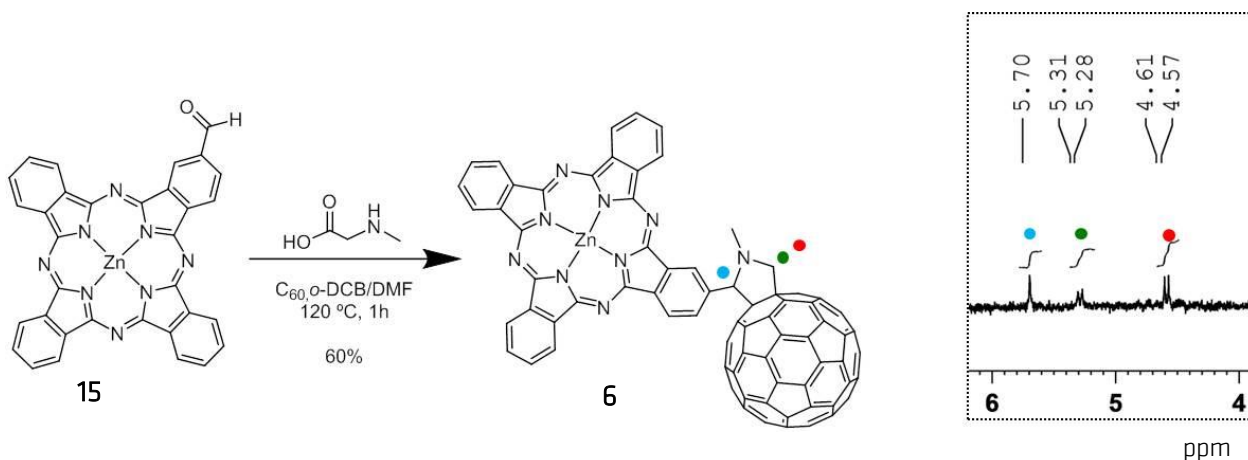


**Figure 41.**  $^1\text{H}$  NMR spectra (300 MHz, DMSO- $d_6$ , 25°C) of hydroxymethyl-ZnPc **14** and formyl-ZnPc **15**. Color code is used for the assignment of protons and asterisks for impurities.

The synthesis of ZnPc- $\text{C}_{60}$  conjugate **6** involved a Prato reaction between precursor aldehyde-substituted ZnPc **15**,  $\text{C}_{60}$  fullerene and sarcosine in *o*-DCB/DMF, affording dyad **6** in 60% yield as a racemic mixture at the methine pyrrolidine carbon atom (Scheme 6). The structural features of compound **6** were confirmed by mass spectrometry,  $^1\text{H}$ -NMR and UV-vis spectroscopy. Thus, MALDI-MS studies of the ZnPc- $\text{C}_{60}$  adduct **6** revealed peak of molecular ion at 1351-1381  $m/z$ , corresponding to the dyad of the proposed structure (Figure 42a). More intense peak at 719.9  $m/z$  is due to the fragmentation taking place and is attributed to the loss of ZnPc moiety. More importantly, characteristic signals of protons for the  $\text{C}_{60}$  pyrrolidine adducts have been observed in the  $^1\text{H}$ -NMR spectrum of **6** in  $\text{CS}_2/\text{THF-}d_8$  (1/1). Thus, geminal pyrrolidine protons resonate as two doublets at 5.30 and 4.59 ppm, whereas the remaining pyrrolidine proton appears as a singlet at 5.70 ppm. Signal of the N-methyl protons can be observed as singlet at 1.29 ppm. The UV-vis spectra

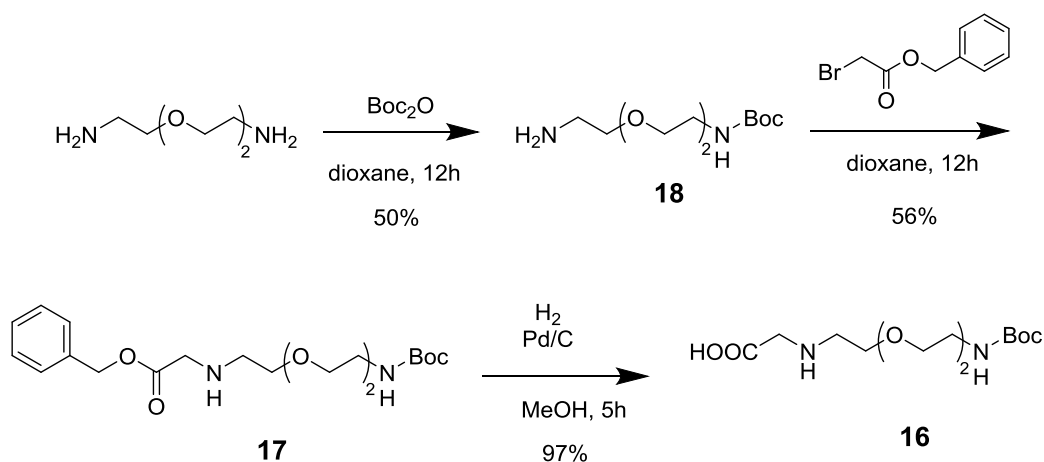
## Results and Discussion

of **6** in solution and thin film will be discussed in comparison with those of other dyads later on in this chapter.



**Scheme 6.** Synthesis of ZnPc- $\text{C}_{60}$  dyad **6**. Inset -  $^1\text{H}$  NMR spectrum (300 MHz,  $\text{CS}_2/\text{THF}-d_8 = 1:1$  vol.,  $25^\circ\text{C}$ ) with characteristic signals of the pyrrolidine unit.

The preparation of amphiphilic analog of **6** - Pc- $\text{C}_{60}$  dyad **7** - required the synthesis of *N*-functionalized glycine **16** that was prepared according to the literature procedure<sup>112</sup> as outlined in Scheme 7. The synthesis of **16** started with the mono protection of 2,2'-(ethylene-dioxy)bis(ethylamine) by reaction with di-*tert*-butyl-dicarbonate ( $\text{Boc}_2\text{O}$ ) in dioxane leading to compound **18** in 50% yield. The remaining amino group in **18** was then protected using benzyl-bromoacetate affording compound **17** in 56% yield. Compound **16** was finally obtained in a 97% yield by removal of the benzylic group in **17** in the presence of  $\text{H}_2$  and Pd/C as catalyst.

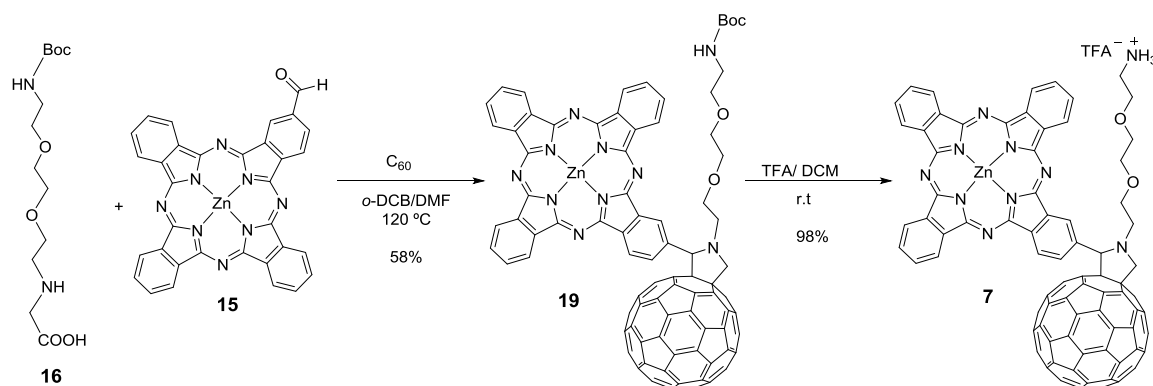


**Scheme 7.** Synthesis of *N*-functionalized glycine **16**.

<sup>112</sup> G. Pastorin, W. Wu, S. Wieckowski, J.-P. Briand, K. Kostarelos, M. Prato, A. Bianco, *Chem. Commun.*, **2006**, 1182-1184.



1,3-Dipolar cycloaddition reaction between aldehyde-functionalized Pc **15**, *N*-functionalized glycine **16** and C<sub>60</sub> fullerene afforded ZnPc-C<sub>60</sub> dyad **19** (Scheme 8).



**Scheme 8.** Synthesis of amphiphilic ZnPc-C<sub>60</sub> dyad **7**.

Formation of the dyad **19** was confirmed by MALDI TOF mass spectrometry performed in a negative mode in the presence of *trans*-2-[3-(4-*tert*-Butylphenyl)-2-methyl-2-propenylidene]malononitrile (DCTB) as a matrix. A peak of molecular ion observed at 1568.3 *m/z* corresponds to the proposed structure of **19** (Figure 42b). As in the case of the dyad **6**, the more intense peak at 994.2 *m/z* corresponds to the fullerenic unit after the loss of the ZnPc moiety. The *tert*-butoxycarbonyl (Boc)-protected amino end group in **19** was quantitatively deprotected an excess of trifluoroacetic acid (TFA) to afford amphiphilic Pc-C<sub>60</sub> conjugate **7** in 98% yield. The presence of one positive charge compensated by trifluoroacetate anion makes this dyad insoluble in aromatic solvents. However, presence of the terminal ammonium group is supposed to assist in dispersion of this dyad in water.

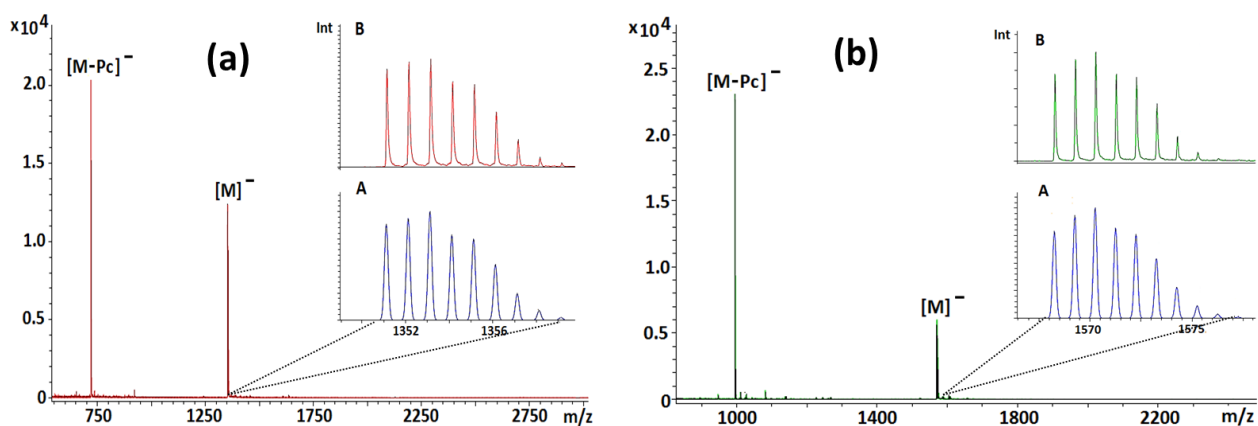
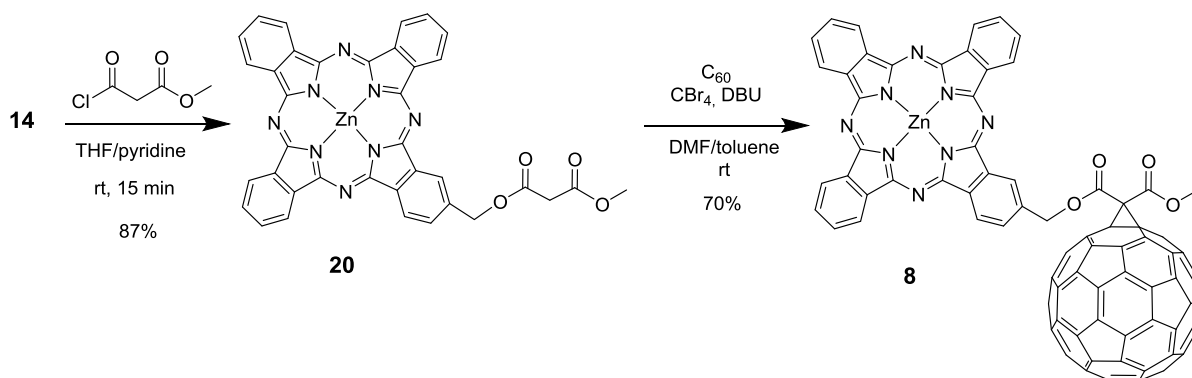


**Figure 42.** MALDI-TOF MS spectra (DCTB) of a) ZnPc-C<sub>60</sub> dyad **6** and b) its analog **19**. Inset: A) calculated isotopic pattern for the same peak, B) isotopic resolution of the MALDI-TOF main peak.

## Results and Discussion

A different synthetic strategy was used for the preparation of the Pc-C<sub>60</sub> dyad **8**, which involved the synthesis of a malonyl-substituted Pc **20** in 87% yield by reaction between hydroxymethyl ZnPc **14** with chloromalonyl ester in the presence of pyridine. Subsequently, malonyl-substituted Pc **20** dissolved in DMF was added to a toluene solution of C<sub>60</sub> fullerene and CBr<sub>4</sub> in the presence of an excess of DBU affording Pc-C<sub>60</sub> conjugate **8** in 70% yield *via* a Bingel-Hirsch reaction (Scheme 9).



**Scheme 9.** Synthesis of Pc-C<sub>60</sub> dyad **8**.

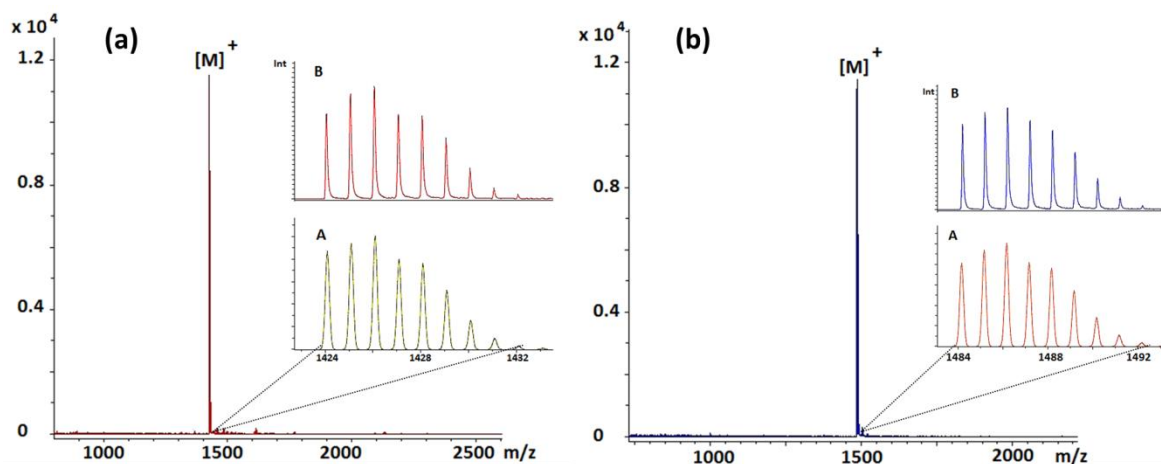


**Figure 43.** MALDI-TOF MS spectra (DCTB) of a) ZnPc-C<sub>60</sub> dyad **7** and b) its enlarged analog **8**. Inset: A) calculated isotopic pattern for the same peak, B) isotopic resolution of the MALDI-TOF main peak.

Full spectroscopic characterization of **8** has been performed, confirming its unambiguous formation and isolation in a pure form. Thus, MALDI TOF mass spectrum performed in a positive mode with DCTB as a matrix revealed the presence of a peak at 1424.1 m/z corresponding to [M]<sup>+</sup> molecular ion (Figure 43a). <sup>1</sup>H NMR spectrum showed characteristic singlet of methylene protons at 6.08 ppm, and a singlet of the three methyl protons at 4.20

ppm (Figure 44). In a contrast, corresponding signals of the precursor ZnPc **20** were observed as the two singlets at 5.78 and 3.81 ppm, whereas the methylene protons of the malonyl fragment resonate as singlet at 3.58 ppm (Figure 44). Worth noting, a 1:1 mixture of CS<sub>2</sub>/THF-*d*<sub>8</sub> was found successful to dissolve the dyad till the concentration suitable for NMR analysis. Presence of the malonyl fragment in **8** was expected to enlarge the distance between ZnPc and C<sub>60</sub> units as well as to provide a free rotation within the conjugate.

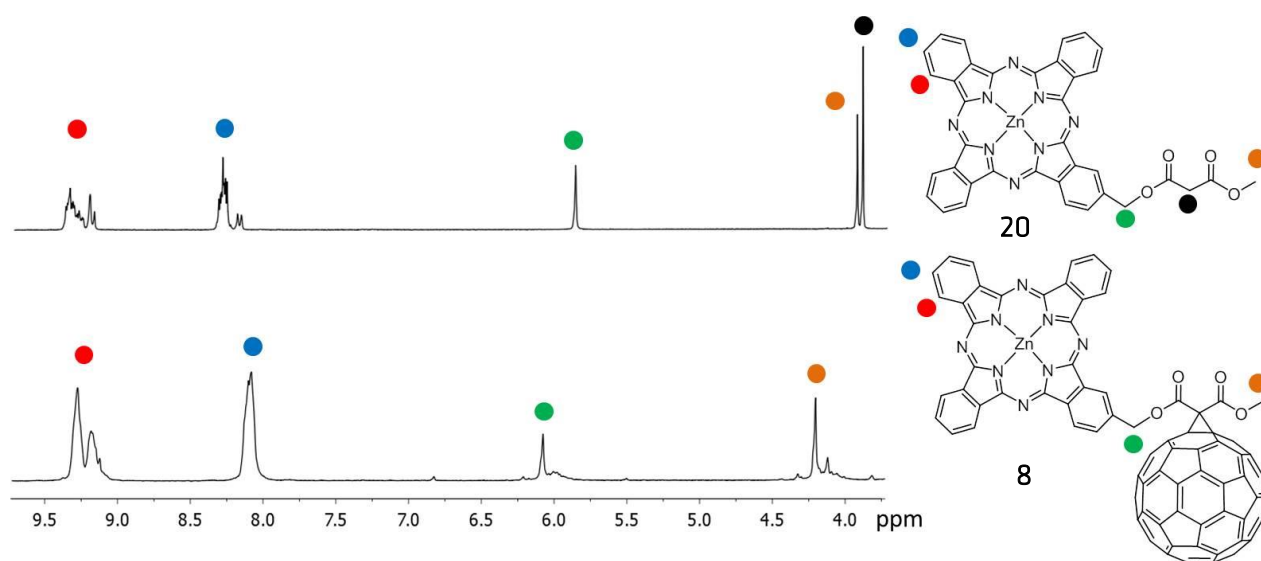


**Figure 44.** <sup>1</sup>H NMR spectra (300 MHz, CS<sub>2</sub>/THF-*d*<sub>8</sub> 1:1, 25°C) of malonatomethyl-ZnPc **20** and ZnPc-C<sub>60</sub> conjugate **8**. Color code is used for the assignment of protons.

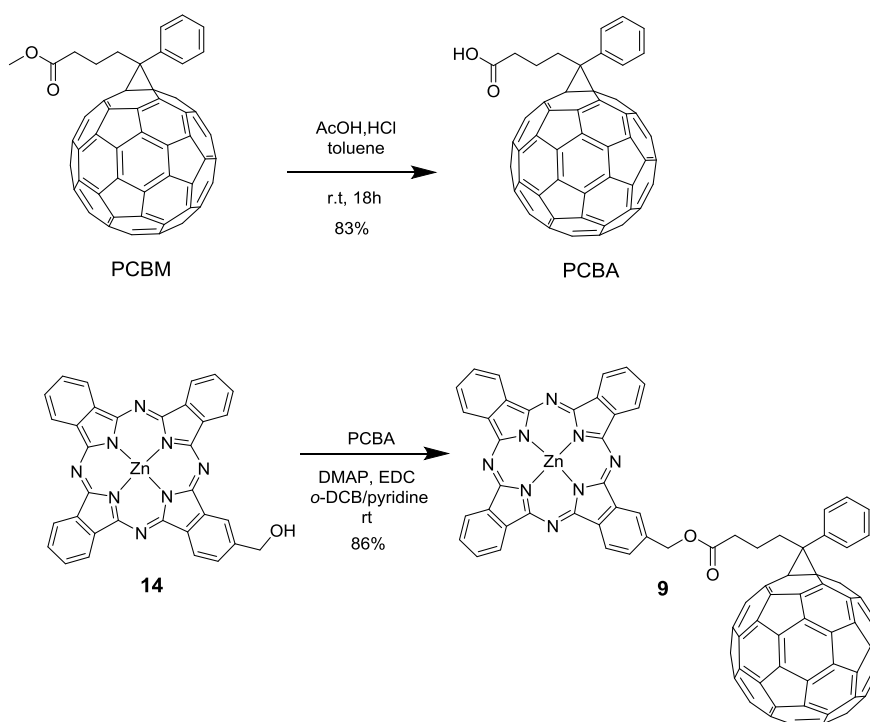
Finally, an extended analog of **8** was designed as ZnPc linked to C<sub>60</sub> fullerene in a dyad **9** via a flexible oxymethylbutyric spacer following the procedure reported by Guldi *et al.* for the synthesis of tetra-phenylporphyrin covalently connected to C<sub>62</sub>@I<sub>h</sub>-C<sub>80</sub> metallofullerene.<sup>113</sup>

The ZnPc bearing 4-benzoylbutyric acid tosylhydrazone **21** has been synthesized for its further addition to the fullerene moiety. For this purpose, ZnPc **22** was reacted in Dean-Stark apparatus with *p*-toluene-sulfonylhydrazide (tosylhydrazone) in toluene/pyridine solvents mixture at reflux overnight to afford **21** in 50% yield (Scheme 10). In its turn, ZnPc oxymethyl ester of 4-benzoylbutyric acid **22** was prepared via esterification reaction of hy-

<sup>113</sup> D. M. Guldi, L. Feng, S. G. Radhakrishnan, H. Nikawa, M. Yamada, N. Mizorogi, T. Tsuchiya, T. Akasaka, S. Nagase, M. A. Herranz, N. Martin, *J. Am. Chem. Soc.*, **2010**, 132, 9078-9086.

## Results and Discussion

droxymethyl ZnPc **14** and 4-benzoyl butyric acid in a presence of 1-ethyl-3-(3-dimethylaminopropyl)carbodiimide (EDC) and catalytic amounts of 4-dimethylaminopyridine (DMAP) in THF at r.t. in 81% yield. The subsequent addition of sodium methoxide to **21** in anhydrous reaction media was supposed to induce the transformation of the tosylhydrazone moiety into highly reactive diazo group binding *in situ* to C<sub>60</sub> via cyclopropanation reaction.<sup>114</sup> Instead, the degradation of **21** occurred, yielding the ZnPc **14**. However, an alternative route for the preparation of **9** was attempted as the one described below.

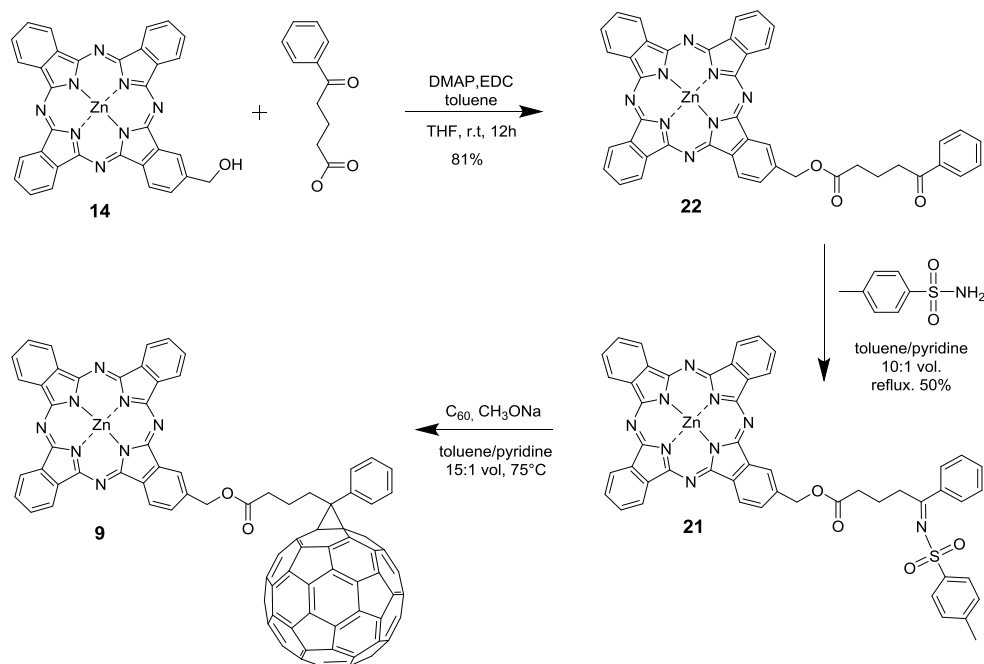


**Scheme 10.** First route for the synthesis of ZnPc-C<sub>60</sub> dyad **9**.

Pc-C<sub>60</sub> conjugate **9** was obtained in 86% yield by reaction of esterification between hydroxymethyl-Pc **14** and [6,6]-phenyl-C<sub>61</sub>-butyric acid (PCBA). This latter fullerene derivative was synthesized by acid-catalyzed hydrolysis of the methyl ester PCBM received from commercial supplier (Scheme 11).<sup>115</sup>

<sup>114</sup> R. K. M. Bouwer, J. C. Hummelen, *Chem. Eur. J.*, **2010**, 16, 11250-11253.

<sup>115</sup> M. Drees, H. Hoppe, C. Winder, H. Neugebauer, N. S. Sariciftci, W. Schwinger, F. Schffler, C. Topf, M. C. Scharber, Z. Zhun, R. Gaudiana, *J. Mater. Chem.*, **2005**, 15, 5158-5163.



**Scheme 11.** Second route for the synthesis of ZnPc-C<sub>60</sub> dyad **9**.

MALDI TOF mass spectrum performed in a positive mode with DCTB as a matrix revealed the presence of a peak at 1482.2 m/z corresponding to [M]<sup>+</sup> molecular ion (Figure 43b). Notably, no significant fragmentation, if any, has been observed in mass-spectrometric data of **9** and **8**, in comparison with those of the “Prato-type” dyads **6** and **19** (Figure 42), confirming a strong influence of the retro-Prato related processes on the stability of the ZnPc-C<sub>60</sub> dyads.<sup>116</sup> <sup>1</sup>H NMR spectrum recorded at 300 MHz in CS<sub>2</sub>-THF-*d*<sub>8</sub> 1:1 mixture showed characteristic multiplets of the ZnPc core protons at δ 9.41-9.22 and 8.20-8.07 ppm (Figure 45). Eight methylene protons appeared as the four groups of signals at δ 5.68 (s, CH<sub>2</sub>), 3.00 (m, CH<sub>2</sub>), 2.75 (m, CH<sub>2</sub>) and 0.98 (m, CH<sub>2</sub>) ppm. Finally, the phenyl protons were observed at δ 7.52 (t, 2H, CH<sub>aryl</sub>), 7.45 (t, 1H, CH<sub>aryl</sub>) and 7.20-7.05 (m, 2H, CH<sub>aryl</sub>) ppm.

<sup>116</sup> Martín N., Altable M., Filippone S., Martín-Domenech A., Echegoyen L., Cardona C.M. *Angew. Chem. Int. Ed.*, **2006**, 45, 110-114.

## Results and Discussion

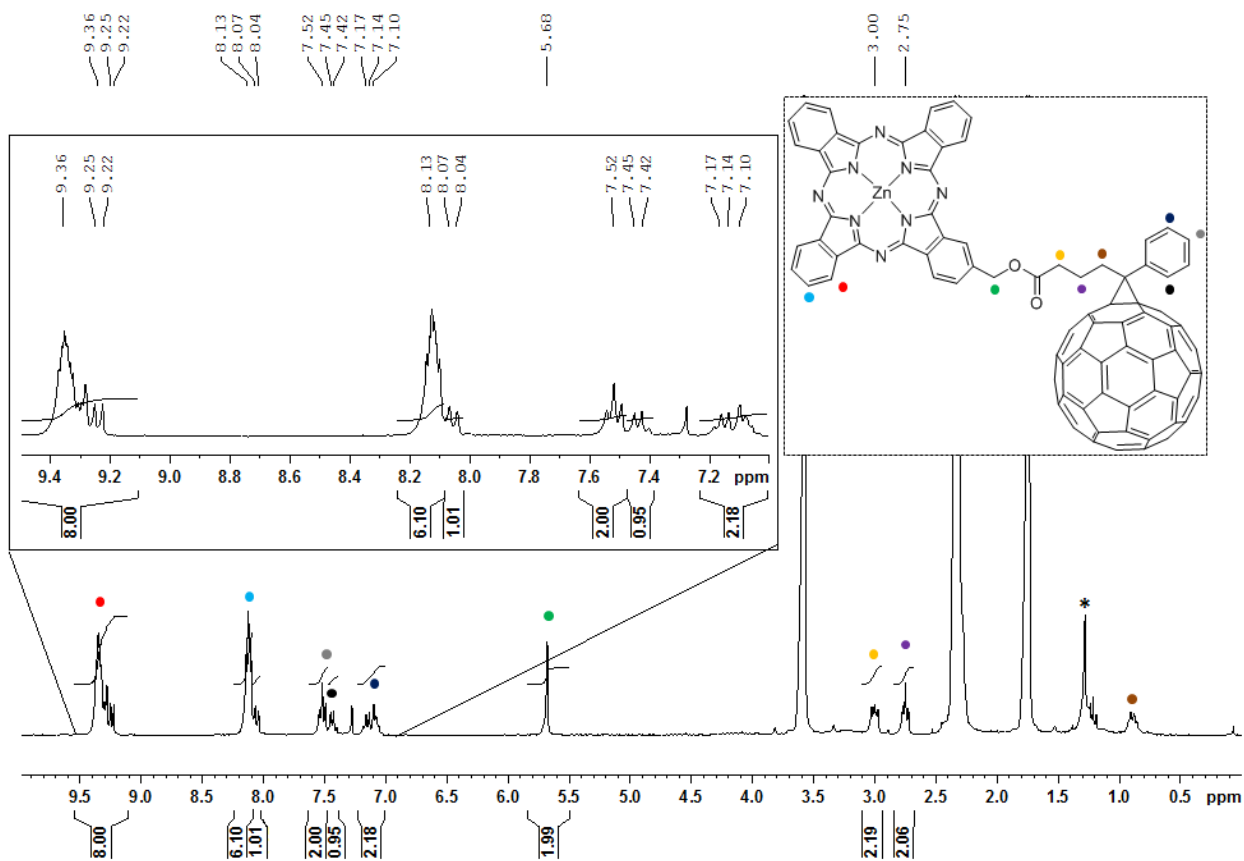


**Figure 45.**  $^1\text{H}$  NMR spectrum (300 MHz,  $\text{CS}_2/\text{THF}-d_8$  1:1, 25°C) of ZnPc-C<sub>60</sub> dyad **9**.

## 4.1.2 Photophysical studies of the dyads

First insights into the ground state absorption features of the ZnPc-C<sub>60</sub> dyads **6**, **8** and **9** were obtained from their UV-vis spectra in solution and in the thin films. Dyad **1** - a *tert*-butyl substituted analogue of **6** - has also been prepared in this work according to the procedure developed earlier by our group.<sup>35</sup>

In order to utilize it as a reference compound. Thus, dilution spectra in of all the dyads in toluene are shown on the Figure 46. As it can be seen, spectrum of each dyad results from a superposition of absorptions of fullerene and ZnPc units. Thus, they can be characterized by the presence of the two intense bands – a sharp absorption at around 675 nm typical for the ZnPc Q-band, and a broad peak that results from the sum of fullerene absorption and a ZnPc B-band at around 340 nm. More interestingly, ZnPc and fullerene units seem to reveal minimal interaction in the ground state in solution. The main indication of the latter comes from the fact that ZnPc Q-bands reveal only a slight shift depending on the nature and rigidity/flexibility of the spacer. The ZnPc Q-bands appears at 673 nm in UV-vis absorption spectrum of **8** and **9**, whereas those are slightly shifted bathochromically to 676 and 680 nm in **6** and **1**, respectively, as a function of shorted distance between the two photoactive units. The latter is a direct indication of a slightly lower LUMO of the “prato-type” dyads **6** and **1**.

Turning to intermolecular effects of dyads in solution, it is evidenced from the Figure 46 that no interactions, such as  $\pi$ - $\pi$  stacking, take place within a given range of concentrations in toluene. Thus, no shift of the ZnPc Q-band was observed upon dilution/addition of coordinating solvent, such as pyridine or THF, in contrast to a study on ZnPc aggregation effects reported recently by our group<sup>117</sup> as well as those described elsewhere.<sup>118,119</sup> However, a clear dependence of molar absorptivity of **6** on the concentration evidences its decreased solubility in toluene. In comparison, the other dyads remain their extinction coefficients unchanged and dependent on the type of the spacer, revealing  $\epsilon \approx 18 \times 10^4$  [dm<sup>3</sup> mol<sup>-1</sup> cm<sup>-1</sup>] for **8** and **9**,  $19 \times 10^4$  [dm<sup>3</sup> mol<sup>-1</sup> cm<sup>-1</sup>] for **1**, and  $\epsilon \approx 14 \times 10^4$  [dm<sup>3</sup> mol<sup>-1</sup> cm<sup>-1</sup>] for **6**.

<sup>117</sup> G. Bottari, O. Trukhina, A. Kahnt, M. Frunzi, Y. Murata, A. Rodriguez-Forteza, J. M. Poblet, D. M. Guldi, T. Torres, *Angew. Chem. Int. Ed.*, **2016**, 55, 11020.

<sup>118</sup> A. W. Snow, in *The Porphyrin Handbook*; K. M. Kadish, K. M. Smith, R. Guillard, Eds.; Academic Press: San Diego, CA, 2003; Vol. 17, pp 129-176.

<sup>119</sup> a) M. Katayose, S. Tai, K. Kamijima, H. Hagiwara, N. Hayashi, *J. Chem. Soc., Perkin Trans.*, **1992**, 2 403-409; b) J. M. Kroon, B. M. Koehorst, G. M. Sanders, E. J. R. Sudholter, *J. Mater. Chem.*, **1997**, 7, 615-624.

## Results and Discussion

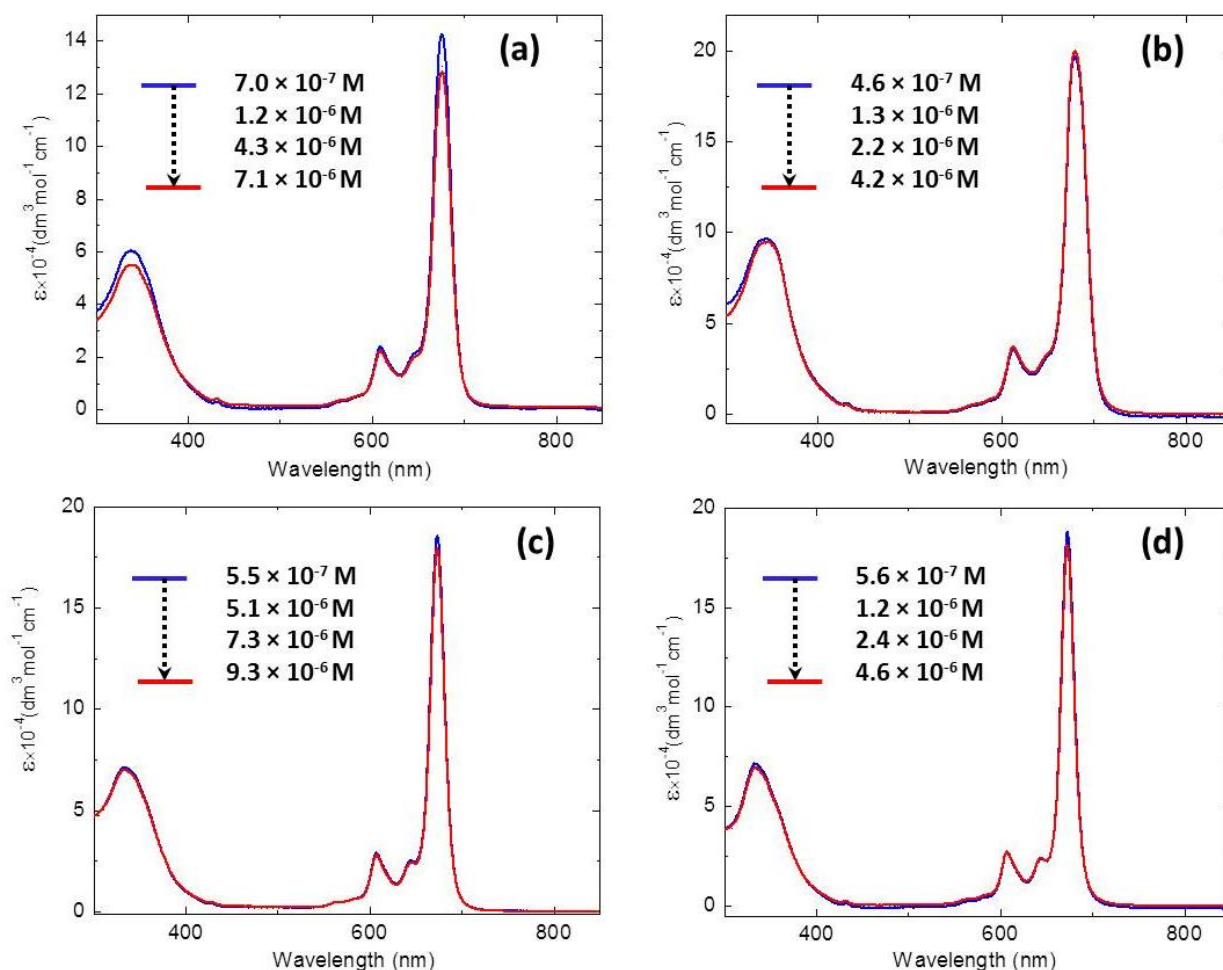


**Figure 46.** Effect of dilution on the UV-vis absorption (toluene, 25 °C) of ZnPc-C<sub>60</sub> dyads a) **6**, b) **1**, c) **8** and d) **9**.

UV-vis ground state absorption features of the thin films of the dyads were also deemed important for the estimation of supramolecular interactions and study of the charge separated events in the solid state. For this purpose, the drop casted films of the dyads **1**, **6**, **8** and **9** were prepared on glass substrates, utilizing the corresponding  $5 \times 10^{-6}$  M saturated solutions in THF. In addition, films of the dyads in a matrix of acrylic glass, containing 5 wt. % of poly(methyl-methacrylate) (PMMA) were fabricated by spin coating of the corresponding solutions in THF on glass substrates at 1500 r.p.m for 10 sec. Embedding of the dyads in PMMA matrix allowed preparation of the supercooled liquid phase at room temperature for revealing possible supramolecular effects in the solid state, if any, being more defined in comparison with those of drop casted films. The corresponding UV-vis absorption spectra in toluene, PMMA matrix and in drop casted film are represented in the Figure 47.



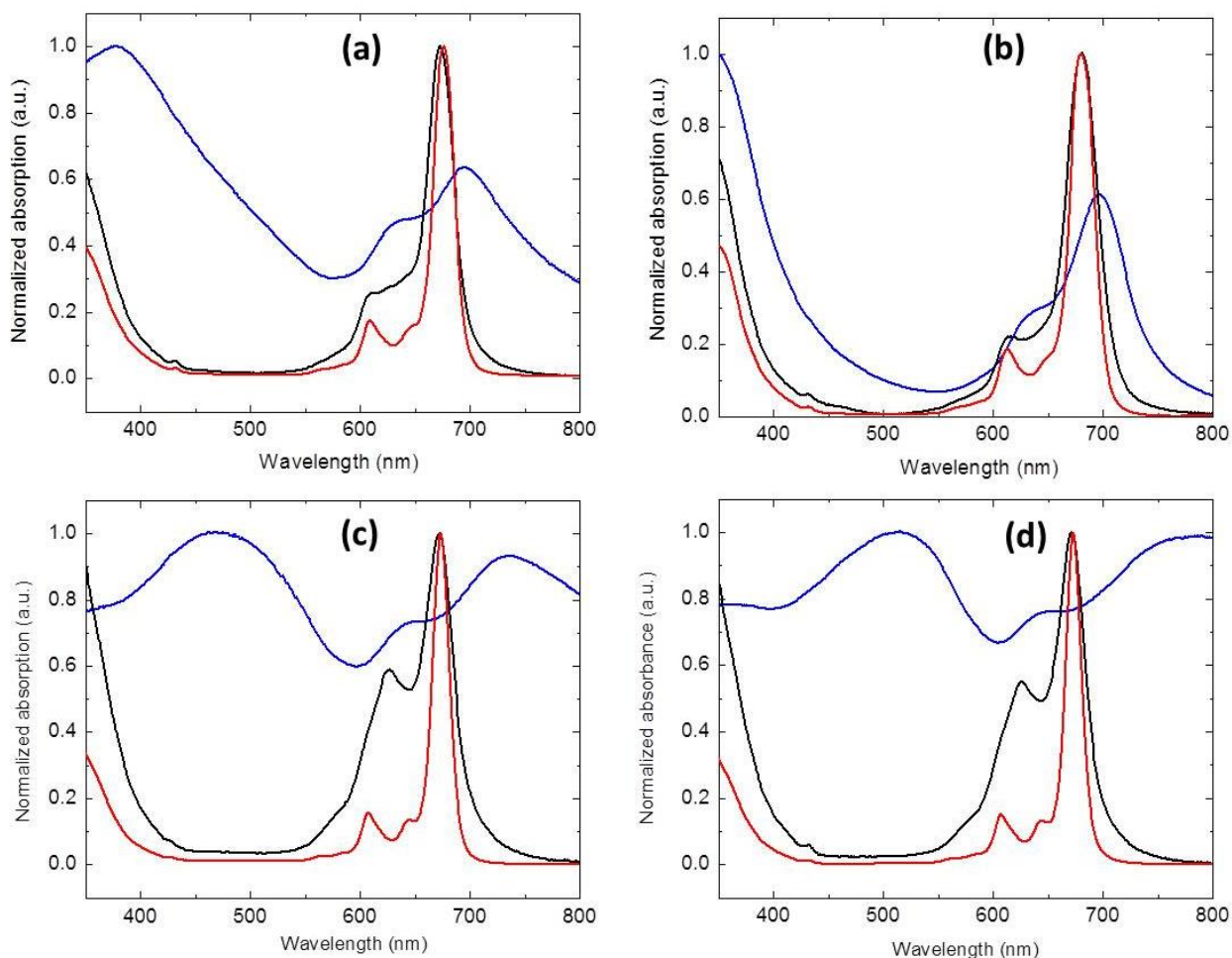


**Figure 47.** UV-vis normalized absorption spectra of ZnPc-C<sub>60</sub> dyads in toluene (red line), in PMMA matrix on glass (5 wt. %, black line) and those of a thin film drop casted from THF on glass (blue line) of ZnPc-C<sub>60</sub> dyads a) **6**, b) **1**, c) **8** and d) **9**.

In PMMA matrix, the characteristic ZnPc Q-band experiences no shift (black lines) in comparison with those in toluene (red lines). However, the evident broadening of the major absorption features takes place, being caused by the shorter distances between dyad molecules, if being compared with those in toluene solution. Interestingly, the rigid spacer between ZnPc and C<sub>60</sub> units in dyads **6** and **1** results in fewer changes of the ZnPc Q-band in frozen solution. In a contrast, UV-vis absorption features of **8** and **9** vary significantly when the latter lose their flexibility in PMMA matrix. However, no spectral evidence, such as bathochromic or hypsochromic shifts, of any ordered supramolecular aggregates driven by intermolecular forces or matrix itself could be observed. When turning to absorption features of the dyads in drop casted films, the drastic changes can be found (Figure 47, blue lines).

## Results and Discussion

Those can be characterized by broadening of all the absorption bands and their clear bathochromic shifts in comparison with spectral features in toluene and in PMMA. A stronger scattering that causes the elevation of the baseline absorption in spectra of **8** and **9** indicates on the precipitation of the corresponding dyads from their THF solution in the form of larger aggregated species on glass substrate upon drop casting. Whereas, the size of the corresponding agglomerates is smaller for **6** and the least for **1**, bearing a tetra-tert-butyl substituted ZnPc. Obviously, the intermolecular distances are the least for the drop casted films. In line with that, the interaction between neighboring molecules increases with the decrease of separation distances, resulting in an additional energy shifts of the ZnPc and C<sub>60</sub> corresponding absorptions.

Next, ultrafast charge generation in ZnPc-C<sub>60</sub> dyads has been studied by femtosecond transient absorption spectroscopy in THF solutions, PMMA matrix and in drop casted films with the aim to define the possible photophysical processes, such as photoexcitation and charge generation with the corresponding charge separation (CS) and charge recombination (CR) times, in ZnPc and C<sub>60</sub> units. Additionally, we were interested in comparing the observed phenomena in solution and in the solid state, with the aim to reveal the influence of the latter on charge separation dynamics. The global fitting has been used for the data analysis a general method. Pump pulses at 387.5 nm (around 200- 1200 nJ pulse energy with about 300  $\mu\text{m}$  spot size) have been used together with probe pulses of 480 – 1300 nm, recorded by a double line single shot capable spectrometer. Due to the short pump wavelength employed, the excitation of both photoactive units (ZnPc at its Soret band and the C<sub>60</sub>) was considered, accounting on (i) energy/charge transfer from C<sub>60</sub>\* to ZnPc, (ii) ultrafast charge generation directly from the ZnPc Soret band and (iii) ultrafast triplet generation from the ZnPc Soret band. Since the fact that all these ultrafast processes leave characteristic spectral signatures in femtosecond transient absorption spectra (TA), it should be possible to identify them by global spectral analysis.

Before turning to an in depth analysis of the TA spectra of the dyads, we will define the most characteristic features of the photoinduced processes of ZnPc. In general, a global kinetic fitting analysis results in a set of characteristic spectra, i.e. *evolution-associated differential spectra* (EADS), which possess a definite characteristic lifetime. From the spectral shapes of the EADS, the corresponding attribution to either photo-excited states or to superpositions of them is possible.

In Figure 47a, the two EADS of ZnPc **14** in THF are shown, having lifetimes of 13 ps and 1.8 ns, respectively. The similarity of their shapes indicates the existence of the only dominant photoexcited state. Their definition becomes possible due to the characteristic sharp absorption bands of the ZnPc molecule.

The preliminary analysis of EADS includes the search of signatures of any excited states, regardless their singlet, triplet or charged nature, depletes the number of available molecules in the ground state. Therefore, the ground state is considered to be bleached to a certain extent, being called *transient photobleach* (PB). Taking into account the ground state absorption of ZnPc, consisting of a sharp (00) transition at 1.82 eV and a clearly resolved vibronic replica at 2.03 eV, these two features are expected to form an integral part of any excited state spectra. In fact, looking at Figure 48, the both transient photobleaches - PB00 and PB01 – can be satisfactory found.

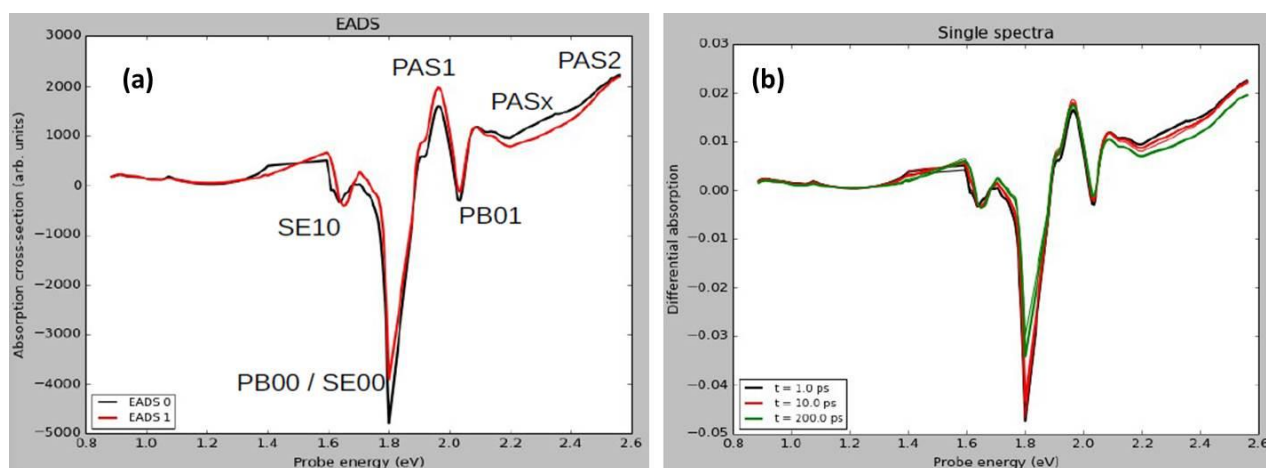


**Figure 48.** a) EADS from the global fitting analysis of ZnPc **14** solution in THF, b) TA spectra at specified time delays (thin lines) and a global fit (thick line).

From Einstein relations, and neglecting a Stokes shift, the oscillator strength for stimulated absorption is equal to that for stimulated emission. As a consequence, in the excited state spectra, the *stimulated emission* (SE) feature of the (10) transition can be observed at 1.65 eV (Figure 48a). Spectral analysis shows that the oscillator strength of SE10 is similar to PB01, which means that the ZnPc singlet state is the dominating excited state, and the only excited state occurring after 10 ps. Especially, the fact that the ratio SE10/PB01 stays constant between 10 and 200 ps (Figure 48b), confirms the observation of none significant triplet formation in a given time window.

## Results and Discussion

The latter means that both *photoinduced absorption* (PA) bands of EADS1, namely PAS1 at 1.95 eV, and PAS2 at 2.55 eV, can be attributed to excited state absorptions of the singlet state. Finally, a small band PASx at 2.3 eV in EADS0 with a lifetime of 13 ps should be considered as a polaronic state, which agrees with a presence of the other sharper polaron band at 1.4 eV. In other words, this weak band is caused by ionization involving solvent molecules, followed by geminate recombination with 13 ps recombination time. Singlet states cause only negligible PA bands in the near infrared. Minor bands at 0.9 and at 1.1 eV are one order of magnitude weaker than PAS1 and PAS2, and thus, they cannot be associated the ZnPc singlet state absorption.

### 4.1.2.1 Photophysics in THF solution

When turning to photophysical properties of ZnPc-C<sub>60</sub> dyads, we began our study from the reference system **1**, taking into account its photophysical behavior has been previously reported by our group.<sup>35</sup> Thus, three EADS of **1** in THF are shown on the Figure 49a. In overall, EADS0 of **1** is similar to EADS1 of ZnPc **14** (Figure 49a), showing SE10, PAS1 and PAS2. The latter indicates the predominant generation of singlet excitons following the pump at 387 nm with 150 fs pulses and 560 nJ pulse energy. In a contrast, EADS1 differs strongly from EADS0 indicating the occurrence of photophysical processes. In EADS1, singlet excited state related bands, namely SE10, PAS1 and PAS2, disappear, whereas, the new absorption features evolve at 1.25, 1.4, and 2.35 eV, associated with photoinduced absorption by the charged acceptor (PAA) and that of the charged donor - PAD1 and PAD2, respectively. Since EADS0 and EADS1 are well distinct, the rate constant  $k_1$  can be directly associated with charge separation. EADS2, on the other hand, is similar to EADS1, which leads to the conclusion that EADS2 is still the same state, namely the charge separated state, but that charge recombination is non-exponential with two lifetimes,  $1/k_2$  and  $1/k_3$ . Being structurally close to **1**, dyad **6** in a similar manner reveals EADS0 dominated by singlet excited states, whereas EADS1 represents only polarons and no visible contribution of singlet states (Figure 49b). EADS1 is only polarons, so we consider the presence of PCBM excitons as minor. Charge recombination divides into a fast and a slow part, like in **1**.

When turning to the dyads **8** and **9**, possessing flexible spacers and a certain degree of rotational freedom, the photophysical events become more complex. Thus, in TA spectra of **8**, EADS0 contains characteristic features of the ZnPc singlet excited state, whereas the EADS2 evolves as fingerprints of the charge separated state (Figure 49c). However, EADS1 appears as an intermediate state between those two: PAD1 is not yet fully developed, whereas the band at 2.4 eV seems to be a compromise between PAS2 and PAD2. EADS1 clearly shows some SE10 which EADS2 lacks. Importantly, the total integral of PB01 seems to increase from EADS0 to EADS1. All these observations can be explained by the following scenario. Most dyades are excited on the ZnPc side, and perform charge separation as second step. Some dyades are however excited on the C<sub>60</sub> side. Since the neutral C<sub>60</sub>\* excited state causes very little PA or PB, these dyades remain invisible in EADS0 but then perform energy transfer to ZnPc, creating ZnPc singlet excited states.

## Results and Discussion

In other words, while the initial singlet states of ZnPc site are charge separated, new ones get evolved from the C<sub>60</sub> site. Once all, the C<sub>60</sub> singlet states have been transferred to ZnPc, the recombination of the charge separated state occurs in 320 ps, much slower than in **1**, where it occurs in 40 ps.

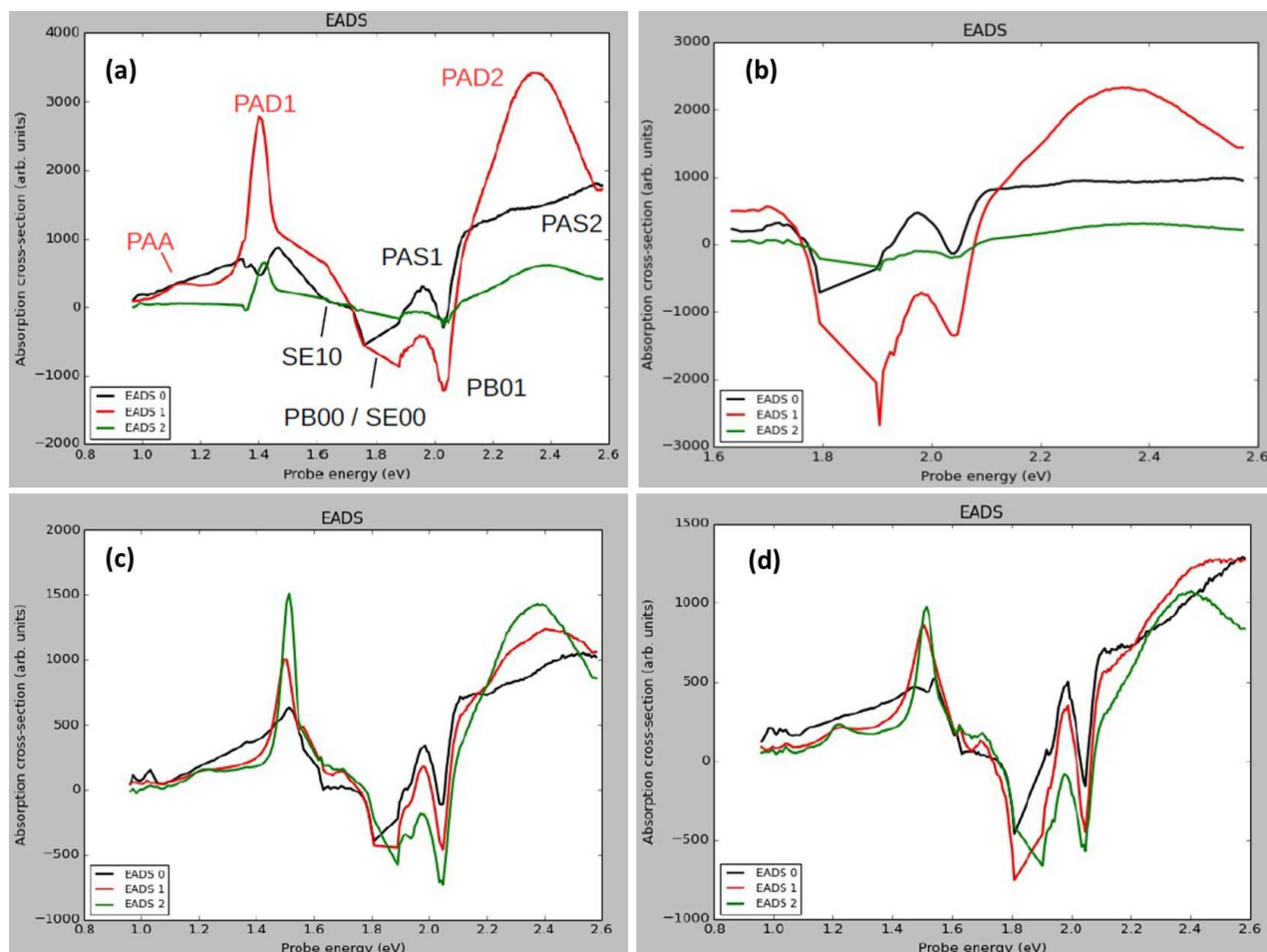


**Figure 49.** a) EADS from global fits for TA spectra of ZnPc-C<sub>60</sub> dyads a) **1**, b) **6**, c) **8** and d) **9** in THF, obtained after pumping at 387 nm with 150 fs, pulses and 560 nJ pulse energy. In panel (a), the nomenclature of the photoinduced bands is introduced as PB, SE, PAS, PAA, PAD corresponding to photobleaching, stimulated emission, photoinduced absorption of singlet, photoinduced absorption of acceptor and photoinduced absorption of donor, respectively.

Regarding the dyad **9**, the situation is similar to **8**, in that charge separation occurs with two lifetimes. EADS1 shows evidence of both - singlet and polaronic states, showing that the 387 nm pump pulse creates some C<sub>60</sub> excitons which are transferred to ZnPc from EADS0 to EADS1 (Figure 49d).

An important difference between **8** and **9** is that in the latter, the integral of PB01 is reduced going from EADS1 to EADS2. Also the integrals of the PAD1 and PAD2 bands are clearly reduced, which is explained by a certain amount of geminate recombination on a 10 ps time scale, typical for such a process. On the other hand, the integral of PAA at 1.25 eV is not reduced, but even increased, which agrees with our model of delayed charge separation after exciton transfer from C<sub>60</sub> to ZnPc. In summary, in THF solution, we find charge separation times from 1 -2 ps for all samples, and recombination times around 50 ps for **1** and **6**, and around 500 ps for **8** and **9**.

### 4.1.2.2 Photophysics in PMMA films on glass

TA spectra of the dyads in PMMA matrix are shown on the Figure 50. In the case of **1**, subpicosecond charge separation and slow recombination of about 900 ps take place (Figure 50a). No sign of non-geminate recombination could be observed. In Figure 50b, **6** is reproduced without residuals even using only two states. In overall, subpicosecond charge separation and recombination on a time scale of roughly 1 ns evolve, being independent of pump intensity. In Figure 50c, the EADS of a global fit of **8** in PMMA matrix are given. Notably, in thin films, the PB 00 / SE 00 band at 1.87 eV is fully rendered because the material was not fully absorbing at the Q band maximum like the THF solutions. This makes it easy to trace ZnPc singlet excitons in PMMA films. As mentioned previously, a PB band represents always the sum of all possible photoexcitations of ZnPc, while an SE is specific for the singlet exciton. As it can be clearly observed from the Figure 50c, PB01 is increasing from EADS0 EADS1, showing that the total number of excited ZnPc species increases. Thus, the PB00 accordingly increases. On the other hand, decreasing SE00/PB00 band indicates the corresponding decrease of the singlet states. The decrease of singlets continues from EADS1 to EADS2, showing on-going charge separation. In summary, the behavior of **8** is similar in solution and PMMA films. Table 1 however shows that charge recombination proceeds more slowly in PMMA films. The recombination coefficient does not depend strongly on intensity, showing that non-geminate recombination is a minor effect in PMMA dissolved **8**. Thus, the slower recombination of **8** in PMMA might point to the necessity of flexible linkers between the ZnPc and C<sub>60</sub> moieties. In PMMA, the moieties can no longer move so freely.

## Results and Discussion

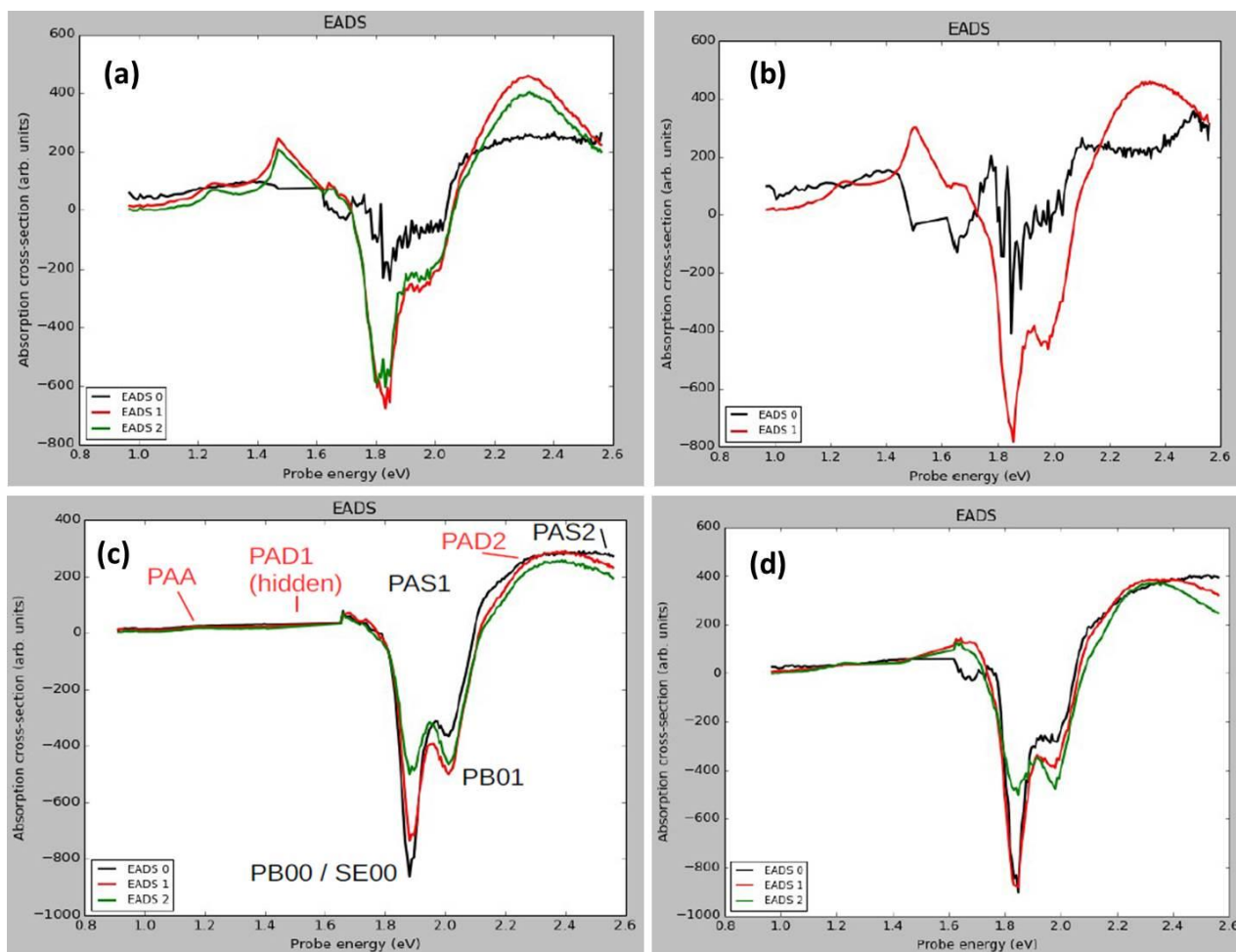


**Figure 50.** a) EADS from global fits for TA spectra of ZnPc-C<sub>60</sub> films a) **1**, b) **6**, c) **8** and d) **9** in PMMA matrix on glass, obtained after pumping at 387 nm with 150 fs, pulses and 560 nJ pulse energy. In panel (c), the nomenclature of the photoinduced bands is introduced as PB, SE, PAS, PAA, PAD corresponding to photobleaching, stimulated emission, photoinduced absorption of singlet, photoinduced absorption of acceptor and photoinduced absorption of donor, respectively.

Finally, EADS of **9** are shown on the Figure 50d. Comparison of the EADS of **8** and **9** shows that the photophysics might be more complex than assumed previously. The ratio (SE00+PB00)/PB01 is ascribed to the presence of singlet states. In Figure. 50d, we can see the SE10 band in EADS0 (at 1.65 eV), so we can test this hypothesis. The SE10 band is completely gone in EADS1, and at the same time, the strength of the PB01 band increases relative to the 00 transitions of SE and PB. Both observations are consistent with singlet disappearance and an increase of the overall population of ZnPc excited states. However, by comparing EADS1 and EADS2: from the ratio of PB01 and the 00 transitions of PB and SE, we would conclude a further dramatic decrease of singlet population. This is however not confirmed by the SE10 band, which is already completely gone in EADS1.



The picture becomes clearer upon looking at 2.15 eV. There, a shoulder is present which agrees with the position of the second vibronic of the ground state absorption, and therefore can be associated with PB02. The strength of this PB02 transition increases strongly from EADS0 via EADS1 to EADS2, and especially from EADS1 to EADS2, where the relative increase is much more than of the respective PB01 transition. We conjecture therefore that apart from the singlet/polaron ratio, also the Huang-Rhys factor is changing over time. This gives important insight into morphology. A larger Huang-Rhys factor means that the potentials of ground and excited state become more dissimilar over time. A bleach of one molecule cannot change over time, since irrespective of the geometry that the excited state attains over time, it is always the relaxed ground state which is the reference for the bleach in the transient absorption experiment. Changing bleach is therefore always a sign of excited state mobility towards specific sites. An alternative explanation could be the built-up of a PA band over time, superposing the 00 transitions more than the 01 one. In Figure 50d, we see that the PAA band of C<sub>60</sub>(-) becomes stronger from EADS1 to EADS2, while the corresponding PAD2 band at 2.35 eV does not get stronger. This might point to a contribution of a two steps charge transfer, where first Pc<sup>+</sup>;Pc<sup>-</sup> charged pairs are formed (this is not possible in solution but possible in films although we would expect it more in dense films and not so much in PMMA films), and later on the ZnPc(-) is transferred to PCBM, where it is energetically stabilized. As in the case of **8**, we find no clear sign of non-geminate recombination in **9** by looking at the charge recombination coefficient as function of pump intensity.

In summary, in PMMA films, the spectral signatures remain similar to those of the solutions, which mean that intermolecular interaction, which would lead to excitonic features, is weak. Subpicosecond charge separation and recombination on a 1 ns time scale was observed for all samples. In terms of their photophysical behavior, dyads can be easily divided in the two groups, a “prato-type” compounds **1** and **6**, and those with a flexible linker **8** and **9**. The slower recombination in PMMA for **8** and **9** was ascribed to hindered mobility of the linking groups and larger distance between the two sites. Interestingly, photoexcitation dynamics follow a similar trend in **1** and **6** despite tert-butyl peripheral substitution of ZnPc in **1**. It seems, intramolecular interactions play a bigger role in affecting the photoexcitation dynamics than intermolecular ones.

### 4.1.2.3 Photophysics in drop casted films on glass

The EADS spectra of **1** in drop casted films (Figure 51a) and in PMMA (Figure 50a) are similar which means that even in dense films, **1** cannot find an intermolecular arrangement that leads to strong excitonic interactions. In EADS of **1**, PAD1 at 1.46 eV is clearly visible, which is absent in **8** and **9**. Comparing EADS 1 and EADS 2 of **1**, we find that PAD1 and PAD2 do not show the same decay, unexpectedly. This means, the band at 1.46 eV was equivocally assigned to PAD1. Possibly, a triplet state gives the same PA band at 2.3 eV as a charged state. Additionally, the doublet at 1.15 and 1.25 eV is appears being better separated than in the other dyads. No intensity dependence is observed for **1**, meaning that the charge recombination flows fully geminate. Surprisingly, **6** behaves differently from **1** in drop casted films. Those features find more resemblance with those of **8** which will be discussed below.

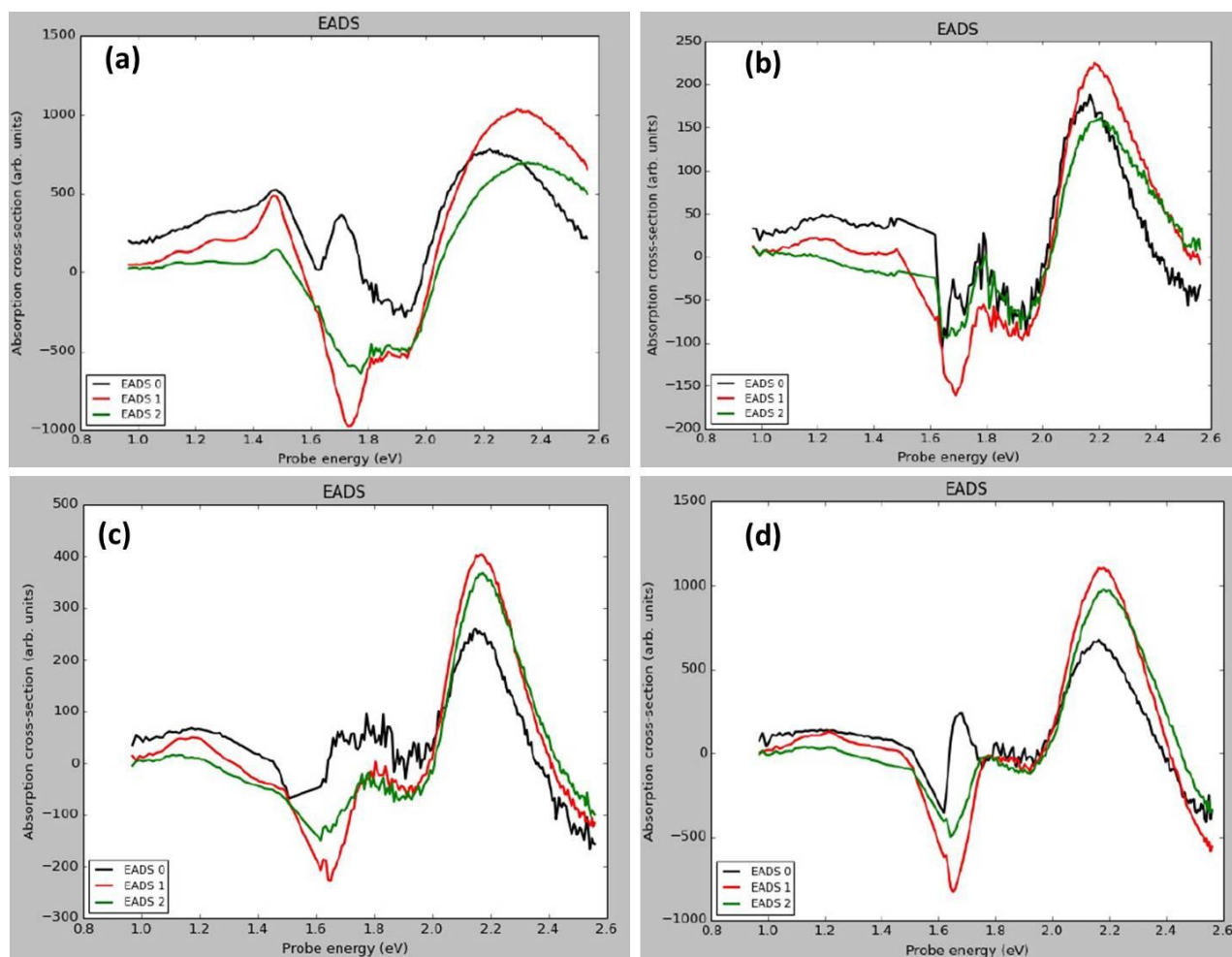


**Figure 51.** a) EADS from global fits for TA spectra of ZnPc-C<sub>60</sub> films a) **1**, b) **6**, c) **8** and d) **9** in drop casted films on glass, obtained after pumping at 387 nm with 150 fs, pulses and 560 nJ pulse energy.

Figure 51c refers to drop-cast films of **8**. It is evident that the bleach contributions are vastly different from those in PMMA films, pointing to intermolecular interactions taking place. The main bleach is shifted from 1.85 eV to 1.65 eV, explained by J aggregation.<sup>118,119</sup> There is a strong PA band at 2.2 eV, which is very similar for all EADS in Figure 51c, from which we conclude that even in EADS0, there is no singlet state. There are two possible explanations for this observation: (i) charge separation in dense films occurs on a time scale shorter than 200 fs, our instrumental resolution, or (ii) the charged state is the primary excitation, directly generated from the pump pulse. These observations are similar to the ones in P3HT-PCBM bulk heterojunctions, and so this study might add clues to the ongoing discussion. Another observation does not have an obvious explanation: at the position of the C<sub>60</sub>(-) band, we seem to have a doublet, and this doublet has a strongly different decay kinetics than the PAD2 band at 2.2 eV. PAD2 decays on a 400 ps time scale while the doublet at 1.2 eV decays on a 10 ps time scale. However, for donor-acceptor charge separation, both donor and acceptor charged bands should decay with the same kinetics. As a possible solution to explain such an event, we assume that one of the bands constituting the doublet is in fact a triplet state. The band at 1.2 eV decays faster than the one at 1.15 eV. Intensity dependent measurements do not show a strong change of the charge carrier lifetime. This means that even in drop cast films, most of the charge recombination is geminate, which is undesirable for photovoltaics. EADS of **9** in drop casted film is represented on the Figure 51d. In overall, **8** and **9** behave very similarly, with respect to the spectral shapes of the EADS as well as the resulting time constants. As in the case of **8**, in **9** the charge recombination is mostly geminate.

In summary, in dense films fabricated by drop casting of  $5 \times 10^{-6}$  M solutions of dyads in THF, we find strong excitonic effects for all systems, with the exception for **1**, from enhanced intermolecular interaction. Charge carrier formation in all cases is so fast that we cannot resolve it ( $< 200$  fs). Interestingly, it might even be the case of a direct excitation of charges. Charge recombination happens faster than in PMMA matrix. However, the geminate recombination remains strong which means that the charge pairs do not become really separated but stay spatially correlated. Finally, in drop casted films we find evidence for the occurrence of a third state, which might be a triplet state. More profound studies are deemed necessary to understand such kinetics. However, they were not undertaken within a time framework of this thesis.

**Table 4.** Transient charge separation (CS) and recombination (CR) time constants in picoseconds (ps) of the dyads in THF solutions, PMMA matrix and drop casted films (films).

Compound	CS (THF)	CR (THF)	CS (PMMA)	CR (PMMA)	CS (film)	CR (film)
<b>1</b>	1.15	234	0.40	849	< 200 fs	568
<b>6</b>	1.28	403	0.19	982	< 200 fs	666
<b>8</b>	1.92	320	0.31	757	< 200 fs	471
<b>9</b>	1.61	669	0.43	1152	< 200 fs	529

### 4.1.3 Microscopic characterization

Next, the amphiphilic dyad **7**, bearing charged ammonium functionality, was synthesized with the aim to study its ability towards self-assembling in aqueous solutions in a similar manner to how it has been reported before by our group. However, according to TEM studies, extensive sonication in water did not afford formation of any nanorod-like/fiber structure on the TEM grid, except those globular agglomerates represented in the Figure 52. Lower dispersiveness of the dyad **7** in aqueous media might be due to the lack of the tert-butyl substituents, making stronger an intermolecular interaction between the nanocarbonic units.

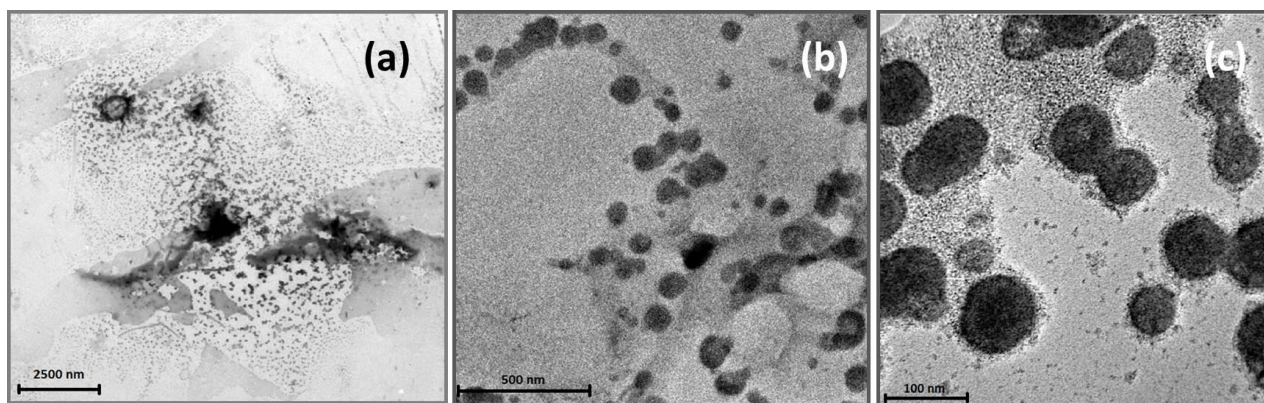


**Figure 52.** a) TEM image of the nanotubules formed by dispersion of conjugate **17** in H<sub>2</sub>O. b) AFM image of **17** drop-casted from THF/H<sub>2</sub>O dispersion on a silicon oxide surface.

The drop casted films that were studied by femtosecond TA were examined by AFM in order to draw the correlation between the surface morphology and photophysical behaviour of the systems. In the case of the dyad **1**, a uniform coverage of the glass surface by

tens of nanometer-size agglomerates has been found. The corresponding topographic image and phase picture are represented on the Figure 53a and 53b. The profile information (Figure 53c) suggests the formation of nearly 200 nm layer packed with approximately 100 nm size ZnPc-C<sub>60</sub> spherical agglomerates. In a contrast, being deposited in the same conditions, dyad **6** revealed stronger tendency to segregation (Figure 53d and 53e). The latter afforded the formation of interconnected few micrometres-long, 300 nm-height islands, comprising approximately 100 nm size spherical agglomerates of ZnPc-C<sub>60</sub> dyad **6**. The observed morphology stands in agreement with the charge dynamics revealed by femto-second TA. In other words, absence of an ordered structure, that would allow an efficient charge delocalization and extraction, brings these systems to a geminal recombination as a governing mechanism after charge separation. More tight intramolecular distances in **6**, when compared with **1**, are mostly dictated by less affinity of the molecules towards the glass surface. The latter brings **6** to a non-structured formation of amorphous aggregates that prefer to form stacks giving bigger amorphous agglomerates rather than to remain on the surface.

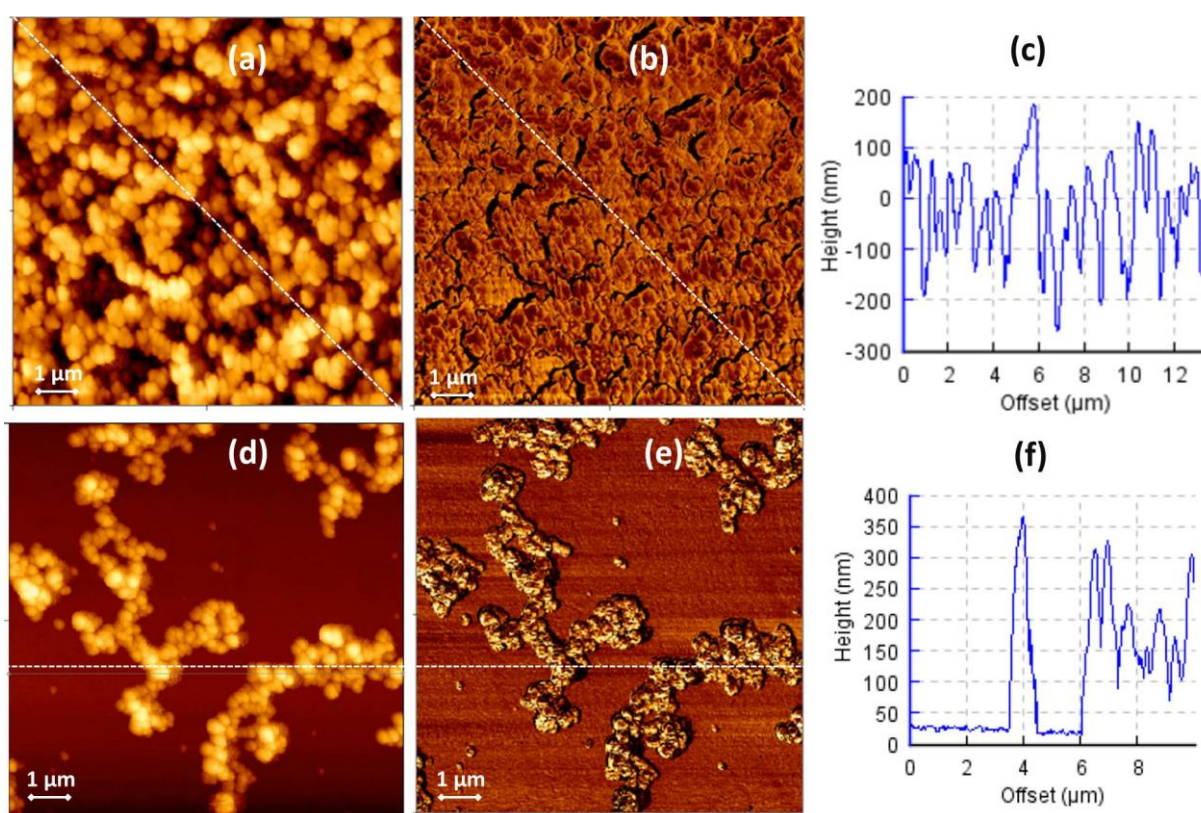


**Figure 53.** AFM topographic image of a spin casted solution of a) **1** and d) **6** in THF on glass. The corresponding profiles along the dashed white line of c) **1** and f) **6**. Phase image for b) **1** of the area shown in a), and for e) **6** of the area shown in d).

Examination of the morphology of the films of the remaining two dyads with flexible linkers **8** and **9** afforded informative images represented in the Figure 54. Interestingly, the fairly similar structures have been found in both cases – uniform spherical dots of approximately 400 nm average size. Obviously, a certain degree of geometrical freedom allowed their self-assembly, avoiding an extensive contact with hydrophilic surface of a glass substrate. At this point, it would be extremely difficult to predict the packing geometry of the dyads **8** and **9** within these spheres. One can suggest those to have a micelle structure with fullerenes pointing inward the sphere whereas phthalocyanines – outward, as a consequence of being immersed in a coordinating THF solution. However, such suggestions have only a speculative character and are not supported by any strong experimental evidences. It's worthy to mention that presence of such nano-sized particles might be the reason of an extremely pronounced scattering in UV-vis spectra of drop casted films of **8** and **9**, earlier shown on the Figure 54c and 54d. Not a surprise, a geminate recombination was observed as a major mechanism of relaxation in TA experiments.

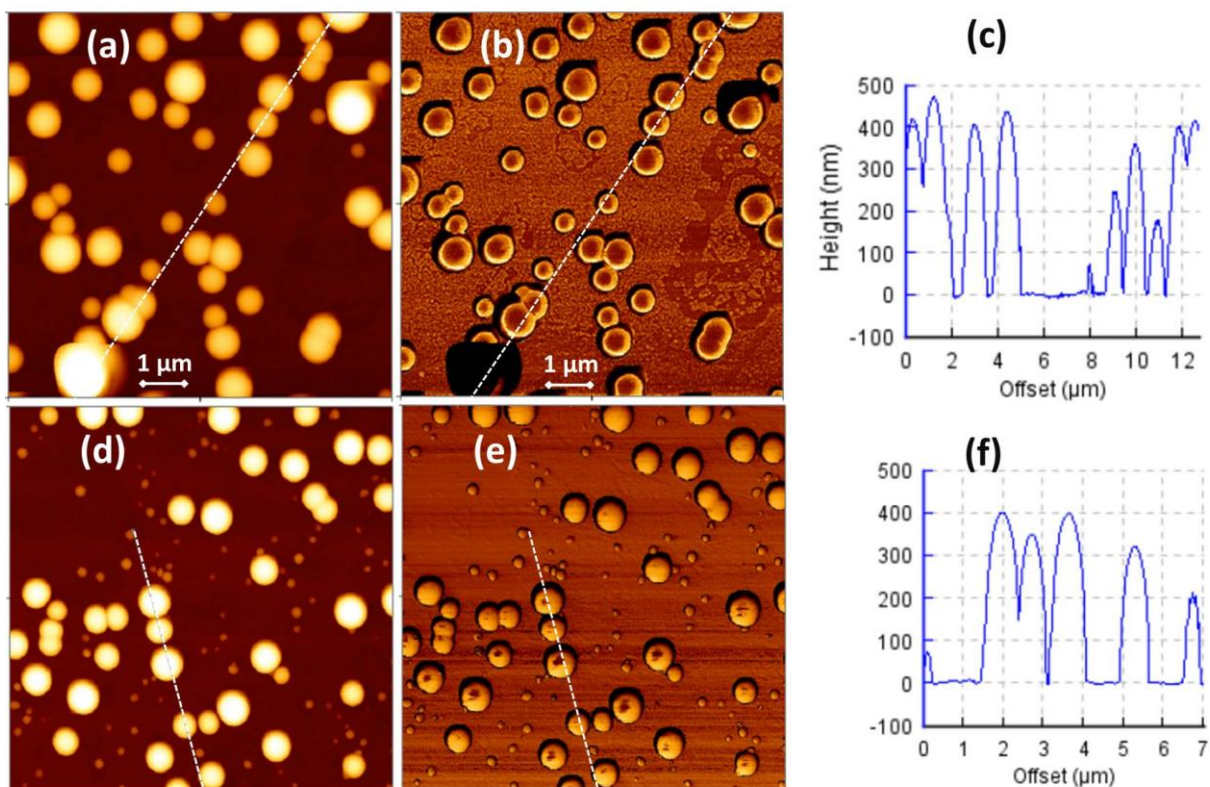


**Figure 54.** AFM topographic image of a spin casted solution of a) **8** and d) **9** in THF on glass. The corresponding profiles along the dashed white line of c) **8** and f) **9**. Phase image for b) **8** of the area shown in a), and for e) **9** of the area shown in d).

## 4.2 DNA interstrand cross-linking on surface

Several methods for cross-linking of DNA strands have been described.<sup>120</sup> Exploiting a technique for covalent cross-linking of furan-modified ODNs in solution this was the first study to demonstrate this principle on flat surfaces by integration of three components: furan-modified short oligos (12mers), oxidative coupling using a “residue-free” oxidant, singlet oxygen, and an efficient soluble phthalocyanine photosensitizer functional with red light. In the following results is demonstrated that covalent ICL formation can be applied to surface-immobilized oligonucleotides using  $^1\text{O}_2$  on furan-carrying ODNs allowing for the use of considerably shorter oligonucleotides than in classical hybridization-only based DDI. Proof-of-principle is demonstrated by surface plasmon resonance (SPR) measurements on a Biacore system using complementary oligonucleotide pairs for cross-linking and an FITC/anti-FITC probe as a model system in order to generate strong SPR signals.<sup>121</sup> In addition, the high efficiency of the principle is confirmed by an Enzyme-linked Immunosorbent Assay (ELISA).

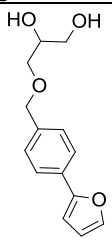
Addressable surfaces are promising tools for bioanalytical and diagnostic applications and for positioning of biomolecules on chips, in microfluidic channels or other structures. Site-specificity allows e.g. for multiplexed assays. DDI has been explored in this context as an easily accessible address generator. For follow-up assay steps or manipulations a stable bond is desirable. The second part of the results show the development towards the implementation of this ICL methodology into a multiplex immunoassay for cardiac markers, studies of the effect of the singlet oxygen on the antibody as well as cross-reactivity tests on SPR and microarrays are shown. Table 4 identifies the ODNs used in the experiments.

---

<sup>120</sup> a) K. Ichikawa, N. Kojima, Y. Hirano, T. Takebayashi, K. Kowata and Y. Komatsu, *Chem. Commun.*, **2012**, 48, 2143-2145; b) M. Shelbourne, T. Brown, A. H. El-Sagheer and T. Brown, *Chem. Commun.*, **2012**, 48, 11184-11186; c) N. E. Price, K. M. Johnson, J. Wang, M. I. Fekry, Y. Wang and K. S. Gates, *J. Am. Chem. Soc.*, **2014**; d) S. Ghosh and M. M. Greenberg, *J. Org. Chem.*, **2014**, 79, 5948-5957.

<sup>121</sup> a) J. A. Schenk, F. Sellrie, V. Böttger, A. Menning, W. F. Stöcklein and B. Micheel, *Biochimie*, **2007**, 89, 1304-1311; b) M. Hovestädt, H. Memczak, D. Pleiner, X. Zhang, J. Rappich, F. F. Bier and W. F. Stöcklein, *J. Mol. Recognit.*, **2014**, 27, 707-713.

**Table 4.** Oligonucleotide sequences and nomenclature.

DNA name	DNA Sequence	Structure of furan-containing nucleoside X
ODN1	5' biotin CTG ACG GXG TGC 3'	
ODN2	5' biotin CAG TCG GXG AGC 3'	
ODN3	5' biotin GAC TGC CXC ACG 3'	
ODN4	5' biotin CAC AGC CXC TCG 3'	
ODN10	5' biotin G ACG GXG TGC 3'	
ODN8	5' biotin ACG GXG TG 3'	
C.ODN1	3' GAC TGC CCC ACG-FITC 5'	
C.ODN2	3' GTC AGC CCC TCG-FITC 5'	
C.ODN3	3' CTG ACG GXG TGC-FITC 5'	
C.ODN4	3' GTG TCG GXG AGC-FITC 5'	
C.ODN10	3' C TGC CCC ACG-FITC 5'	
C.ODN8	3' GC CCC ACG-FITC 5'	

### 4.2.1 DNA-directed immobilization on SPR biosensor chips

The limit of detection of hybridization of the C.ODN1 at different concentrations with the immobilized ODN1 on the neutravidin-coated gold chip are shown in Figure 55. Concentration-dependent binding signals were obtained as a function of the injection time.

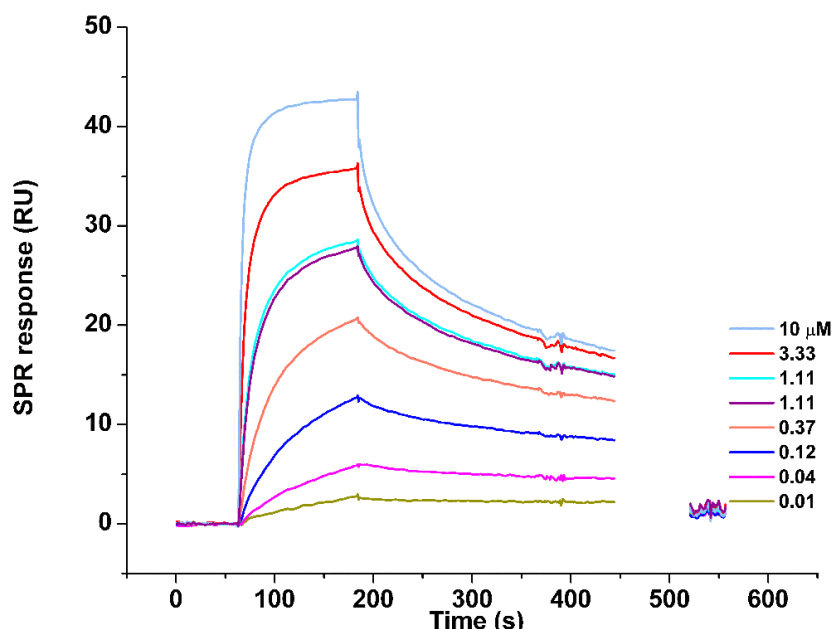


**Figure 55.** Exemplary sensorgrams of injections of different concentrations (10  $\mu\text{M}$ -0.01  $\mu\text{M}$  in a 1:3 dilution series) on C.ODN1 functionalized flow cell.

The formation of a covalent bond between the immobilized ODN on a surface and the C.ODN target should enhance the stability of the duplex. This duplex should be stable even in the presence of  $\text{Na}_2\text{CO}_3$  which has a strong anion effect and stabilizes



the single stranded conformation.<sup>122</sup> Using ODN1, DNA cross-linking on the surface was investigated using 5  $\mu\text{M}$  MB at the conditions described above. Detection of hybridized ODN1 by binding of the HRP-labelled anti-FITC antibody showed similar SPR response to the cross-linked ODNs after regeneration of the surface with  $\text{Na}_2\text{CO}_3$  (Figure 56). This is due to the increased stability of the ODN duplex by the cross-link formed. The somewhat lower signal (B1 vs. A1) may be due to some singlet oxygen-induced DNA damage. When ODN1 was only hybridized, thus allowing dehybridization, the duplex was not stable to the regeneration step.

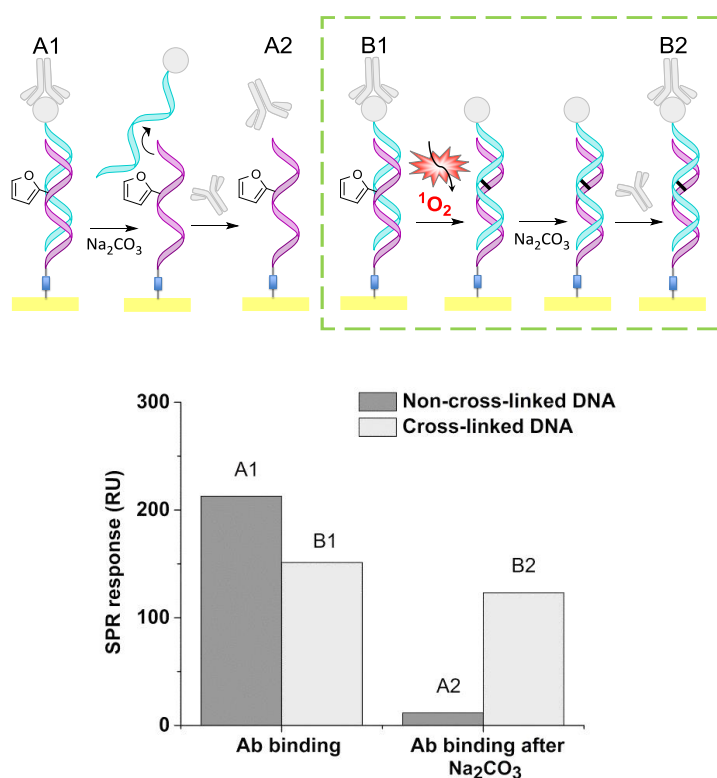


**Figure 56.** Comparison of the SPR signal obtained from non-cross-linked DNA and cross-linked DNA duplex (ODN1-C.ODN1). The signal obtained from the hybridized duplex (A1) decreases after surface regeneration (A2). The binding of the cross-linked DNA duplex with the recognition antibody is stable after regeneration following ICL formation (B1-B2). Detection of DNA ICL formation using ODN1 by 48 nM of HRP-labelled anti-FITC antibody, its binding is stable after regeneration using 50 mM  $\text{Na}_2\text{CO}_3$ .

<sup>122</sup> E. N. Galyuk, D. Y. Lando, V. P. Egorova, H. Dai and Y. M. Dosin, *J. Biomol. Struct. Dyn.*, **2003**, 20, 801-809.

## Results and Discussion

Covalent cross-linking in solution was proven using polyacrylamide gel electrophoresis and MALDI-TOF-MS, resulting in the observation of  $[M+H]^+/2$  at  $m/z$  4,132.332 for ODN1-C.ODN1.

Control experiments confirmed that the anti-FITC HRP antibody does not bind to the immobilized biotinylated and furan-modified capture oligonucleotide ODN1, the antibody only recognizes the FITC from the respectively labeled sequence C.ODN1 once hybridization has occurred. The sensorgram observed during the Biacore experiments is shown in Figure 57.

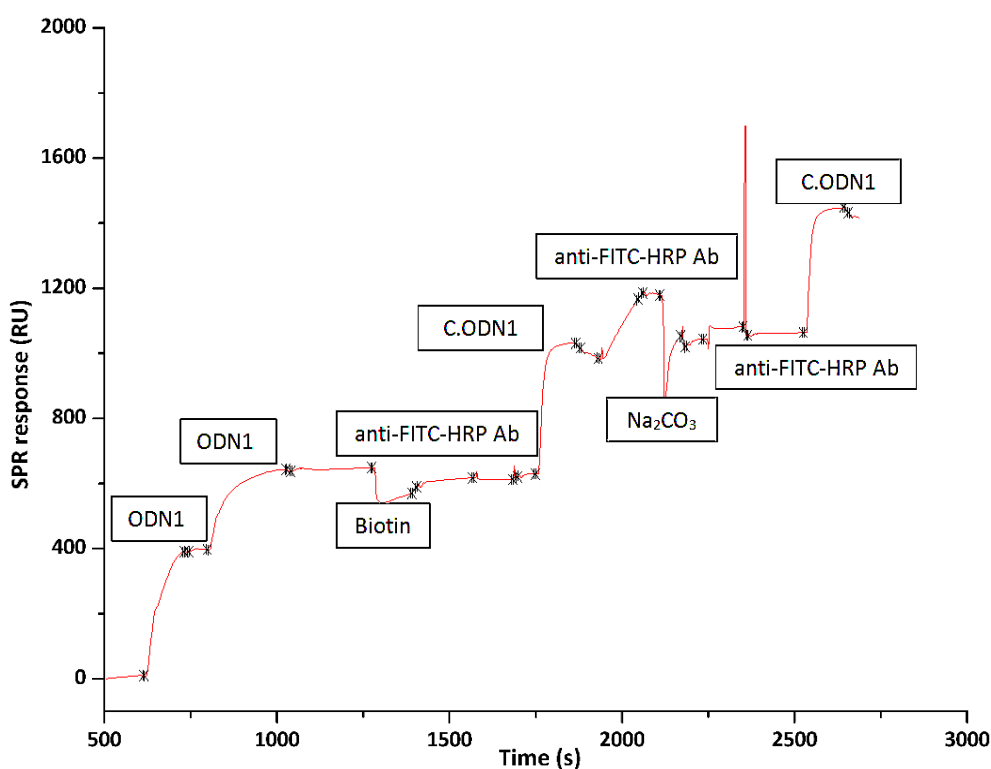


**Figure 57.** Control experiment. The anti-FITC HRP antibody does not bind to the immobilized biotinylated and furan-modified capture oligonucleotide ODN1, the antibody only recognizes the FITC from the respectively labelled sequence C.ODN1 once hybridization has occurred.

The ICL of the novel furan-modified sequences, ODN2, 3 and 4 to the complementary C.ODNs showed similar SPR response, the increase in the SPR response corresponding to the binding of FITC-C.ODN sequences with the recognition antibody is preserved after regeneration conditions due to the covalent bond formed, which increased the stability of the ODN duplexes.

Figure 58 shows the overlay of the sensorgrams obtained and a schematic representation of the steps during the experiment.

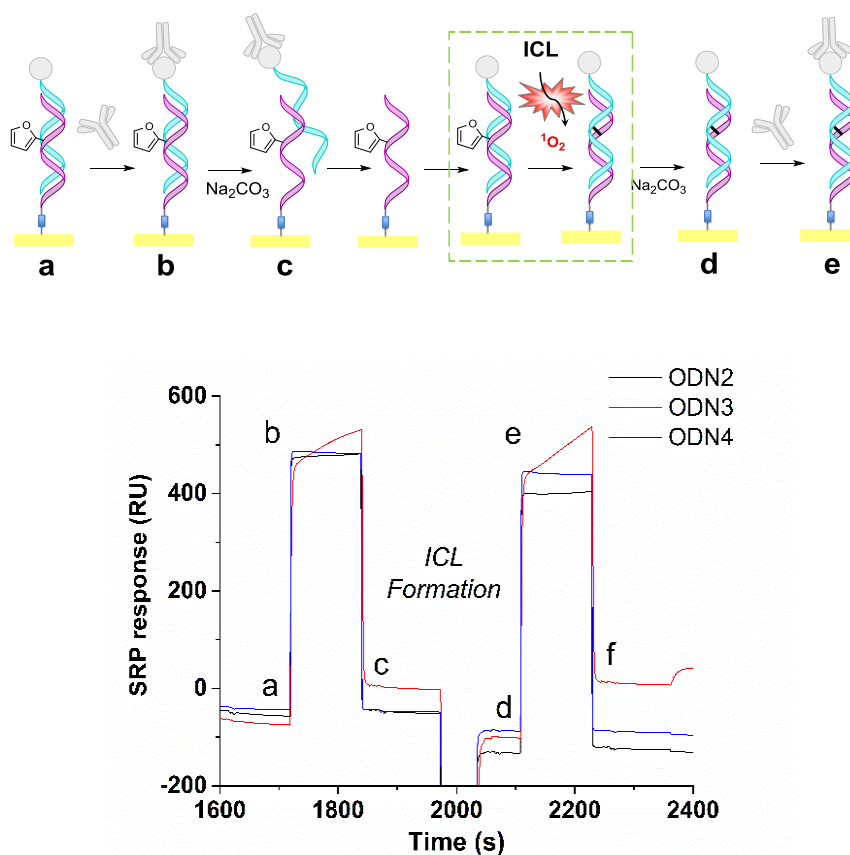


**Figure 58.** SPR sensorgram from non-cross-linked DNA and cross-linked DNA (ODN2, 3 and 4). The injection of the anti-FITC-HRP detection antibody (48 nM) on the immobilized hybridized ODN duplexes (a) produced an increase of the signal (b). This signal decreased after surface regeneration using 50 mM  $\text{Na}_2\text{CO}_3$  (c). Then, the chip was taken out of the SPR instrument for hybridization and irradiation for ICL formation (5  $\mu\text{M}$  MB). The chip was introduced into the SPR instrument again and the surface was regenerated again (d). Even after surface regeneration the detection antibody still recognised the FITC label C.ODN of the stable duplex leading to an increase in the SPR response (e). The binding of the ODNs and the detection antibody was disturbed again using  $\text{Na}_2\text{CO}_3$  (f).

SPR experiments indicates that the yield of DNA Cross-linking formation by using MB was 30-40 % and for TT1 ca. 5-10 %. As expected, the MB was more efficient in promoting ICL formation than the phthalocyanine TT1, whose lower photodynamic activity can result from the formation, to some extent, of molecular aggregates in water.<sup>7</sup>

## Results and Discussion

In order to determine suitable sequences which can be used in platforms for multiplexed diagnostic assays, hybridization specificity measurements were performed. The binding of the novel furan-modified sequences, ODN2, 3 and 4 to the complementary C.ODNs are presented in Table 5. All three sequences are very specific and show no cross-reactivity. Moreover, the specific detection of ODNs in solution was possible even for mixtures, laying the basis for a selective platform for multiplex bioanalytical applications.

**Table 5.** Binding signals in RU obtained by injection of 1  $\mu\text{M}$  C.ODNs 2, 3, & 4. The three sequences yield highly specific binding, unspecific effects are < 2 %.

	C.ODNs						
	2	3	4	2+3	2+4	3+4	2+3+4
ODN2	351	1	-10	331	319	-3	327
ODN3	5	324	-7	318	1	292	308
ODN4	1	2	287	2	282	284	288

The studies focussing on finding out the minimum oligonucleotide length that can achieve an efficient crosslink on a surface are presented in Figure 59. The results show that a 12 or 10mer ODNs can be used because the affinity decreases drastically in the case of an 8mer, as was expected because its length is under the 10 bases that a turn of the DNA helix requires.

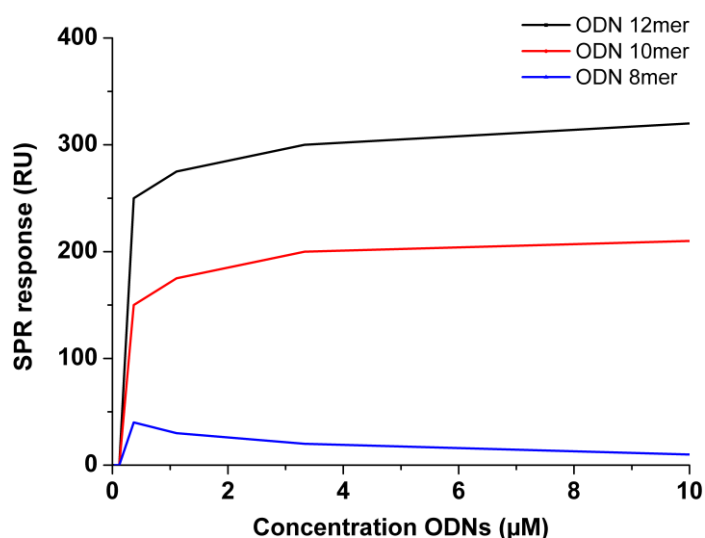
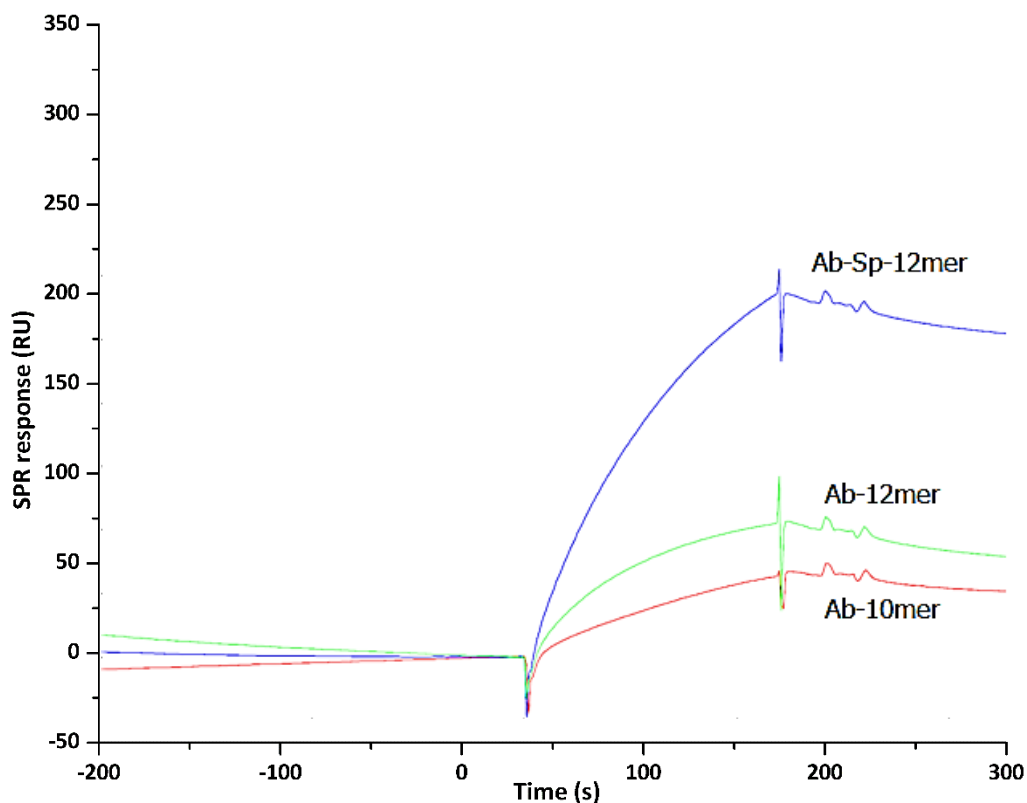


**Figure 59.** SPR response of the oligonucleotide affinity on the surface. The 10- and 12mer ODNs are suitable for addressing an ODN-antibody conjugate.

The 10- and 12mers were selected for the synthesis of the antibody-oligonucleotide conjugate required. The conjugates were synthesized by a method already described,<sup>123</sup> and the best result was obtained for the conjugate that has a spacer (Sp (poly (T) tail of 10 bases)) between the antibody and the recognition sequence (Figure 60).



**Ab-Sp-12mer >> Ab-12mer > Ab-10mer**

**Figure 60.** Antibody-oligonucleotide conjugate affinity over the time.

<sup>123</sup> O. Söderberg, K.-J. Leuchowius, M. Gullberg, M. Jarvius, I. Weibrecht, L.-G. Larsson and U. Landegren, *Methods*, **2008**, 45, 227-232.

## 4.2.2 Light-induced immobilization on microplate surfaces

The results in Figure 61 clearly show that both MB and irradiation are necessary for the ICL formation, being both limiting factors for the formation of singlet oxygen necessary to oxidize the furan nucleoside which can then form the covalent link with the complementary strand. The wells under dark control conditions produce insignificant optical density (OD) values after regeneration of the surface with sodium carbonate. The OD after dehybridization attack almost reaches the values observed before surface regeneration.

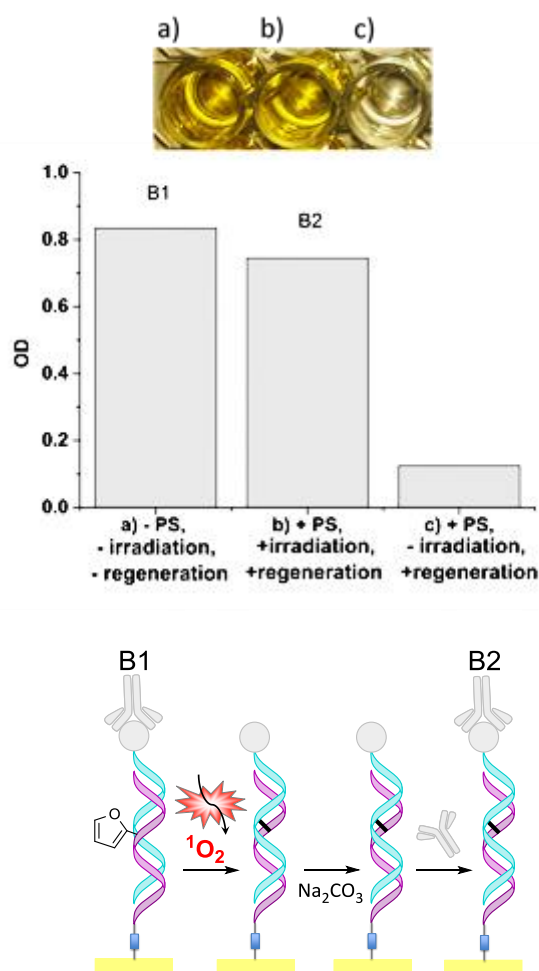


**Figure 61.** Signals (OD) obtained for a microtiter plate-based ELISA based on duplex systems (ODN1-C.ODN1) B1 and B2 and a HRP-labelled detection antibody. Comparison of the values obtained before and after regeneration with 50 mM  $Na_2CO_3$  and irradiated vs. protected parts with photosensitized (5  $\mu$ M MB) cross-linking. High signals indicate cross-linking requires a photosensitizer (PS) and light.

### 4.2.3 Multiplex immunoassay cross-reactivity

The results in Figure 62 shows the cross-reactivity experiments performed in microarray and surface plasmon resonance. The concentration choosed of the analyzed proteins were in function of their differents levels of clinical cut-off, which are summarized in the chapter 1.1.1 Cardiac Biomarkers. SPR experiments were performed first to determine that all reactans of the immnuassay reaction are suitable for the use in the future address-multiplex diagnostic assay. The biding signals are represented in Figure 62.a). All components showed a high specificity and no cross-reactivity with the others reactans and only showed biding with their corresponding match. However, when the multiplex immunoassay is performed in microarray its presents a high cross-reactivity of the T1 protein with all captures antibodies (Figure 62.b). Therefore, TI shouldn't be combine with FABP and CRP proteins on microarray detection platform. Although have been used before in multianalyte detection using differents transduction platforms.<sup>124</sup> The higher florescence intensity in microarray of CRP corresponds with the high resonance units of SRP. As well as for FABP, it shows few resonance units in comparison with values obtained for T1 and CRP.

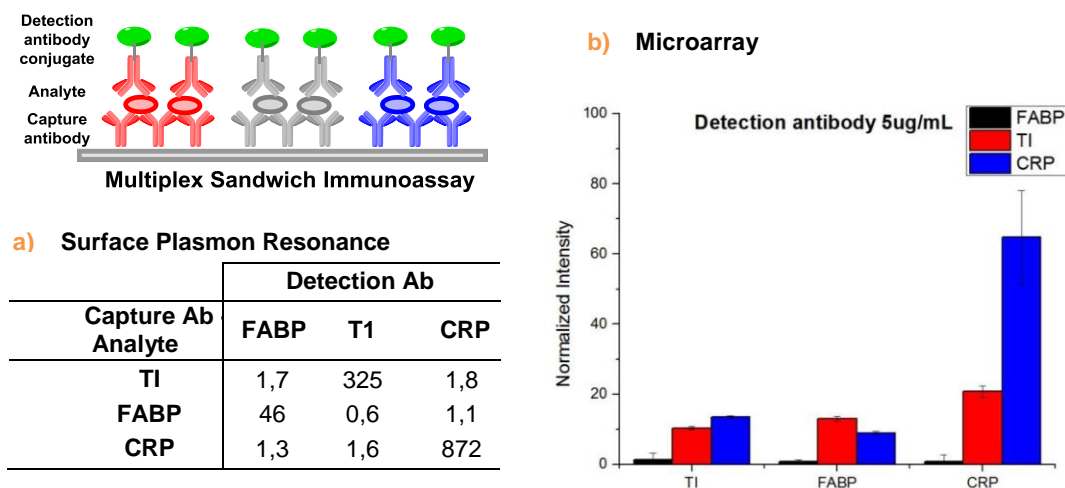


**Figure 62.** Cross-reactivity of the multiplex sandwich immunoassay. a) Binding signals in RU obtained by injection of 1  $\mu\text{g/mL}$  detection antibody-FABP; TI & CRP. Three antibodies yield highly specific binding, unspecific effects are < 1 %. b) Normalized intensity fluorescence signals obtained from a microarray.

<sup>124</sup> a) A. Qureshi, Y. Gurbuz and J. H. Niazi, *Sens. Actuators B*, **2012**, 171–172, 62-76; b) D. P. Matta, S. Tripathy, S. R. Krishna Vanjari, C. S. Sharma and S. G. Singh, *Biomed. Microdevices*, **2016**, 18, 111; c) N. Radha Shanmugam, S. Muthukumar, S. Chaudhry, J. Anguiano and S. Prasad, *Biosens. Bioelectron.*, **2017**, 89, 764-772.

## 4.2.4 Implementation of ICL in immunoassays

The OD values of the immunoassay decrease significant over time after irradiation of the capture antibody in the presence of photosensitizers (Figure 63). The singlet oxygen oxidate the disulfide bonds, which are critical to maintain the protein structure and are particularly susceptible to oxidative modification and loss of function very fast.<sup>125</sup>

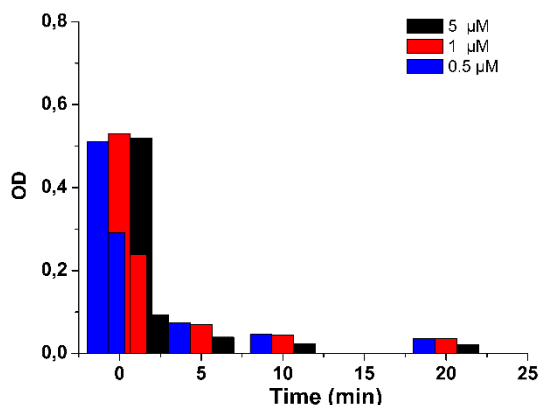


**Figure 63.** OD values obtained by variation of the irradiation time with red light and methylene blue (5, 1 and 0.1  $\mu\text{M}$ ). The OD values are reduced after irradiation of the capture antibody.

The results of study the ICL on surface at lower concentration of photosensitiser and irradiation time confirmed that the ICL formation is faster than in solution. On the surface the irradiation time required for ICL formation is only 10 min. In Figure 64 it is shown that a concentration of 5  $\mu\text{M}$  MB is more efficient.

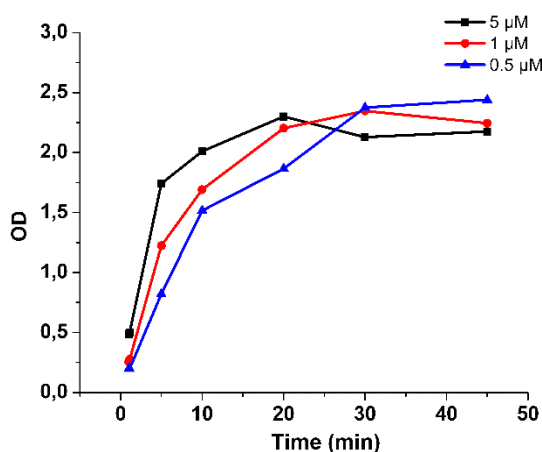


**Figure 64.** OD values obtained by variation of the concentration of methylene blue (5, 1 and 0.5  $\mu\text{M}$ ) and the irradiation time in minutes.

<sup>125</sup> M. Karimi, M. T. Ignasiak, B. Chan, A. K. Croft, L. Radom, C. H. Schiesser, D. I. Pattison and M. J. Davies, *Sci. Rep.*, **2016**, 6, 38572.



## **5. Conclusions**

---



## 5.1 Phthalocyanine-C<sub>60</sub> fullerene dyads

In conclusion, four novel ZnPc-C<sub>60</sub> dyads **6-9** have been designed and synthesized, bearing peripherally unsubstituted ZnPc units. To achieve this goal, two main synthetic strategies for the covalent modification of C<sub>60</sub> fullerene have been successfully employed; namely Prato-type 1,3-dipolar cycloaddition and Bingel-Hirsch method of cyclopropanation. Preparation of novel TBDPS-substituted ZnPc was deemed important for obtaining all these conjugates. The synthesis of monosubstituted Pcs in sufficient amount and purity for their further covalent modification has been a bottleneck in chemistry and materials science employing non-substituted Pcs. It was obtained in enough quantities for the studies even the difficulties of the synthesis and purification.

Next, the study of photoexcitation dynamics of donor-acceptor conjugates **6, 8** and **9** in comparison with tert-butyl substituted analog **1**, performed in THF solution, PMMA matrix and drop casted film, allowed us to estimate the influence of the condensed phase of the lifetime of charge separation (CS) and charge recombination (CR). This is a valuable information for OPV community. Briefly, a longer spacer between ZnPc and C<sub>60</sub> and the use of PMMA matrix was found to extend times of CS and CR, especially for the dyads **8** and **9** – by “freezing” them in one of the conformations. In contrast, the CS and CR times were significantly dropped down for the dyads in the drop casted films as a consequence of closer intermolecular contacts and the lack of any supramolecular order in the solid state. In fact, all the systems suffered a geminal recombination, extremely undesirable in OPV applications, since it means excitons are not successfully split into free charges.

In addition, all the films studied by TA were investigated by AFM, revealing a globular morphology of the amorphous agglomerates having a size of hundreds of nanometers. Additionally, the amphiphilic dyad **7** was studied by TEM, however, no sign of a presence of ordered structures similar to fibers or rods was found. Despite an apparent strong tendency of the dyads to intermolecular interaction and a dense packing in the solid state, no evidence could be found in solution in the range of concentrations from 10<sup>-7</sup> to 10<sup>-5</sup> M, employing UV-vis spectroscopy. The results of our study suggest the necessary use of nanocomposite polymers as possible templates for enhancing the supramolecular ordering and consequent OPV performance of the ZnPc-C<sub>60</sub> covalent dyads.

## 5.2 DNA Interstrand cross-linking on surface

The steps to develop a new stable platform based on ICL methodology were described and all objectives were successfully accomplished. It was shown that ICL formation of furan-modified DNA is a very useful method to increase the stability of short immobilized DNA duplexes on a surface. SPR and ELISA experiments confirmed the ICL formation and the stability of the DNA after regeneration compared to the non-cross-linked ODN.

Two photosensitizers were compared and it was determined that methylene blue (MB) is more efficient in promoting ICL formation than the phthalocyanine TT1. Its lower photodynamic activity can result from the formation, to some extent, of molecular aggregates in water. The minimum optimum length for addressing the antibody-oligonucleotide conjugate was found to be 12mer with a poly(T)<sub>10</sub> tail. Furthermore, this work demonstrates that it is possible to simultaneously use three different specific sequences for selective immobilization on a microarray surface.

Concluding it can be said that this technique represents a biomolecule-compatible immobilization method that could improve the robustness of array-based detection methods, but the effect of the singlet oxygen on the change of the binding site of the antibody needs to be taken into account. Nevertheless, it is a very promising tool to increase the stability of other surfaces based on DNA hybridization which usually have the drawback of being rather unstable.

Phthaloyanines proved to be versatile compounds in achieving nanochemical structures that can be used in novel, innovative devices.